

A NOVEL ANTIBODY FOR THE DETECTION AND TREATMENT OF
PANCREATIC DUCTAL ADENOCARCINOMA

by

Shu-ta Wu

A dissertation submitted to the faculty of
The University of North Carolina at Charlotte
in partial fulfillment of the requirements
for the degree of Doctor of Philosophy in
Biology

Charlotte

2017

Approved by:

Dr. Pinku Mukherjee

Dr. Didier Dréau

Dr. Craig Ogle

Dr. Christine Richardson

Dr. Shan Yan

ABSTRACT

SHU-TA WU. A novel antibody for the detection and treatment of pancreatic ductal adenocarcinoma. (Under the direction of DR. PINKU MUKHERJEE)

Pancreatic ductal adenocarcinoma (PDA) remains the most aggressive cancer with a 5-year survival rate below 10%. Two of the major contributors to this dismal prognosis are late-stage diagnosis and limited treatment options. Common symptoms of PDA like weight loss, abdominal pains, and jaundice do not appear until the cancer has progressed to late stage and the tumor is of significant size. Surgery and systemic delivery of chemotherapies is the standard treatment for patients, but the associated side effects are severe and the overall survival rate remains unchanged. Therefore early detection (Chapter 2) and targeted drug delivery (Chapter 3) in PDA is highly desirable. Mucin 1 (MUC1) is a tumor-associated antigen (tMUC1) expressed on 80% of human PDA. Here I report the targeting capabilities of TAB004, a tMUC1 specific antibody, for diagnosing and treatment purposes using a fluorophore bound antibody and a TAB004-conjugated PEGylated PLGA (poly lactic-co-glycolic acid) nanoparticle that is loaded with a paclitaxel (PTX). In orthotopic immunocompetent mice, I show that TAB004 specifically targets the tumor without significant accumulation in other organs. Conjugating TAB004 to the surface of PLGA Nanoparticles (T-NPs) significantly increased their internalization into PDA cells as well as their cytotoxicity of PDA cells when compared to the non-conjugated PLGA-NPs. *In vivo*, the T-NPs showed dramatically increased accumulation within the pancreatic tumor when compared to the non-conjugated PLGA NPs. The data suggests that TAB004 is a promising

antibody to deliver imaging agents and treatments directly to the pancreatic tumor microenvironment, thus improving detection and treatment of PDA

DEDICATION

To my wife, Somaly

and

my children, Adria, Alyssa, and TBD Progeny #3.

Kids, if I can do this, you can do better.

ACKNOWLEDGEMENTS

This work was made possible through the wonderful guidance of Dr. Pinku Mukherjee. Thank you for the opportunity to work in your lab, your mentorship, and especially for funding most of my research. I would like to thank my committee: Dr. Didier Dréau, Dr. Craig Ogle, Dr. Christine Richardson, and Dr. Shan Yan for their support. Thank you to the members, past and present, of the Mukherjee lab, Priyanka Grover, Laura Moore, Mahbeoubeh Yazdanifar, Shayan Nazari, Dr. Timothy Erick, Dr. Maria Bogachek, Dr. Jenny Curry, Dr. Dahlia Besmer, Dr. Sritama Nath, Dr. Lopa Das Roy, and a special thank you to Dr. Ru Zhou whose guidance on many subjects and projects was extremely helpful. Thank you to the animal team at the University of North Carolina at Charlotte's Vivarium, Hernando Gordils and Alvaro Perez, and to Dr. Chandra Williams whose expertise with the animals allowed much of this research to be done. I would like to thank the University of North Carolina at Charlotte Graduate School for providing Graduate Assistant Support award for supporting my graduate education. Thank you to the Williams States Lee College of Engineering at UNC Charlotte, Center for Biomedical Engineering and Science IVIS Imaging System Award that provided additional funding for using the IVIS Spectrum. And lastly, I'd like to thank my wife, Somaly Kim Wu, for her support in completing my PhD journey.

Oh, and thanks kids. I wouldn't change a thing about this journey, but man did you girls make it difficult.

TABLE OF CONTENTS

LIST OF FIGURES	viii
LIST OF TABLES	x
LIST OF ABBREVIATIONS	xi
CHAPTER 1: INTRODUCTION	1
CHAPTER 2: IMAGING AND EARLY DETECTION OF PANCREATIC CANCER BY ANTI-MUC1 ANTIBODY, TAB004	14
2.1 Introduction	14
2.2 Material and Methods	15
2.3 Results	17
2.4 Conclusions	24
2.5 Figures	25
CHAPTER 3: TARGETING PANCREATIC CANCER WITH ANTIBODY GUIDED PLGA NANOPARTICLES	38
3.1 Introduction	38
3.2 Material and Methods	40
3.3 Results	48
3.4 Conclusions	54
3.5 Figures	55
CHAPTER 4: DISSERTATION SUMMARY	65
SUPPLEMENTAL	75
Characterizing TAB004	75
Macropinocytosis	80
REFERENCES	82
APPENDIX – Contribution, Honors, and Awards	92

LIST OF FIGURES

FIGURE 1. Overall schematic TAB004 conjugation to chemotherapeutic or imaging agent	5
FIGURE 2. . Schematic representation of the structure of MUC1.	8
FIGURE 3. MUC1 overexpression and loss of polarity in cancer cells.	9
FIGURE 4. A “PanINgram” illustrating progression of normal cellular arrangement through PanIN lesion stages	11
FIGURE 5. Diagram showing generation of KCM mice used in this dissertation	12
FIGURE 6. Fluorescent IVIS images of organs from mouse in Control Group 1	25
FIGURE 7. Fluorescent and bioluminescent IVIS images of organs from mouse in Control Group 2	26
FIGURE 8. Fluorescent IVIS images of organs from mouse in Control Group 3	27
FIGURE 9. Fluorescent IVIS images of organs from mouse in Control Group 4	28
FIGURE 10. Fluorescent IVIS images taken at different time points of mouse from murine monoclonal TAB004 injected group	29
FIGURE 11. Fluorescent IVIS images of organs from mouse in murine monoclonal TAB004 group	30
FIGURE 12. Fluorescent IVIS images taken at different time points of mouse from chimeric TAB004 injected group	31
FIGURE 13. Fluorescent IVIS images of organs from mouse in chimeric TAB004 group	32
FIGURE 14. Quantification of ROI values from all groups	33
FIGURE 15. Confocal imaging of tumor sections from Chimeric TAB004 injected mice	34
FIGURE 16. IVIS images of KC and KCM Spontaneous mice (3 and 11 weeks PI of tamoxifen) injected with TAB004	35

FIGURE 17. Immunohistochemistry images of pancreas from KCM mice	36
FIGURE 18. Fluorescent IVIS images of organs from KCM mice	37
FIGURE 19. Nanoparticle preparation and surface functionalization	57
FIGURE 20. Characterization of PLGA NPs	58
FIGURE 21. Internalization of PLGA NPs	59
FIGURE 22. Cell viability of PDA cell lines treated with PTX and PTX loaded NPs	60
FIGURE 23. Specificity and internalization of TAB004 in BxPC3 MUC1 and Neo	61
FIGURE 24. Confirmation of TAB004 conjugation to PLGA NPs with FACS	62
FIGURE 25. Internalization of TAB004 conjugated NPs loaded with fluorescein diacetate	63
FIGURE 26. Cell viability of PDA cell lines treated with PTX loaded NPs and PTX loaded TAB004 conjugated NPs	64
FIGURE 27. <i>In vivo</i> imaging of TAB004-ICG in orthotopically injected bioluminescent tumor bearing mice	65
FIGURE 28. <i>In vivo</i> imaging of ICG loaded NPs and ICG loaded T-NPs orthotopically injected bioluminescent tumor bearing mice	66
FIGURE 29. ELISA data of murine TAB004 incubated with tMUC1	77
FIGURE 30. FACS analysis of cTAB004 and hTAB004 binding profiles	79
FIGURE 31. IVIS images of SDS-PAGE gels	81
FIGURE 32. Figure 32. Confocal images of Mouse PDA cell lines treated with TMR-Dextran	82

LIST OF TABLES

TABLE 1. Results from combinational therapies with gemcitabine.	3
TABLE 2. Cargo Loading of PTX, FDA, NR, and ICG into Nanomaterials	44
TABLE 3. Structural Properties of PTX, FDA, NR, and ICG Nanomaterials	44

LIST OF ABBREVIATIONS

5FU	fluorouracil
ADAM 17	a disintegrin and metalloprotease 17
ADCC	antibody dependent cell-mediated cytotoxicity
ADCs	antibody direct (drug) conjugates
CA19.9	cancer antigen 19.9
CEA	carcinoembryonic antigen
cTAB004	chimeric TAB004
DMSO	dimethyl sulfoxide
EGFR	epidermal growth factor receptor
ELISA	enzyme-linked immunosorbent assay
EPR	enhanced permeability and retention effect
EUS-FNA	endoscopic ultrasound and fine needle aspiration
FAMMM	familial atypical mole and multiple melanoma
FDA	fluorescein diacetate
FmAbs	fluorescently labeled mAbs
FOLFIRINOX	5-fluorouracil, oxaliplatin, irinotecan, and leucovorin
GPI	glycosylphosphatidylinositol
H&E	hematoxylin and eosin
hIgG	human immunoglobulin G
hTAB004	humanized TAB004
ICG	indocyanine green
IgG	immunoglobulin G

IHC	immunohistochemistry
IVIS	in vivo imaging system
mAbs	monoclonal antibodies
MAT	monoclonal antibody based therapies
MDCT	multidetector computer tomography
MOS	median overall survival
MRI	magnetic resonance imaging
mTAB004	murine TAB004
MTT	3-(4, 5-dimethylthiazol-2-yl)-2, 5 diphenyltetrazoliumbromide
MUC1	Mucin-1
MUC1.Tg	MUC1 transgenic
MUC1-C	C-terminal subunit
MUC1-N	N-terminal subunit
NK	natural killer
NLC	nanostructured lipid carriers
NPs	nanoparticles
OD	optical density
PanIN	pancreatic intra-epithelial neoplasia
PDA	pancreatic ductal adenocarcinoma
PD-L1	programmed cell death-ligand
PDTR	Pro-Asp-Thr-Arg
PLGA	poly(lactic- <i>co</i> -glycolic acid)
PTX	paclitaxel

RE	radiance efficiency
ROIs	region of interests
SDS-PAGE	sodium dodecyl sulfate polyacrylamide gel electrophoresis
SLNs	solid Lipid NPs
SPR	surface plasmon resonance
tMUC1	tumor-associated MUC1
T-NPs	TAB004 conjugated to PLGA NPs
VNTR	variable number tandem repeat
WT	wild type

CHAPTER 1: INTRODUCTION

Pancreatic cancer is a highly aggressive cancer with a 5-year relative survival rate of 8% for all stages combined and is currently the fourth-leading cause of cancer related deaths in the United States [1]. The 5-year survival rate decreases to 3% in patients with advanced pancreatic cancer [2]. Incidence and mortality trends predict pancreatic cancer will become the second-leading cause of cancer related deaths by 2020 [3]. 95% of pancreatic cancers are pancreatic neoplasms called pancreatic ductal adenocarcinoma (PDA) [4]. Greater than 50% of patients with PDA have locally advanced or metastatic disease when diagnosed, with the liver, lungs, and peritoneum being the primary metastatic sites. This limits the viable therapeutic options to systemic chemotherapy and supportive care to alleviating symptoms [1]. Poor prognosis for patients is mainly due to a) late diagnosis due to lack of effective screening processes and distinct early symptoms and effective diagnostics [5, 6]; b) resistance to chemotherapy [7]; and c) inefficient delivery of chemotherapeutic drugs to the tumor site, likely due to the dense stroma and deficient vascular network in the pancreatic tissue microenvironment [8, 9]. The most common precursor lesion for PDA are pancreatic intra-epithelial neoplasia (PanIN) [10] and detection of these may be important for early diagnosis, but this task has proven extremely challenging to date. Surgical resection of the tumor combined with repeated treatments with various chemotherapy remains the current choice of treatment to increase survival rate. Therefore, there is a pressing need to develop an effective detection platform, since survival from PDA is increased with resection and treatment with early detection [11, 12],

along with a novel drug delivery system that can increase the drug accumulation and uptake in a tumor specific manner [13].

There are many imaging resources in use for diagnosing pancreatic cancer. Here I highlight three most commonly used modalities for pancreatic cancer imaging.

Multidetector computer tomography (MDCT) is the most widely available and validated imaging technique used for staging and diagnosis [14, 15]. The reported sensitivity of MDCT for tumor detection is excellent, ranging from 89-97% [14], but smaller tumor masses (<2cm) lower the sensitivity of MDCT to ~77%. MDCT's positive predictive value for predicting unresectability ranges from 89-100%, but it's ability to predict respectability is only 45-79% [16]. This technique is also limited in its ability to detect and diagnose small hepatic metastases [17].

Magnetic resonance imaging (MRI) is another widely used technique for detecting pancreatic tumors and in preoperative staging since it demonstrates similar sensitivities to MDCT [18]. One advantage to MRI is that it may be more accurate in characterizing small hepatic cysts and metastases than MDCT [19]. The choice between MDCT or MRI is often institution dependent, with MRI usually favored since it can be used in patients with iodinated contrast allergy and impaired renal function [14].

Endoscopic ultrasound and fine needle aspiration (EUS-FNA) are techniques used for preoperative tissue diagnosis and evaluation of patients suspected of having pancreatic cancer [20]. EUS-FNA is an invasive procedure that required a highly skilled operator, but its sensitivity in diagnosis pancreatic cancer ranges from 80-95% [18]. Risk of biopsy-

related complications include pancreatitis, bleeding, perforation, and death [21], but EUS-FNA is necessary for smaller tumors or deeply located tumors [22]. While these imaging techniques have effective sensitivities in detecting pancreatic cancer, they are invasive in nature and require a high level of skill. Moreover, these technologies are not approved diagnostic screening.

Research and development for an effective chemotherapy drug treatment for PDA remains challenging with current strategies only providing marginal improvements to patient survival rates. Gemcitabine is the standard care of PDA since 1997, as it led to better results than Fluorouracil (5FU) [23]. Countless studies have investigated combination of other drugs with gemcitabine with minimal improvement to median overall survival (MOS) results (Table 1, [24]). Other chemotherapeutic agents and combinations like FOLFIRINOX (5-fluorouracil, oxaliplatin, irinotecan, and

Table 1. Results from combinational therapies with gemcitabine. Adapted from [24].

Selected randomized Phase III completed trials with cytotoxic combinations.

Study	N	Control arm	Experimental arm	Overall survival, months	P-value	Response rate
Burris (1997) [9]	126	5-FU	Gemcitabine	4.41 vs 5.65	0.0025	4.8% vs 23.8%
E2297, Berlin (2002) [90]	322	Gemcitabine	Gemcitabine, 5-FU	5.4 vs 6.7	0.09	5.6% vs 6.9%
Rocha Lima (2004) [91]	342	Gemcitabine	Gemcitabine, irinotecan	6.6 vs 6.3	0.79	4.4% vs 16.1%
Reni (2005) [10]	104	Gemcitabine	Cisplatin, epirubicin, gemcitabine, fluorouracil	NR	NR	8.5% vs 38.5%
Abou-Alfa (2006) [92]	349	Gemcitabine	Gemcitabine, exatecan	6.2 vs 6.7	0.52	No difference
Oettle (2005) [93]	565	Gemcitabine	Gemcitabine, pemetrexed	6.3 vs 6.2	0.85	7.1% vs 14.8%
Cunningham (2009) [11]	533	Gemcitabine	Gemcitabine, capecitabine	6.2 vs 7.1	0.08	12.4% vs 19.1%
E6201, Poplin (2009) [94]	832	Gemcitabine	Gemcitabine, oxaliplatin	4.9 vs 5.7	0.16	6% vs 9%
GIP-1, Colucci (2010) [95]	400	Gemcitabine	Gemcitabine, cisplatin	8.3 vs 7.2	0.38	10.1 vs 12.9%
PRODIGE, Conroy (2011) [7]	342	Gemcitabine	FOLFIRINOX	6.8 vs 11.2	0.001	9.4% vs 31.6%
MPACT, Von Hoff (2013) [8]	861	Gemcitabine	Gemcitabine, nab-paclitaxel	6.7 vs 8.7	0.001	7% vs 23%
GEST, Ueno (2013) [96]	834	Gemcitabine	Gemcitabine, S-1	8.8 vs 9.7	0.001	13.3% vs 29.3%
MAESTRO, Cutsem (2016) [97]	693	Gemcitabine	Gemcitabine, evofosfamide	7.6 vs 8.7	0.0589	15% vs 19%

Abbreviations: N, number of patients; NR, not reported 5-FU, 5-fluorouracil; GIP-1, Gruppo Italiano Pancreas 1; PRODIGE, Partenariat de Recherche en Oncologie Digestive; FOLFIRINOX, 5-fluorouracil, leucovorin, irinotecan and oxaliplatin; MPACT, Metastatic Pancreatic Adenocarcinoma Clinical Trial; GEST, Gemcitabine and S-1 Trial.

leucovorin) or Abraxane (nab-paclitaxel, an albumin-coated formulation of paclitaxel) have been tested and have shown some success [25, 26]. The combination of gemcitabine and nab-paclitaxel has been shown to increase the intratumor concentration of gemcitabine by roughly three-fold in murine xenograft models [27, 28] and increase the MOS to 8.5 months in clinical trials [29]. These promising results suggest that paclitaxel, a taxane agent, (PTX) could be useful in stopping PDA progression. PTX is one of the most widely used anticancer drugs approved for the treatment of many types of cancer. PTX interferes with cell division by interacting with the polymer form of tubulin and promoting microtubulin assembly. The stabilization of the microtubulin polymers prevents depolymerization, which induces M-phase cell cycle arrest and cell death [30, 31]. PTX side effects include chemotherapy-induced neuropathic pain and mitochondrial dysfunction [32]. Thus, targeted therapy is required to prevent unnecessary pain and side effects in pancreatic cancer patients.

Monoclonal antibodies are typically labeled as magic bullets that are highly specific and capable of delivering deadly payloads. Usually generated through immunization and hybridoma technologies, recent advancements in display techniques, such as yeast, has made generating mAbs simpler. In certain cases, mAbs alone are capable of inducing cytotoxic effects in the tumor, possibly through antibody dependent cell-mediated cytotoxicity (ADCC), down regulation of tumor associated receptors or ligands, or inhibition of signaling pathways critical to tumorigenesis [33]. Alternatively, mAbs can be used to delivery cytotoxic agents to the tumor or visually mark tumors for identification and surgical resection. These antibody direct (drug) conjugates (ADCs) have proven quite

useful recently. There are several phase I and II clinical trials using radiolabeled carcinoembryonic antigen (CEA) to image tumors [34, 35]. Fluorescently labeled mAbs (FmAbs) could assist in complex tumor resections. The margins of the tumor can be efficiently tagged by the FmAbs which can allow lesions to be resected in the liver of mice [36]. Utilization of FmAbs in combination with current PDA imaging techniques can provide a clearer picture before surgical resection and improve overall survival [37]. The use of mAbs for targeted applications is very attractive. A simplified schematic of ADCs can be seen in Figure 1.

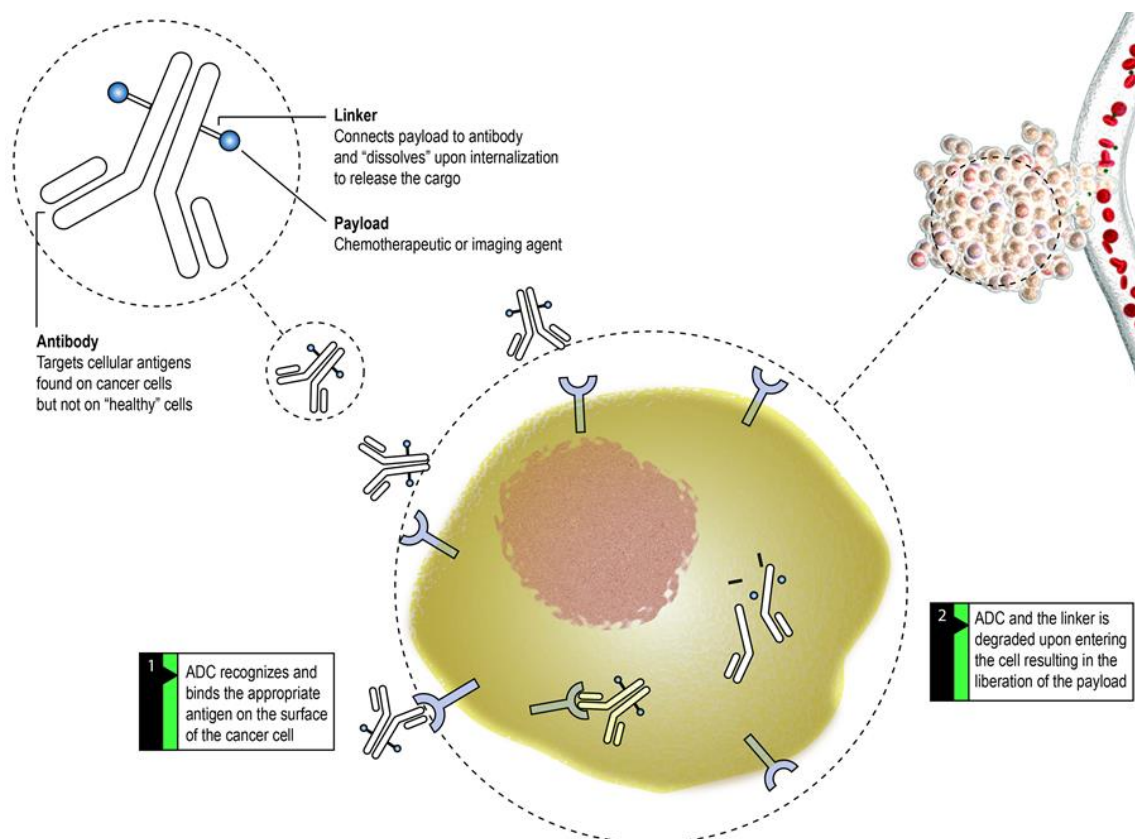


Figure 1. Overall schematic TAB004 conjugation to chemotherapeutic or imaging agent. Anthony J. Fowler, Department of Chemistry, UNC Charlotte (Unpublished)

Several novel targeted therapies involving mAbs developed for PDA have been developed including treatments categorized as targeted therapies with ongoing clinical trials. Epidermal growth factor receptor (EGFR) is transmembrane glycoprotein that forms a receptor for tyrosine kinase [38]. EGFR over expression is associated with tumorigenesis and malignancy in PDA and other epithelial cancers [39]. Afatinib, a novel irreversible EGFR1 inhibitor, in combination with gemcitabine is currently in phase II clinical trials with endpoints to determine overall survival. Carcinoembryonic antigen (CEA) is a glycoprotein that consists of three repeat domains attached to the cell surface of epithelial cells via a glycosylphosphatidylinositol (GPI) anchor and has a role in cell adhesion and signaling [40]. CEA is normally expressed on the luminal surface of epithelial cells, out of reach of monoclonal antibodies. However, in PDA, CEA is overexpressed on both the luminal and basolateral surface membranes. CEA undergoes conformational change when shed from the cell surface and some CEA antibodies can distinguish between normal and tumor antigens in serum. CEA targeting is currently in phase I clinical trials using Cergutuzumab-amunaleukin (CEA-IL2v), a CEA-targeted IL-2 variant-based immunocytokine, in combination with Atezolizumab, a programmed cell death-ligand (PD-L1) antagonist. Cancer antigen 19.9, or sialyl lewis A, (CA19.9-similar to MUC1) is a carbohydrate antigen overexpressed in >90% of patients with pancreatic cancer [41]. It is expressed in extremely low levels in healthy pancreatic tissue as disialyl lewis A [42]. MVT-5873, a humanized CA19.9 antibody, is currently in phase I clinical trials as a monotherapy and combinational therapy with Gemcitabine and nab-paclitaxel to determine maximum tolerated dose. However, while its inability to distinguish between serum and

tumor localized antigen make it a poor candidate for cytotoxic targeting [43], it could still prove useful for diagnosing and monitoring PDA.

Nanoparticles (NPs) are 100 to 100,000 times smaller than human cells that can interact with biological molecules intra and extracellularly, and their use for targeted delivery of cytotoxic agents in PDA is extensive [44]. Nanoparticles can be attached to lipids or form polymers to encapsulate drugs to increase drug solubility, permeability, and delivery to tumor, a common issue with standard chemotherapies [45]. They have the ability to passively target pancreatic cancer in part to the enhanced permeability and retention (EPR) effect, which is caused by the vasculature permeability in tumors being greater than in normal tissues, and thus providing a mechanism for preferential retention of NPs, as they do not penetrate into neighboring normal tissue [46, 47]. The unorganized structure of the tumor and lack of lymphatic drainage prolong the retention of NPs following extravasation from the leaky vasculature [48]. The size of nanoparticles can be adjusted so that they are small enough to escape phagocytosis by Kuffer cells and splenocytes, and small enough to evade filtration by the kidneys. However, their non-physiological surface chemistry can cause non-specific targeting and precipitation leading to cell damage [44, 49]. To address this issue, active targeting of tumor cells by combining specific recognition patterns such as antibodies to nanoparticles that increase the efficiency of nanoparticles in poorly leaky tumors [50]. The formulation of the NPs is also key and polymeric NPs modified to degrade in the tumor microenvironment. Surface targeting of tumor antigens is a promising platform for targeted drug delivery [51-54].

Mucin-1 (MUC1, Fig. 2 [55]), is a transmembrane protein with a heavily glycosylated extracellular domain [56]. Normal expression of MUC1 can be found on epithelial cells of the mammary gland, esophagus, stomach, duodenum, uterus, prostate, lung, and pancreas and other glandular epithelial organs [57]. The negatively charged glycosylated extracellular domain of MUC1 in normal healthy tissues creates a physical barrier and an anti-adhesive surface, preventing pathogenic colonization [58]. The MUC1 gene encodes a singly polypeptide chain that is cleaved immediately after translation into two fragments: the larger N-terminal subunit (MUC1-N) and the shorter C-terminal subunit (MUC1-C), which are associated through stable hydrogen bonds (Fig. 2, [55]).

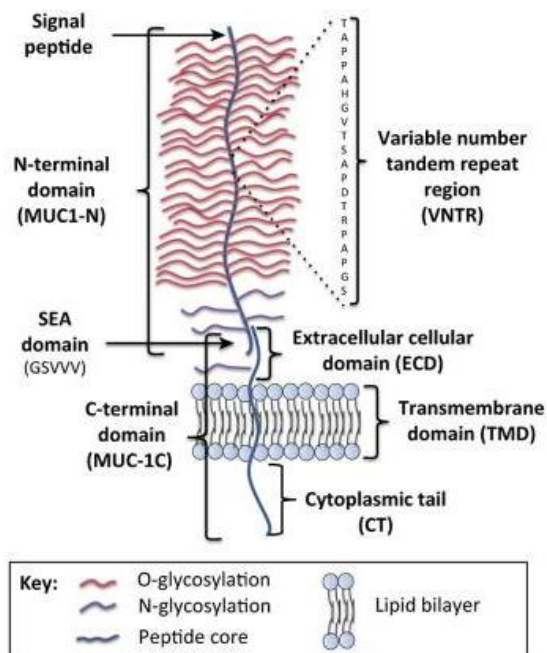


Figure 2. Schematic representation of the structure of MUC1. The N-terminal subunit (MUC1-N) and C-terminal subunit (MUC1-C) of MUC1 associate around the SEA domain, forming a stable heterodimeric complex. MUC1-N contains the signal peptide, variable number tandem repeat (VNTR) region, and SEA domain. The VNTR region of MUC1-N is composed of 20 amino acids that are extensively O-glycosylated (red) at the serine and threonine residues. MUC1-N and MUC1-C are sparingly N-glycosylated (violet) at asparagine residues. The C-terminal domain (MUC1-C) consists of the extracellular domain (ECD), transmembrane domain (TMD), and CT. Adapted from [55].

The MUC1-N subunit contains a variable number tandem repeat (VNTR) region consisting of 20-21 amino acid repeats [59]. However, in 80% of PDA, MUC1 undergoes a transformation into tumor-associated MUC1 (tMUC1) where the extracellular domain of MUC1 is hypoglycosylated and the protein overexpressed [60]. There is also a loss of cell polarity, similar in the case of CEA, that triggers tMUC1 to be redistributed over the cell surface, coming in contact with cell surface growth factors that normally would be restricted to the basolateral surface of epithelial cells, and within the cytoplasm (Fig. 3, [55]). This alteration of the structure and expression of MUC1 is associated with higher metastasis and poor prognosis [61, 62] but also makes it a good tumor antigen to target [63].

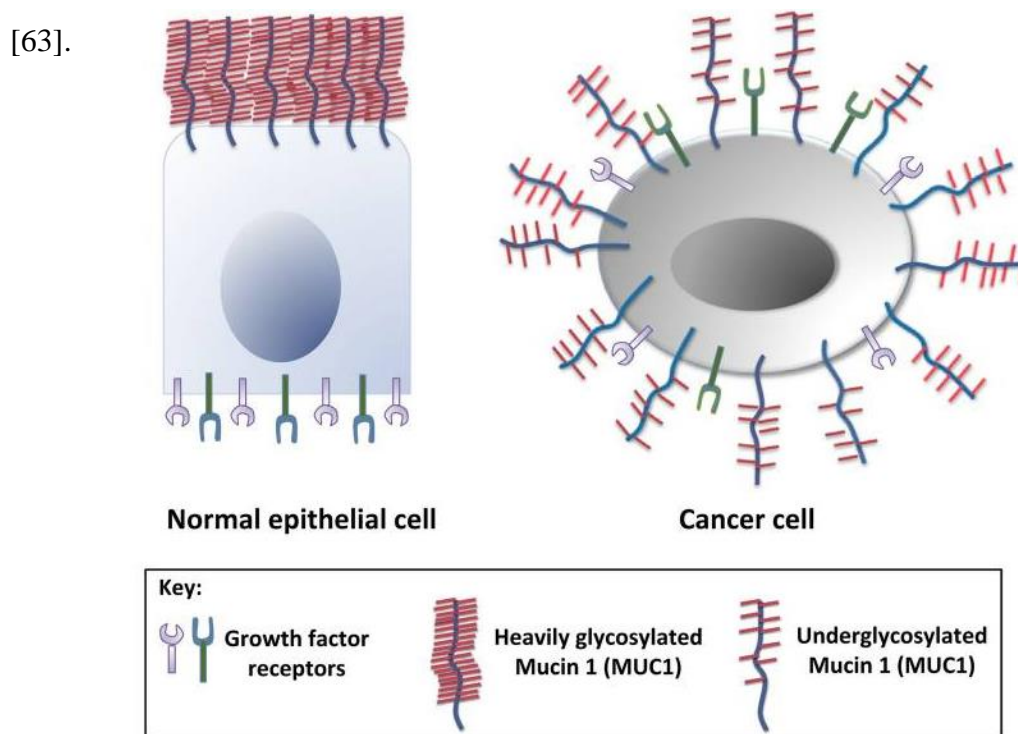
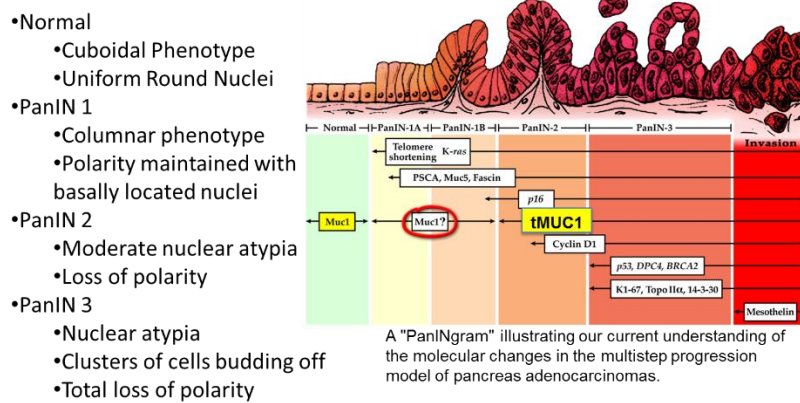


Figure 3. MUC1 overexpression and loss of polarity in cancer cells. MUC1 and growth factors are confined to the apical surface and basolateral surface of normal epithelial cells, respectively. However, tumor cells lose apicobasal polarity, and hypoglycosylated MUC1 is overexpressed all over the surface of the tumor cells, often in close proximity to the growth factors and their receptors. Abbreviation: MUC1, Mucin 1. Adapted from [55].

Several clinical monoclonal antibodies (mAbs) have been developed for MUC1. HMFG and PankoMab are murine based mAbs that recognize the Pro-Asp-Thr-Arg (PDTR) peptide sequence in the VNTR region of MUC1- N [64], but PankoMab recognizes the glycosylated form of the peptide [65]. For treatment in humans, mAbs should be humanized as mouse antibodies can induce an immune response and less efficient in recruiting human effector functions [66]. Although consideration should be taken when determining which human IgG subtype (hIgG) to humanize the mAb on for testing in mice. It has been shown that hIgG1 and hIgG2, the most studied mAb isotypes, recruit murine effector cells differently, with IgG1 activating mouse macrophages [66]. Both of these antibodies have been humanized and the use of HMFG is currently being investigated for breast cancer treatment. Another MUC1 specific mAb, HuC242 (Cantuzumab in its tumor-activated prodrug form) binds to a novel glycoform of MUC1 (CanAg) [67] and has been tested in clinical trials as well. PAM4, originally thought to target MUC1, actually targets MUC5AC [68].

The Mukherjee lab and others have recently described the first mouse model of pre-invasive and invasive ductal pancreatic cancer that recapitulates the full spectrum of human PanINs, putative precursors to pancreatic cancer (as illustrated in Fig 4.[69]). The PanINs are highly proliferative, show indications of histological progression, and trigger signaling pathways normally inactive in normal ductal epithelium [70, 71]. Mice developed ductal lesions with complete penetrance (100%), very similar to all three stages of human PanINs. (PanIN-1A, PanIN-1B, PanIN-2, and PanIN-3) and expresses human MUC1 [71]. Between four and six months of age, all mice developed PanINs of different stages including PanIN-

IA, - IB, -2 and -3. By 7-10 months, 82% of the pancreas was found to be neoplastic, with a few mice developing invasive ductal adenocarcinoma (PDA) at 12 months of age. These models allow the exclusive capability to fully target tMUC1 as tumor progresses from preneoplasia to PDA.



Adopted from: *Maitra A et al, Modern Pathology 2003, 16:607*

Figure 4. A “PanINgram” illustrating progression of normal cellular arrangement through PanIN lesion stages. Adapted from {69}.

Although many xenograph or transplantable tumor models have been utilized, the most effective studies are directed against spontaneous tumors. These models are clinically relevant as tumors arise in an appropriate tissue background and in the context of a viable immune system. This allows the testing of human MUC1-targeted therapies in a MUC1-tolerant host. Although a few MUC1-directed clinical trials have been conducted in patients with pancreas cancer, clinical benefits have been limited. Clinical trials must be preceded by appropriate animal studies to demonstrate that the concepts can be translated into efficacious therapy for cancer.

I will utilize the human MUC1-expressing transgenic mice that exhibit B- and T-cell compartment tolerance and are refractory to immunization with the protein encoded by the transgene [72]. Since its own promoter drives the human MUC1 transgene, the

expression levels are tissue-specific. Crossing the PDA mice to the MUC1.Tg allow the evaluation of targeted imaging and therapeutics in pancreatic cancer in an relevant model.

Generation of the mice is shown schematically (Fig 5). The PDA mice (designated KC mice in the dissertation) were mated to the human MUC1.Tg mice to generate the PDA.MUC1 mice also designated as KCM mice in the dissertation. KCM and KC cell lines were derived from these spontaneous primary tumors and, therefore, are syngeneic for the C57BL/6 background and MUC1.Tg mice. Similarly PDA mice were mated to Muc1KO mice to generate KCKO mice and tumor cells derived from these mice are designated KCKO cell that are devoid of MUC1 [73].

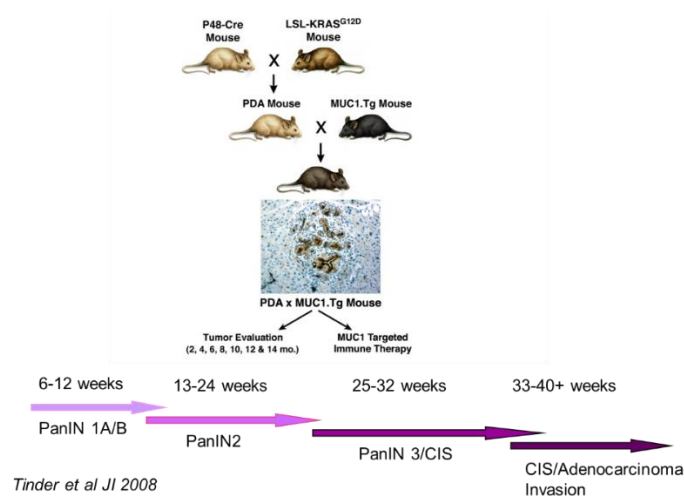


Figure 5. Diagram showing generation of KCM mice used in this dissertation. Adapted from {71}.

This dissertation investigates the ability of a novel monoclonal antibody, TAB004 (OncoTab, Inc., Charlotte, NC), which specifically targets the hypoglycosylated/tumor-associated form MUC1 (tMUC1) [74, 75] in PDA. I present data using TAB004 a) to

detect PDA in murine orthotopic tumor models and in PanIN lesion in mice that developed PDA spontaneously (Chapter 2), and b) to deliver drugs and increase drug accumulation of polymeric NPs at the PDA tumor site (Chapter 3). These two factors can impact the overall survival of patients before and after they are diagnosed with PDA. While this work focuses on PDA, the data shown here may be applicable to other epithelial cancers, given that tMUC1 is overexpressed in most of them [76]. Following the discussion, this dissertation also introduces a supplemental chapter that details preliminary work into characterizing TAB004 stability *in vivo* and tMUC1's role in micropinocytosis.

CHAPTER 2: IMAGING AND EARLY DETECTION OF PANCREATIC CANCER BY ANTI-MUC1 ANTIBODY, TAB004

2.1 Introduction

The poor prognosis for patients is mainly due to late diagnosis, as a result of the lack of distinct early symptoms and effective diagnostics [6]. Only 15-18% of pancreatic cancer cases are resectable, and surgery offers the only single modality for potential cure. These patients have a two-year survival rate of 20% – 40% with surgery, but despite surgical resection, local recurrence or metastasis occurs in more than 50% of the patients (predominantly liver and peritoneum). Overall survival from PDA is only possible with surgery and adjuvant treatment when detected early [11, 12]. Thus, development of an effective and targeted detection platform is essential in order to improve the survival of PDA patients. Infiltrating PDA accounts for over 95% of all exocrine pancreatic malignancies. Activating mutations in the KRAS proto-oncogene are found in over 90% of invasive PDA and are thought to represent an initiating event. Recently a transgenic mouse model has been created that expresses physiological levels of oncogenic KRAS with a glycine to aspartate substitution at codon 12 (KRAS^{G12D}) in the progenitor cells of mouse pancreas. These mice develop the full spectrum of pancreatic ductal adenocarcinoma from preinvasive neoplasias (PanINs) to invasive and metastatic disease (designated as the Cre-LSL-KRAS^{G12D} or PDA mice).

I have generated the PDA.MUC1 mice by breeding the Cre-LSL-KRAS^{G12D} to a human MUC1.Tg mice (designated KCM mice) that develop the entire spectrum of PanIN lesions and adenocarcinoma mimicking the human disease [71] and cell lines from these KCM mice (KCM cells) [62, 73, 77] are utilized with a novel monoclonal antibody,

TAB004 (OncoTAb, Inc., Charlotte, NC), specifically targets the hypoglycosylated/tumor-associated form of MUC1 (tMUC1) [74, 75, 78, 79].

Using the syngeneic KCM cells, I demonstrate that TAB004 specifically binds to tMUC1 expressing orthotopic KCM tumors in immunocompetent mice. Further, I show that TAB004 specifically targets the pancreas in the spontaneous tumor model (the KCM mice) at the early PanIN lesion stage much before the development of invasive PDA. I show that accumulation of TAB004 is significant at the tumor site but not so at other glandular epithelial organs. This data suggests that TAB004 can be further developed as a diagnostics imaging tool for early detection of PDA.

2.2 Methods

The KCM cells was derived by the Mukherjee group from spontaneous PDA tumors obtained from KCM mice. The KCM cells expresses both mouse Muc1 and human MUC1 and are maintained in Dulbecco's modified Eagle's medium (DMEM, 11965-092, Gibco, Waltham, MA). KCM-Luc cell line was generated by retroviral transduction of KCM cells with MSCV Luciferase PGK-Hygro (MSCV Luciferase PGK-hygro was a gift from Scott Lowe, Addgene plasmid # 18782, Cambridge, MA) was performed by transfecting GP2-293 cells with the MSCV Luciferase PGK-Hygro and pVSV-G vectors and using the obtained viral supernatant to infect KCM cells. Growth media for these cell lines were supplemented with 10% fetal bovine serum (FBS, Gibco, Waltham, MA), 3.4mM L-glutamine, 90 units (U) per ml penicillin, and 90 μ g/ml streptomycin (Cellgro, Corning, Manassas, VA).

TAB004 antibody (patent US 8518405 B2 and US 9090698 B2 provided by OncoTAb. Charlotte, NC) is a specific Ab to tMUC1 [8, 78-80]. Murine TAB004 (mTAB004), is a mouse IgG1 monoclonal antibody and chimeric TAB004 (cTAB004) is a chimeric IgG1 antibody with mouse ScFv and human Fc regions. The production of TAB-004 is currently conducted by LakePharma Inc., Belmont, CA.

TAB004 conjugation to indocyanine green (ICG) was performed using the ICG Labeling Kit –NH₂ (LK31-10, Dojindo Molecular Technologies, Inc., Washington, D.C.). All conjugations were performed according to manufacturer protocols.

Tumor/pancreas sections were treated with NucBlue Fixed Cell ReadyProbes Reagent (ThermoFisher, Waltham, MA) for 5 minutes and Wheat Germ Agglutinin-488 (Molecular Probes, Waltham, MA) for 20 minutes. The slides were then washed with PBS for 5 minutes (3x) and fixed with 4% formaldehyde. Prolong Gold Antifade reagent with DAPI (P36935, Molecular Probes, Waltham, MA) was applied to mount coverslips. Images were acquired on an Olympus Fluoview FV 1000 confocal microscope.

C57Bl/6 mice were purchased from Jackson Laboratory and housed at UNC Charlotte's vivarium. For the orthotopic tumor model, C57/Bl6 female mice were injected in the pancreas with 5×10^5 KCM-Luc cells and allowed to recuperate for 7 days before any experiments were performed. For tumor and antibody visualization, orthotopic KCM-Luc tumor bearing C57/Bl6 mice were injected with 125 μ l of Redijet D-Luciferin (760504, Perkin Elmer, Waltham, MA) intraperitoneally and imaged 25 minutes later. For groups injected with antibody, 12.5 μ g of IgG1 Isotype conjugated to ICG or TAB004 conjugated to ICG was injected intraperitoneally and imaged 1 minute, 14 hours, and 24 hours post injection with a Perkin Elmer IVIS Spectrum. KCM mice were generated in the Mukherjee

lab. This mouse model is a triple transgenic cross of LSL-KRASG12D x P48-Cre x Human MUC1.Tg that will develop PDA spontaneously and express human MUC1 in a tissue specific manner [71]. The P48-Cre mice have a tamoxifen inducible promoter and therefore, oncogenesis is initiated only when mice are treated with tamoxifen (75 mg/kg in 100ul of corn oil, 1 injection per day for 10 days, T5648-1G, Millipore Sigma, St. Louis, MO) as recommended by Jackson labs (<https://www.jax.org/research-and-faculty/tools/cre-repository/tamoxifen>). Mice were euthanized following IVIS imaging studies. All procedures were conducted in accordance to the Institutional Animal Care and Use Committee of UNC Charlotte.

All fluorescent slide images were analyzed using Image-J (National Institutes of Health, Bethesda, Maryland). All mice and organ images were processed in Living Imagine 4.3.1 (Caliper Life Sciences, Waltham, MA).

The pancreases of KCM mice were collected and samples fixed in buffered formalin and embedded in paraffin, and 5- to 6- μm -thick sections were obtained. Standard H&E staining protocol was performed and the tissue slides were then assessed by light microscopy, and microphotographs were taken using a DP70 camera and the Olympus Software Suite (Olympus, Waltham, MA)

2.3 Results

Four control groups were imaged alongside TAB004 injected groups. Radiance efficiency (RE, $[\text{p}/\text{sec}/\text{cm}^2/\text{sr}]/[\mu\text{W}/\text{cm}^2]$) values were collected using the Region of Interests (ROIs) for all images.

Control group 1 comprised of normal C57/B16 mice with nothing injected that had their organs imaged using the IVIS (Fig. 6). The purpose of Control group 1 was to

determine background fluorescence (of ICG) levels in C57/Bl6 mice (Fig. 14). Background fluorescence of the open cavity of the mice (in-situ) where the tumor is normally located (Fig. 6A) and each organ (Fig. 6B) is shown. The remaining imaging groups would use the radiance efficiency values from Control group 1 for background normalization.

Control group 2 comprised of normal C57/Bl6 with orthotopic KCM-Luc tumors (Fig. 7). This group is to determine the RE of KCM-Luc tumor by itself without injection of TAB004-ICG. The KCM cell line is a syngeneic mouse PDA cell line that expresses high levels of tMUC1 [62, 79, 81, 82] and therefore a good target for *in vivo* TAB004 [75]. Post luciferin injection, bioluminescent imaging in live mice confirmed the presence of KCM tumor 7 days post KCM challenge (Fig. 7A). Representative image with n=3 mice is shown. Following imaging of the live mice, mice were euthanized and the organs of the mice *in-situ* photographed confirming the location of tumor in the pancreas (Fig. 7B). Additionally, IVIS images confirmed that KCM tumors (Fig. 7C) do not auto fluoresce. RE values of organs from Control group 2 were recorded (Fig. 7D) and compared with RE values of Control group 1. There was no significant increase in RE values between in-situ and organ images of Control group 1 and 2 (Fig. 14), therefore background RE values do not increase if an orthotopic tumor is present.

For control group 3 and 4, I assessed whether a control IgG isotype antibody conjugated to ICG would accumulate in any regions of the mice. Control group 3 consisted of normal non-tumor bearing C57/Bl6 mice injected with IgG1-ICG (Fig. 8). ICG images taken 24 hours post injection of the IgG1-ICG showed fluorescent signal similar to the background of the control (Fig. 8A). 24 hours post injection (PI) time point was selected based in vivo ICG-TAB004 data showing complete disappearance of fluorescence signal

by 48hours (data not shown). Open cavity (Fig. 8B) and organ (Fig. 8C) ICG RE values display no significant increase over values of Control group 1 or 2 (Fig. 14). Control group 4 comprised of orthotopic KCM tumor-bearing C57/Bl6 mice injected with IgG1-ICG (Fig. 9). Live ICG images taken 24 hours after injection of the IgG1-ICG showed no significant increase in fluorescence at the tumor site (Fig. 9A). Additionally, no significant increase in RE values from open cavity (Fig. 9B) and organ (Fig. 9C) images was observed between all the control groups (Fig. 14). Therefore, the injection of an isotype control antibody with ICG does not increase background ICG RE values and any increase in ICG RE values seen in TAB004-ICG injected mice can be unequivocally taken as true accumulation of TAB004 at tumor region.

Murine monoclonal TAB004 antibody. The first treatment group consisted of KCM tumor-bearing C57/Bl6 mice injected with mTAB004-ICG (Fig. 10 and 11). Live ICG images taken as early as 1 minute post injection (PI) show accumulation of the mTAB004 at the tumor site (Fig. 101A). The accumulation appears to increase 14 hours PI but decreases after 24 hours (Fig. 10A). Live bioluminescent image of the same mouse confirm the location of the tumor (Fig. 10B). In-situ photograph (Fig. 11A) confirms the location of the tumor and IVIS images show significant accumulation of mTAB004-ICG at the tumor site (Fig. 11B). The larger region of red-yellow fluorescence indicates accumulation of mTAB004 at the tumor (Fig. 11B). Significant increases in RE values (Fig. 11C) was observed in the pancreatic tumor, liver, small intestine, and spleen (Fig. 14) which indicates the accumulation of mTAB004 selectively in those organs. RE values at the tumor site was ~ 3.5 fold higher and ~2 fold higher at the liver and small intestine site compared to the control groups (Fig 14). The increase in RE values in the liver is expected [83] from an

IgG antibody. While the increase in RE values in the small intestines and spleen would suggest mTAB004 accumulation at the organs, and could be explained by some residual tumor in those organs that could not be completely dissected from the organ. Taken together, mTAB004 showed high specificity to the tumor and proves to be useful for detection of PDA by imaging.

Chimeric TAB004. Due to promising results with mTAB004, a chimeric version of the antibody was generated. A shift to humanize the antibody is essential for further development of any antibody-based targeted imaging for diagnostics or for targeted therapy. I acquired a chimeric version of TAB004, cTAB004, which comprises of murine antigen recognition moiety in a human IgG1 backbone. KCM orthotopic tumor-bearing C57/Bl6 mice were injected with cTAB004-ICG (Fig. 12 and 13). Similar to the mTAB004-ICG (Fig 10), live ICG images taken as early as 1 minute post injection show accumulation of the cTAB004 at the tumor site (Fig. 12A). The accumulation increases 14 hours PI but decreases post 24 hours (Fig. 12A), similar to mTAB004 injected mice. Live bioluminescent image of the same mouse confirm the location of the tumor (Fig. 12B). In-situ photograph of a cTAB004 injected mouse confirms the location of the tumor (Fig 13A). IVIS in-situ image shows accumulation in the tumor and few other organs (Fig. 13B). Dissected organs were imaged separately by IVIS to calculate the RE. The larger region of red-yellow fluorescence indicates accumulation of cTAB004 at the tumor (Fig. 13B). Significant increases in RE values was observed in the pancreatic tumor, liver, and small intestine (Fig. 14); however, unlike mTAB004, there was minimal accumulation of the cTAB004 in the spleen. RE values at the tumor were ~ 3.5 fold higher while ~ 0.5 fold higher in the liver and ~2.5 fold higher in the small intestine compared to control RE values

(Fig 14). As with mTAB004, RE values in the liver is expected to be higher [83] with an IgG antibody; however, the liver was significantly lower in the cTAB004 compared to mTAB004 injected mice, possibly due higher uptake of chimeric antibody by macrophages [66]. The RE values of cTAB004 in the small intestines is the same as the mTAB004 treatment group, where residual secondary tumor bodies could not be removed from the organ.

All experiments shown in Figures 7-113 were conducted with n=3 mice per experimental group and representative images from 1 mouse is shown for all groups. Fig. 14 shows the ROI RE values plotted for n=3 mice per group and significance is represented as p value. Tumors from 24h post cTAB004-ICG injected mice were removed, fixed, paraffin embedded, sectioned (4 μ m sections) and imaged under a confocal microscope to determine the cellular localization of cTAB004 ICG (Fig. 15). Tumors from 3 cTAB004-ICG mice are shown alongside a control tumor from mice that were not injected with cTAB004-ICG. Tumor sections from the cTAB004-ICG injected mice display significantly more ICG fluorescent signal (red) than control tumors without TAB004 ICG (Fig. 15A) in all 3 mice. The blue and green fluorescent signals are DAPI (nucleus) and wheat germ agglutinin (membrane) respectively. Red ICG fluorescence was noted within the tumor bed as well as in the edges of the tumor. Most of staining seems to be localized in the surface and cytoplasm of the tumor cells. Green fluorescence suggests the disorganized membrane staining typical of undifferentiated tumors. Quantification of the red fluorescence showed significant increase in the corrected total cell fluorescence (Fig 15B).

Overall, results show that cTAB004 behaves nearly identical to mTAB004 when binding to the pancreas/tumor site, with no loss in accumulation index, which was determined by the RE values (summarized in Fig. 14). Expected accumulation in other organs, besides the liver, was not significantly higher than control groups. cTAB004 is highly specific for the tumor and provides rationale for further development of this platform technology for targeted imaging of PDA..

I determined the specific targeting in an orthotopic tumor model. However, whether this antibody can be developed for early detection of pre-neoplastic lesions prior to the development of PDA remains to be seen. Thus, the Mukherjee group generated KCM mice by crossing the LSL-KRAS^{G12D} with the tamoxifen inducible ^{P48}Cre with the human MUC1.Tg mice [71]. These triple transgenic KCM mice develop spontaneous PDA when induced with tamoxifen. As controls, the Mukherjee group generated KC mice that are double transgenic cross between LSL-KRAS^{G12D} x tamoxifen-inducible ^{P48}Cre mice. KC mice do not express the human MUC1. Tamoxifen was injected in KCM and KC mice to initiate oncogenesis while control KCM mice received no tamoxifen (no oncogenesis). The 3 groups of mice (tamoxifen – induced or un-induced KCM and KC mice) were injected with cTAB004-ICG and imaged 24 hours PI (Fig. 16). Both KC and KCM mice without tamoxifen induction did not display any ICG fluorescence signal in the pancreas from the exterior (Fig. 16A, B left) or open cavity (Fig. 16A, B right) IVIS images where the pancreas was imaged at its original and secondary positions. Secondary position represents moving the pancreas *in situ* using a forceps to confirm that any fluorescence signal is originating from the pancreas and nowhere else. As early as 3-weeks post tamoxifen induction, KCM mice showed ICG fluorescent signal over background from the exterior

(Fig. 16C left) and open cavity (Fig. 16C right) IVIS images. Moving the pancreas from behind the liver and stomach displays a clearer ICG fluorescent signal over background (Fig. 16C far right). Organs from these animals were also imaged with the pancreas possessing the highest level of RE over other organs, similar to the orthotopic tumor model (Fig. 18A). None of the other organs showed fluorescence signal above background levels. Of note, these KCM mice, all other glandular epithelial organs express normal human MUC1 but TAB004-ICG only accumulated in the pancreas post initiation of oncogenesis suggesting the high specificity of TAB004 to transformed/tumor associated form of MUC1. Based on our previous work, I infer that 3-weeks post completion of tamoxifen treatment, the mice present PanIN lesions 1a and b [71]. Additionally, KCM mice 11 weeks post tamoxifen induction, which develop PanIN 2 lesions at this point, were also injected with cTAB004-ICG to determine if it was possible to track disease progression (Fig. 16D). By this time, the pancreas is larger and the TAB004-ICG fluorescent signal shows accumulation at the pancreas as well. Moving the pancreas from its primary location provides a clear image of the TAB004-ICG signal in the pancreas (Fig. 16D). In contrast, the control KCM that received no tamoxifen and tamoxifen-induced KC mice at the same age showed no TAB004-ICG fluorescence in the pancreas or any other organ (Fig. 18B). Together this data clearly suggests that cTAB004-ICG is binding to tMUC1 at very early stages in PDA initiation (at the early PanIN stage) and is effective in tracking disease over time. All images are representative of n=3 mice per group. Finally, H&E section of the pancreas 5, 8, 11, 22, and 33 weeks post tamoxifen injection confirms the formation of abnormal ducts at 3 weeks and PanIN lesions as early as 8 weeks (Figure 17).

2.4 Conclusions

Our results from the orthotopic tumor model demonstrate that TAB004 is highly specific in targeting the PDA tumor and does not accumulate in other organs besides the liver. The significant increase in RE within the pancreas/tumor in mTAB004 and cTAB004 injected groups clearly demonstrates the retention of the targeting antibody. Furthermore, I confirm that TAB004-ICG accumulates in the margins and within the pancreatic tumor bed (Fig. 10). Finally, I utilized a genetically engineered mouse model that spontaneously induced human tMUC1-positive pancreatic cancer (in KCM mouse) (Fig 11-13). The data from the KCM mice show that TAB004 can target tMUC1 being expressed in the pancreas before PDA develops. Examination of the pancreas from KCM mice show no evidence of a primary tumor, but IHC sections from these mice show the presence of PanIN 2 lesions. The results will be further discussed in the dissertation summary (Chapter 4).

2.5 Figures

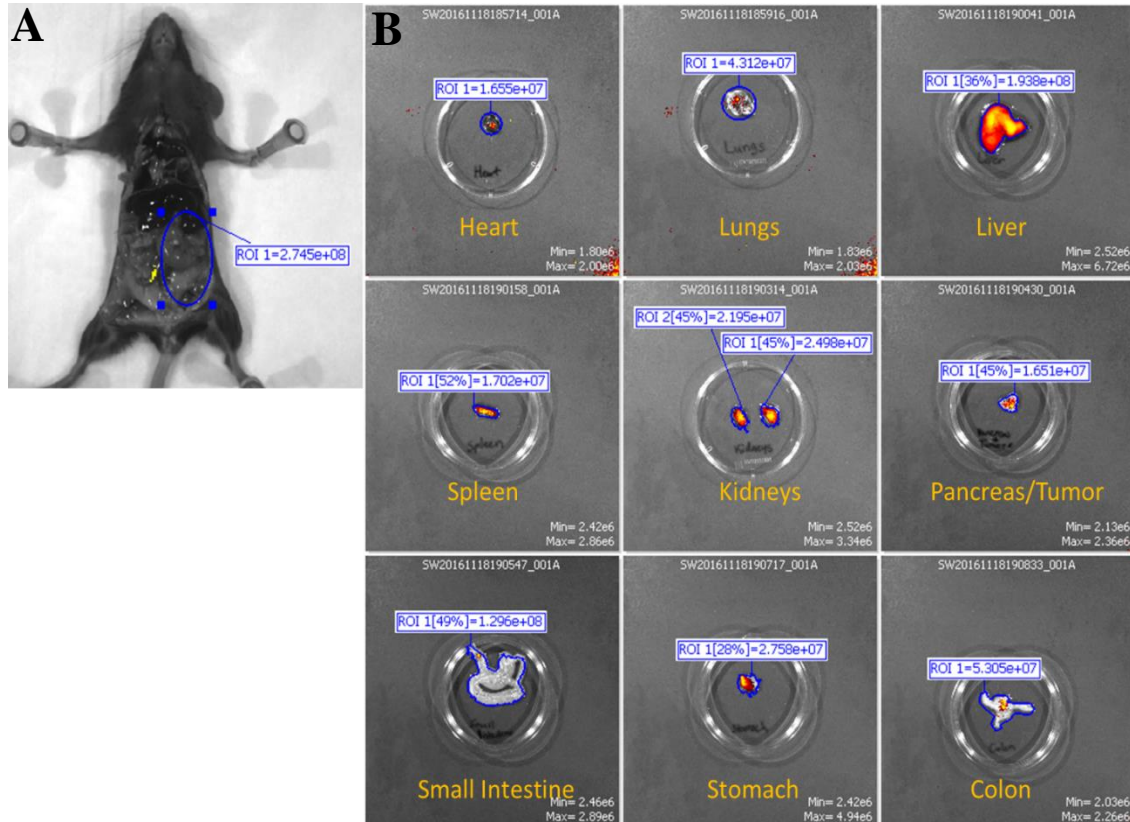


Figure 6. Fluorescent IVIS images of organs from mouse in Control Group 1. Representative images are shown. (A) The mouse is imaged with filter pair ICG on the IVIS Spectrum. Background has been removed and the ROI measurement for the area where tumor would have been present is shown. (B) Organs from mouse are imaged individually in the IVIS Spectrum. Intensity of the red-yellow fluorescence in ROI measurements indicate background levels for each organ.

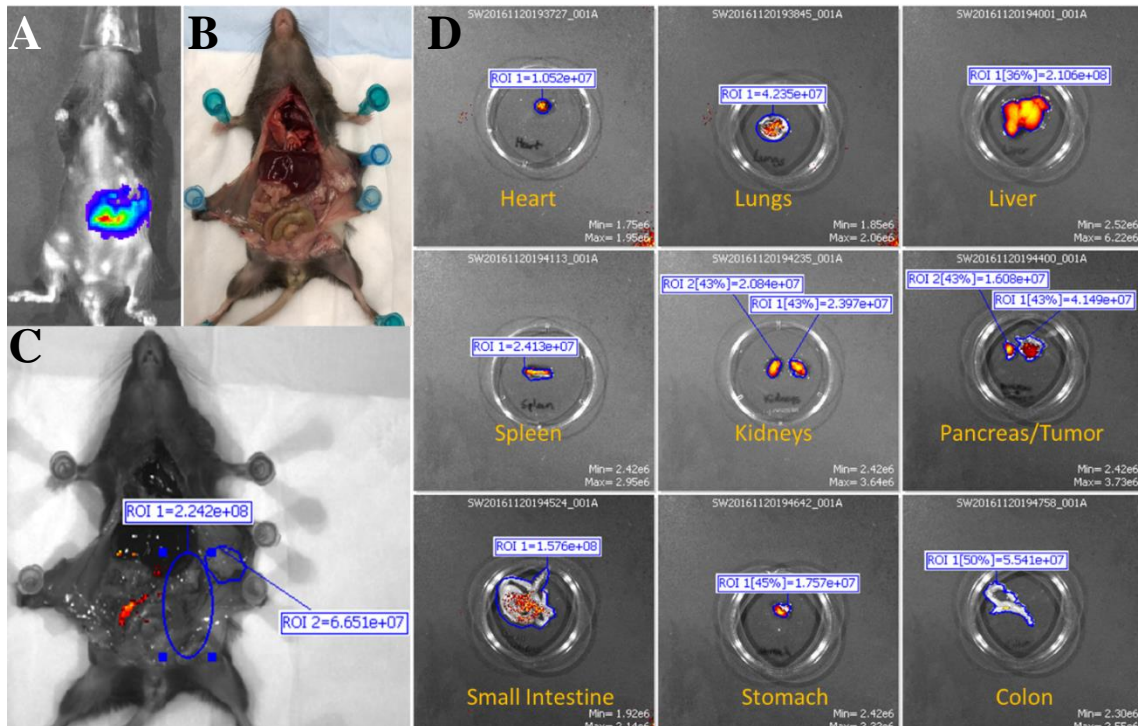


Figure 7. Fluorescent and bioluminescent IVIS images of organs from mouse in Control Group 2. Representative images are shown. (A) Bioluminescent image of tumor. Rainbow indicates tumor site. (B) Photograph images of mouse to show location of tumor. (C) The mouse is imaged with filter pair ICG on the IVIS Spectrum. Background has been removed and the ROI measurements for the area where tumor is present and would have been present are shown. (D) Organs from mouse are imaged individually in the IVIS Spectrum. Intensity of the red-yellow fluorescence in ROI measurements indicate background levels for each organ.

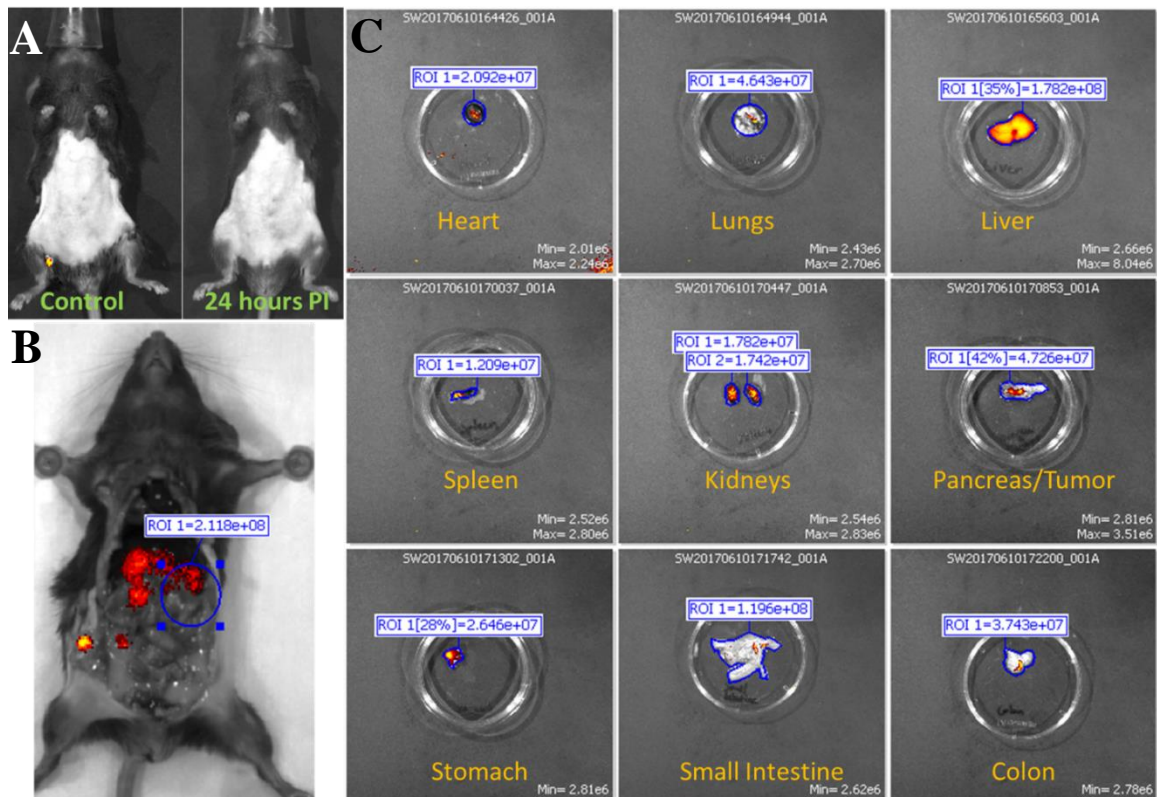


Figure 8. Fluorescent IVIS images of organs from mouse in Control Group 3. Representative images are shown. (A) Fluorescent IVIS image of before (control) and 24 hours post injection of IgG1 conjugated with ICG. 24 hours PI fluorescence is normalized to its own control fluorescence. (B) The mouse is imaged with filter pair ICG on the IVIS Spectrum. Background has been removed and the ROI measurements for the area where tumor would have been are shown. (C) Organs from mouse are imaged individually in the IVIS Spectrum. Intensity of the red-yellow fluorescence in ROI measurements indicate background and antibody accumulation for each organ.

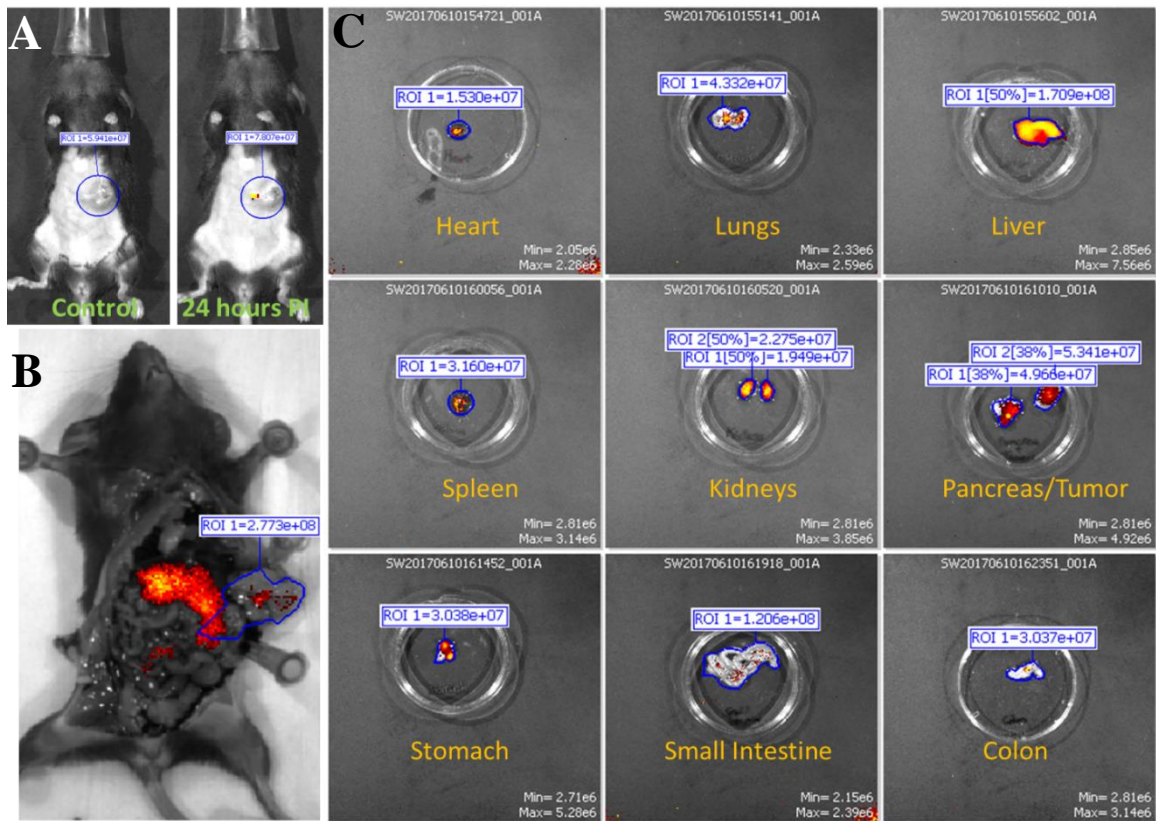


Figure 9. Fluorescent IVIS images of organs from mouse in Control Group 4.

Representative images are shown. (A) Fluorescent IVIS image of before (control) and 24 hours post injection of IgG1 conjugated with ICG. 24 hours PI fluorescence is normalized to its own control fluorescence. (B) The mouse is imaged with filter pair ICG on the IVIS Spectrum. Background has been removed and the ROI measurements for the tumor is shown. (C) Organs from mouse are imaged individually in the IVIS Spectrum. Intensity of the red-yellow fluorescence in ROI measurements indicate background and antibody accumulation for each organ.

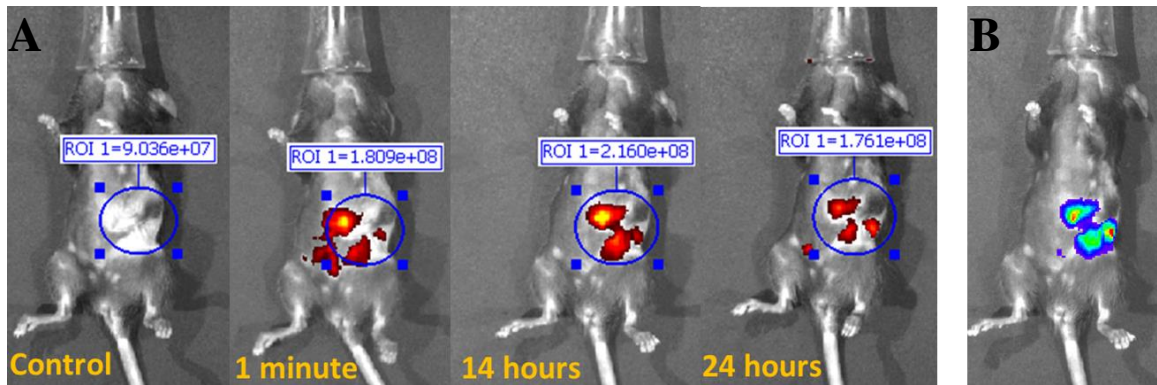


Figure 10. Fluorescent IVIS images taken at different time points of mouse from murine monoclonal TAB004 injected group. Representative images are shown. (A) Fluorescent IVIS image with filter pair ICG of before (control) 1 minutes, 14 hours, and 24 hours post injection of Parental TAB004 with ICG. Fluorescence images taken after injection are normalized to their own control fluorescence. Background has been removed and the ROI measurements for antibody fluorescence is shown. Intensity of the red-yellow fluorescence in ROI measurements indicate background and antibody accumulation. (B) Bioluminescent image of orthotopic tumor in same mouse.

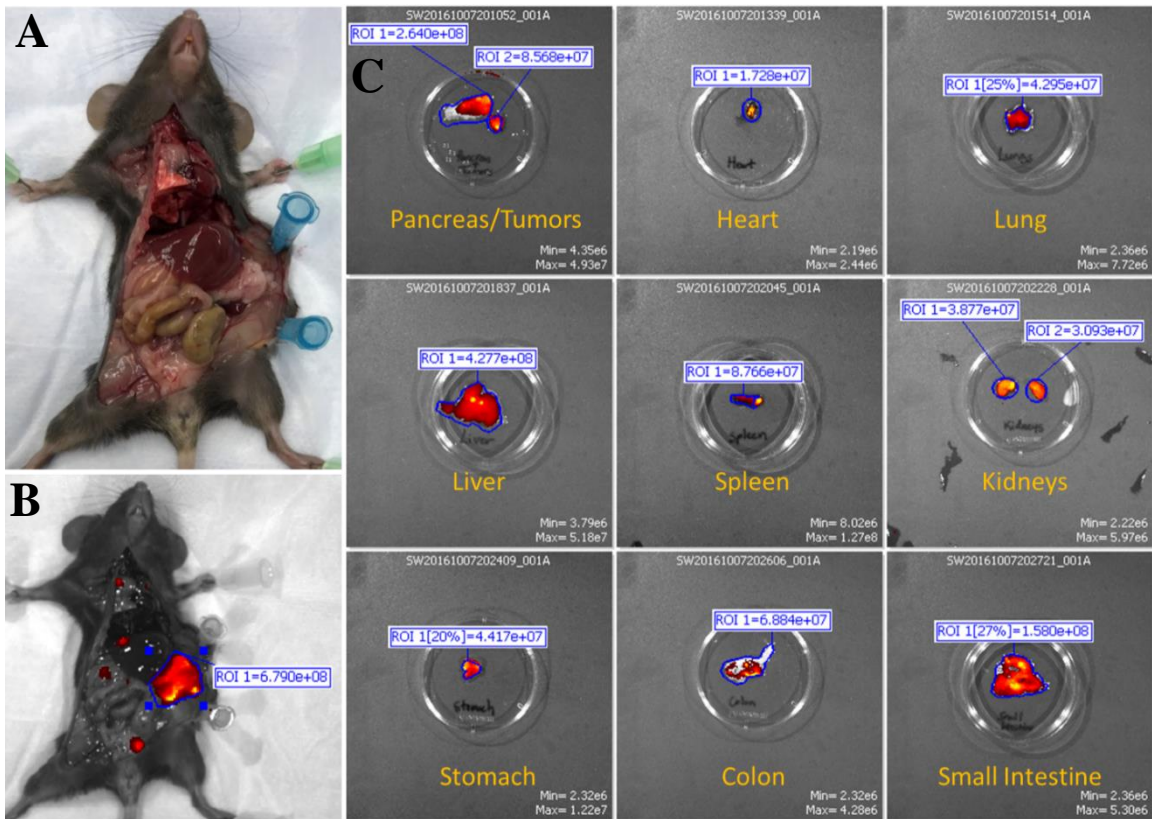


Figure 11. Fluorescent IVIS images of organs from mouse in murine monoclonal TAB004 group. Representative images are shown. (A) Photograph images of mouse to show location of tumor. (B) The mouse is imaged with filter pair ICG on the IVIS Spectrum. Background has been removed and the ROI measurements for the tumor is shown. (C) Organs from mouse are imaged individually in the IVIS Spectrum. Intensity of the red-yellow fluorescence in ROI measurements indicate background and antibody accumulation for each organ.

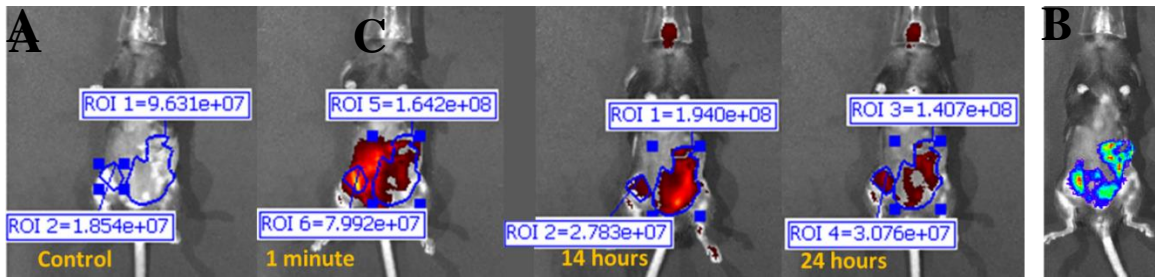


Figure 12. Fluorescent IVIS images taken at different time points of mouse from chimeric TAB004 injected group. Representative images are shown. (A) Fluorescent IVIS image with filter pair ICG of before (control) 1 minutes, 14 hours, and 24 hours post injection of Chimeric TAB004 with ICG. Fluorescence images taken after injection are normalized to their own control fluorescence. Background has been removed and the ROI measurements for antibody fluorescence is shown. Intensity of the red-yellow fluorescence in ROI measurements indicate background and antibody accumulation. (B) Bioluminescent image of orthotopic tumor in same mouse.

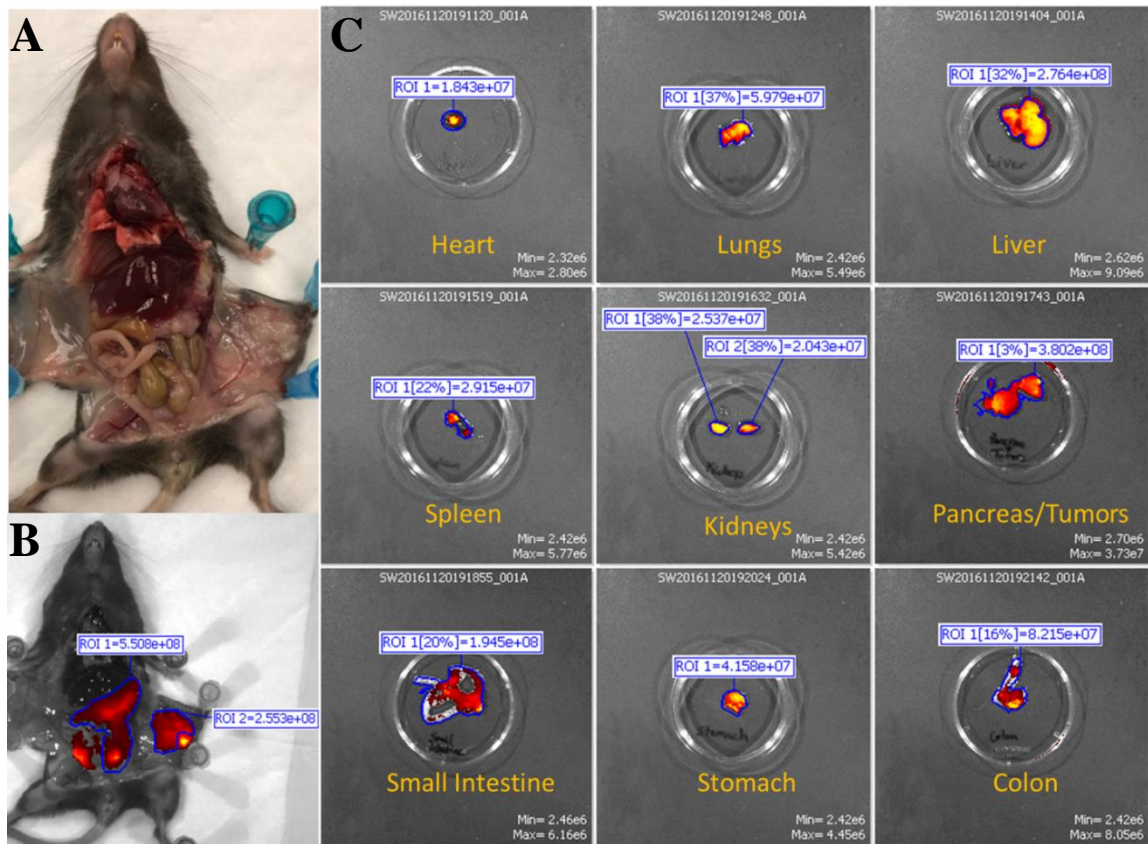


Figure 13. Fluorescent IVIS images of organs from mouse in chimeric TAB004 group. Representative images are shown. (A) Photograph images of mouse to show location of tumor. (B) The mouse is imaged with filter pair ICG on the IVIS Spectrum. Background has been removed and the ROI measurements for the tumor is shown. (C) Organs from mouse are imaged individually in the IVIS Spectrum. Intensity of the red-yellow fluorescence in ROI measurements indicate background and antibody accumulation for each organ.

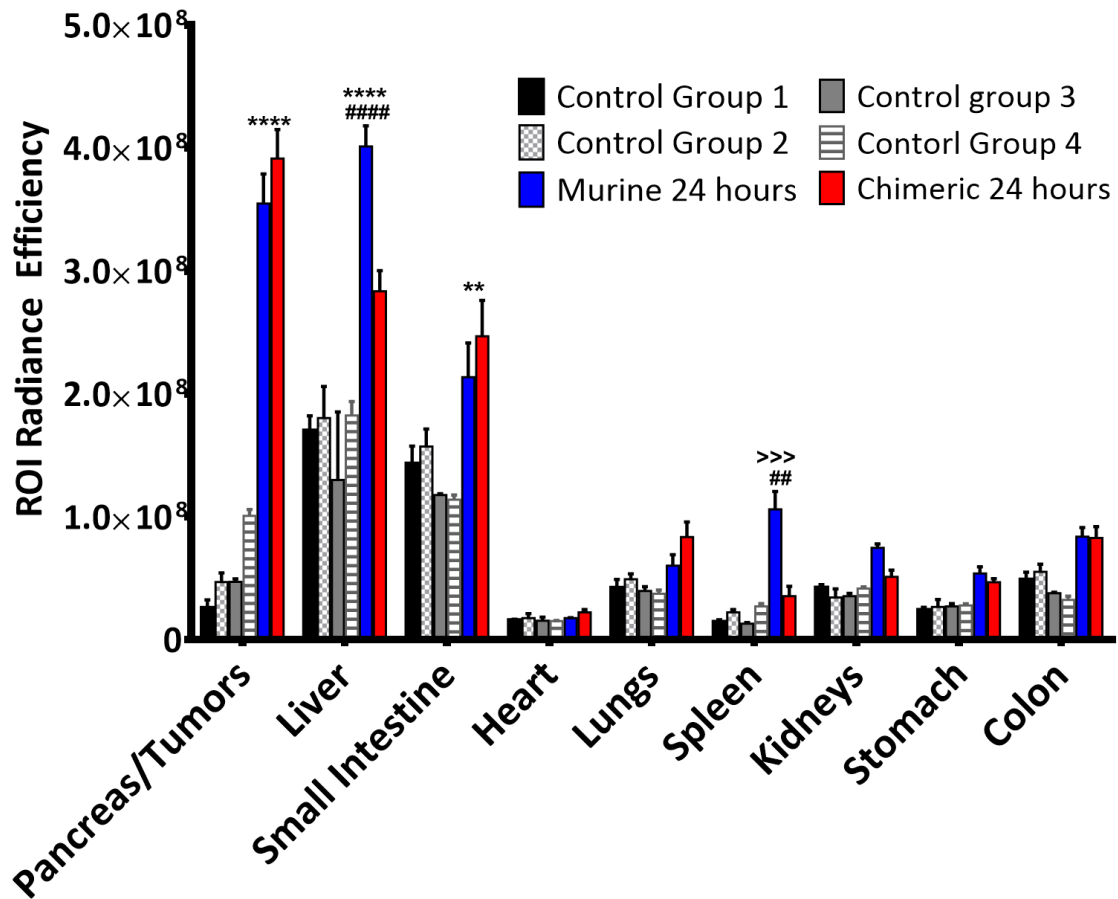


Figure 14. Quantification of ROI values from all groups. The ROI radiance efficiency values for organs from all groups were quantified using Living Image software. * denotes significance between TAB004 (both Murine and Chimeric) and control groups, # denotes significance between Murine and Chimeric TAB004 groups, > denotes significance between Murine TAB004 and other control groups. Data shown is mean \pm SEM (n=3) and determined by 2-way ANOVA with Tukey post hoc test, *p<0.05, **p<0.01, ***p<0.001, ****p<0.0001.

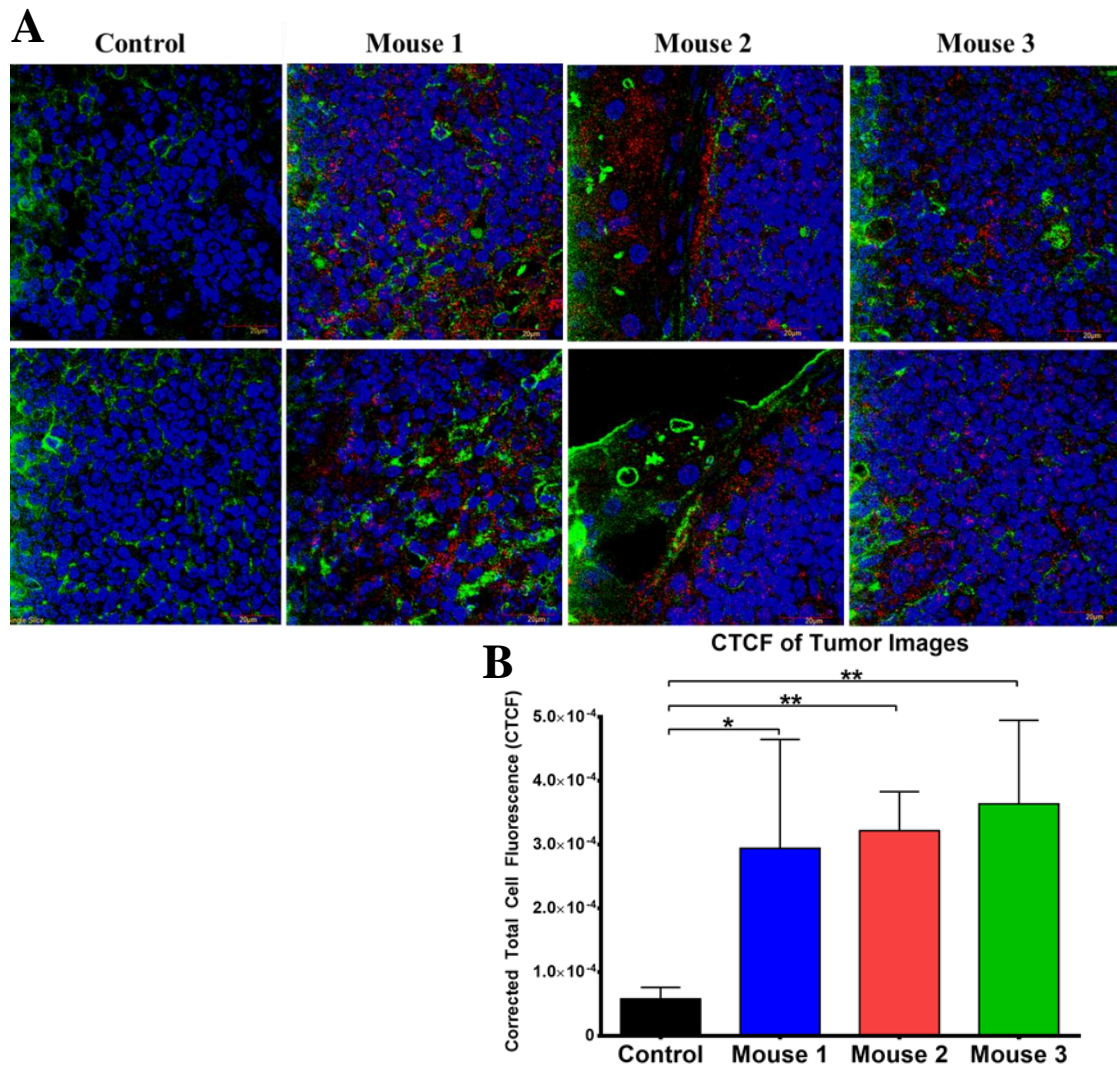


Figure 15. Confocal imaging of tumor sections from Chimeric TAB004 injected mice. Representative images shown. (A) Tumor sections from Chimeric TAB004 injected mice were sectioned into slides imaged. Blue = nucleus (DAPI), Green = cell membrane (Alexa Fluor 488), Red = Chimeric TAB004-ICG. (B) Quantification of fluorescent signal from Chimeric TAB004-ICG using Image J. Data shown is mean \pm SEM (n=3) and determined by unpaired t-test. *p<0.05, **p<0.01

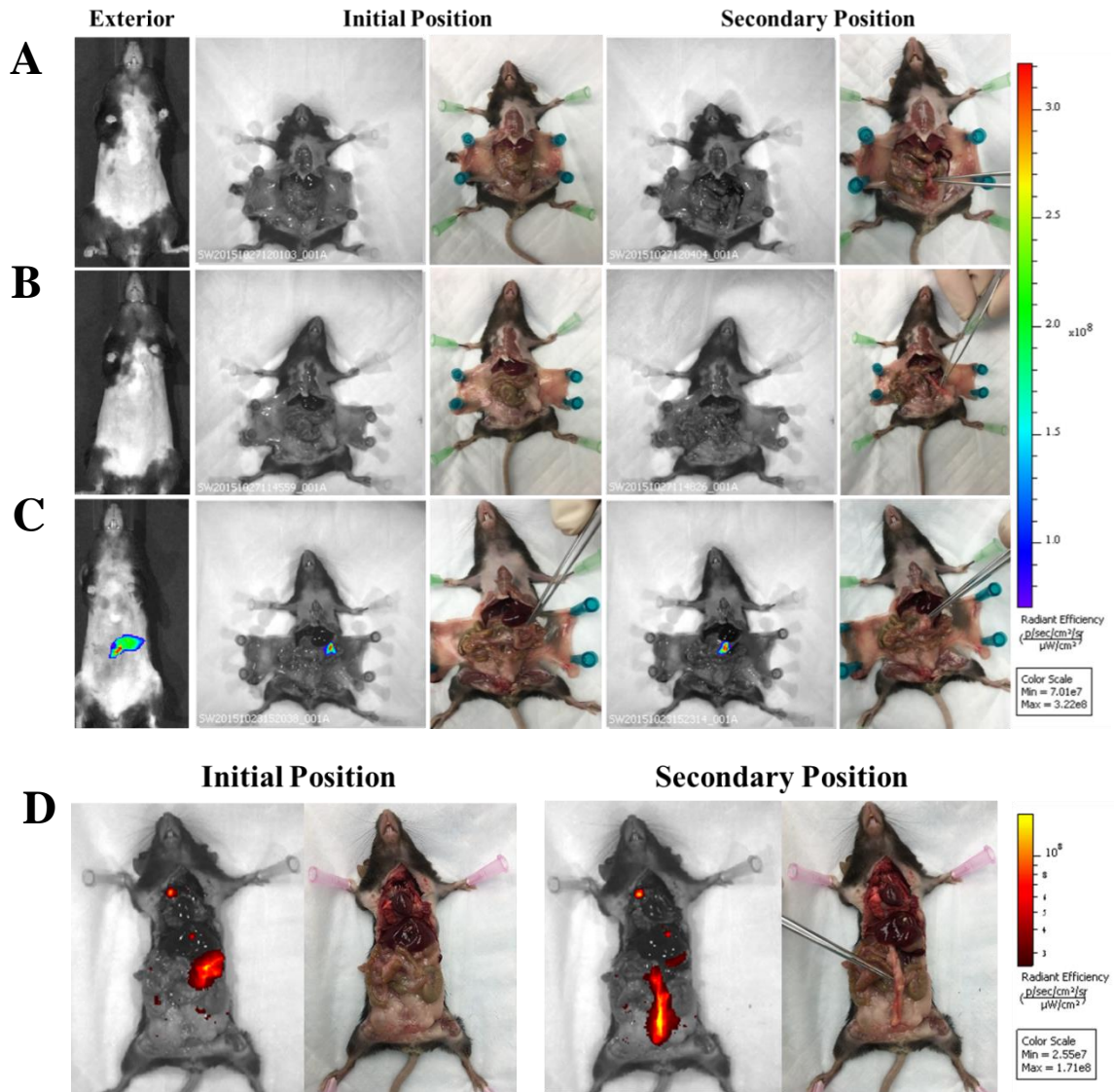


Figure 16. IVIS images of KC and KCM Spontaneous mice (3 and 11 weeks PI of tamoxifen) injected with TAB004. Representative images are shown. Left to Right: Exterior IVIS images with ICG filter pair, IVIS image with ICG filter pair with pancreas in original position, photograph of original position, IVIS image with ICG filter pair with pancreas moved to secondary position, photo graph of secondary position. Forceps indicate location of pancreas. (A) KC mouse (lacks MUC1 transgene). (B) KCM mouse w/o tamoxifen treatment. (C) KCM 3 weeks post tamoxifen treatment. (D) KCM mouse 11 weeks post tamoxifen treatment. Rainbow fluorescence intensity indicates background and antibody accumulation in A-C. Red-yellow fluorescence intensity indicates background and antibody accumulation in D.

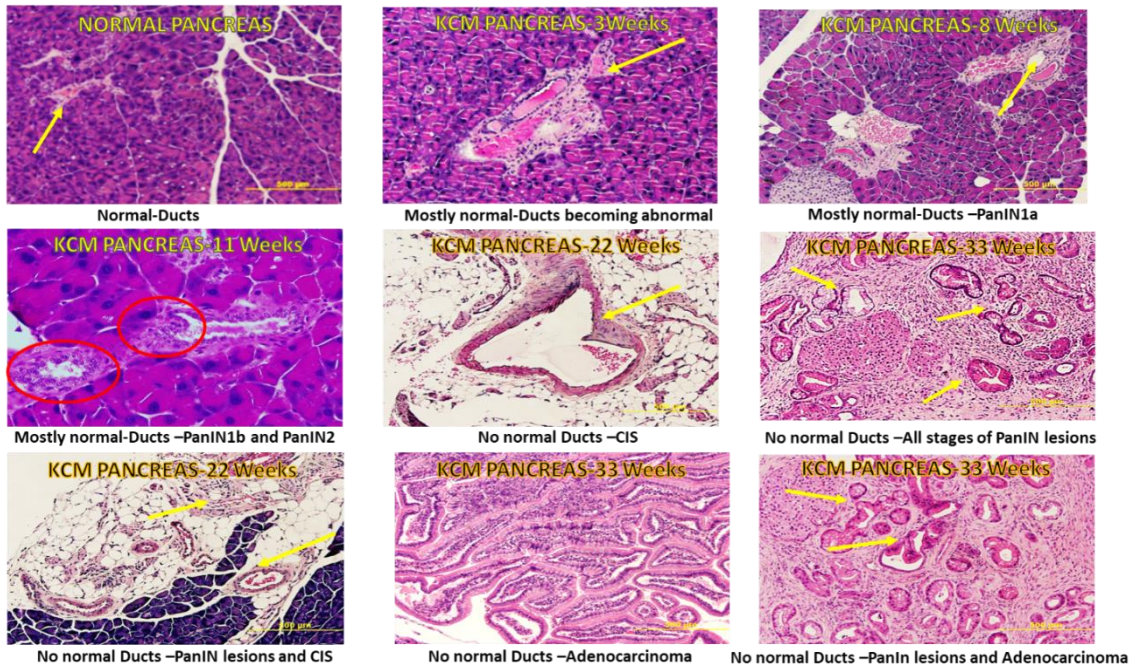


Figure 17. Immunohistochemistry images of pancreas from KCM mice. Representative images are shown. At different weeks post tamoxifen treatment, the progression from abnormal ducts to full adenocarcinoma are identified by H&E staining.

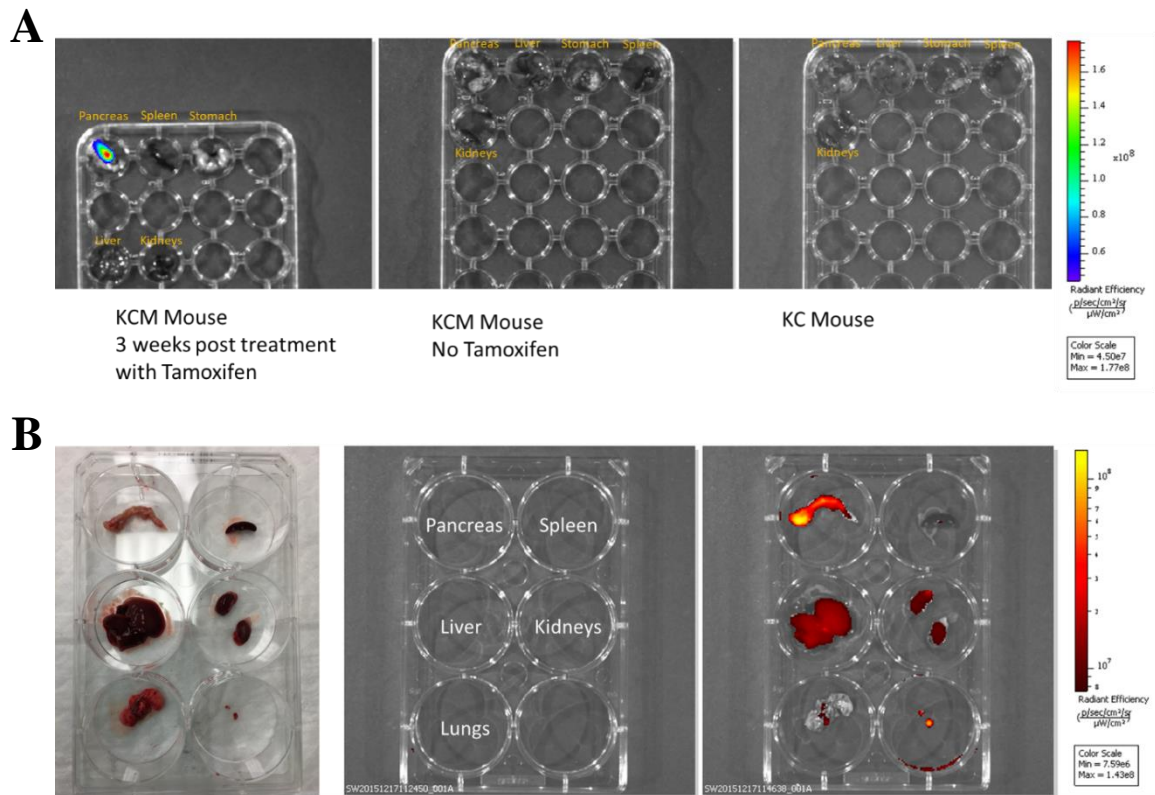


Figure 18. Fluorescent IVIS images of organs from KCM mice. Representative images are shown. (A) IVIS images with ICG filter pair of organs from KCM Spontaneous mouse 3 weeks post tamoxifen induction, KCM Spontaneous mouse w/o tamoxifen, and a KC mouse. (B) Organs from a KCM Spontaneous mouse 11 weeks post tamoxifen induction. Left – photograph of organs, Middle – Legend, Right – IVIS images with ICG filter pair. Intensity of the red-yellow fluorescence in ROI measurements indicate background and antibody accumulation for each organ.

CHAPTER 3: TARGETING PANCREATIC CANCER WITH ANTIBODY GUIDED PLGA NANOPARTICLES

3.1 Introduction

Pancreatic ductal adenocarcinoma (PDA) is a highly aggressive oncological disease with a 5-year relative survival rate of 7% [84] due to chemo-resistance. The resistance of PDA to chemotherapy or the inefficient delivery of chemotherapeutic drugs to the tumor site are likely due to the dense stroma and deficient vascular network in the pancreatic tissue microenvironment [8, 9]. Therefore, there is a pressing need to develop a novel drug delivery system for PDA that can increase the drug accumulation and uptake in a tumor specific manner [13].

Nanoparticles (NPs), modified to degrade in the tumor microenvironment or target tumor antigens, formulated from biodegradable and biocompatible polymers, such as PLGA, are being used increasingly in research due to their excellent systemic characteristics [85]. PLGA NPs allow for the encapsulation of a variety of hydrophobic chemotherapeutics or imaging agents, and can thereby facilitate the systemic delivery of these otherwise insoluble compounds with localization at the tumor site. This localization is the result of the enhanced permeability and retention effect (EPR). PLGA NPs with polyethylene glycol (PEG) displayed at the surface have been shown to increase circulatory half-lives of the NP platform, while surface modification with targeting agents have been shown to aid in localization of the NP selectively at targeted tissues [86-88]. Due to the positive results of nab-paclitaxel, paclitaxel (PTX) is one of the most widely used anticancer drugs approved for the treatment of many types of cancer. Targeted NP platforms consisting of PLGA encapsulated PTX will provide a drug delivery system that

would increase delivery of PTX to the tumor site since systemic administration of the untargeted drug loaded NP has many issues associated with it. For instance, if the NP is too large, issues can arise that prevent them from reaching the tumor site, as the NPs have to cross through several biological barriers, such as blood vessels, tissues, organs, and cells. Without any specificity for the tumor site, it may be necessary to use fairly high doses of NPs and drugs to achieve sufficient local concentrations. Targeting the NPs, and effectively the drug, could possibly overcome these problems.

This study was aimed at investigating the targeting ability of TAB004 conjugated PLGA NPs (T-NPs) *in vitro* and *in vivo*. PTX is one of the most common cytotoxic chemotherapies used, and therefore was selected for this study. I hypothesized that the conjugation of TAB004 to the surface of PLGA NPs will increase their accumulation and duration at the tumor site and thereby increase the overall therapeutic index of the treatment. For this purpose, PTX, indocyanine green (ICG), or fluorescein diacetate (FDA) was encapsulated in PEGylated PLGA NPs with and without TAB004 conjugation and its internalization, retention, and therapeutic efficacy evaluated in several MUC1-expressing PDA cell lines. The cytotoxic effect of the PTX loaded PLGA NPs was evaluated by 3-(4,5-dimethylthiazol-2-yl)-2,5-diphenyltetrazoliumbromide (MTT) assay. The accumulation and internalization of ICG or FDA loaded PLGA NPs was evaluated with confocal microscopy and *in vivo* imaging system (IVIS) Spectrum imaging.

3.2 Material and Methods

All chemical reagents use for the study were of analytical grade and above. Poly(DL-lactide-co-glycolide) M_w 20,000 (PLGA) (50:50) PolySciences, Inc. (Warrington, PA). Polyethylene glycol M_w 1000 (PEG₁₀₀₀), Poly(vinyl alcohol) MW 6000 (PVA) (80 mol% hydrolyzed), 1,1'-carbonyldiimidazole (CDI), 1,3-diaminopropane (DAP), Dextrose were purchased from Sigma Aldrich (St. Louis, MO). Paclitaxel was purchased from Matrix Scientific (Columbia, SC), ICG was purchased from Chem-Impex (Wood Dale, IL). TAB004 monoclonal antibody was obtained from OncoTAB, Inc. (Charlotte, NC, USA).

BxPC3, HPAC, HPAFII, and MIA PaCa-2 were purchased from ATCC (Manassas, VA). HPAC, HPAF II, and MIA PaCa-2 were maintained in Dulbecco's modified Eagle's medium (DMEM, 11965-092, Gibco). BxPC3 cell lines were maintained in RPMI medium 1640 (RPMI, 11875-093, Gibco). Growth media for these cell lines were supplemented with 10% fetal bovine serum (FBS, Gibco), 3.4mM ι -glutamine, 90 units (U) per ml penicillin, and 90 μ g/ml streptomycin (Cellgro).

For the PTX NP formulation a 20 mg sample of was dissolved into 600 μ l of DMSO-*d*₆ and the concentration of the respective cargo determined using ¹H NMR at 25 °C by comparing unique resonances of the cargo to the methylene residue of PLGA at 5.2 ppm. For the FDA, ICG, and NR NP formulations, a sample of nanomaterial (2-4 mg) was dissolved into DMSO and the amount of cargo quantified by UV-Vis.

$$\text{Encapsulation Efficiency} = \frac{\text{Amount of cargo encapsulated}}{\text{Amount of cargo used}} \times 100$$

Particle size, polydispersity index (PDI), along with zeta potential were determined by dynamic light scattering (Zetasizer Nano, Malvern Instruments).

Release profiles of NPs were modeled using FDA NPs. The release characteristics of these particles were characterized in phosphate buffered saline (PBS) at pH 7.4.

PCL_{14K}-PEG₁₀₀₀ was prepared according to the following procedure. Polycaprolactone (2 g, M_w ~ 14,000) was added to a 50 ml oven dried round-bottom flask fitted with a claisen adapter and equipped with a magnetic stir bar, a rubber septum, and a reflux condenser with attached drying tube. To this was added 20 ml of thionyl chloride via syringe, and the rubber septum replaced with a ground-glass stopper, and the resulting solution heated to reflux for 3 hrs. The thionyl chloride was then removed under reduced pressure using a rotary evaporator. The resulting residue was placed under a nitrogen atmosphere and 50 ml of freshly distilled THF was added by cannula followed by PEG₁₀₀₀-diol (2.9 g, 20 equivalent) and triethylamine (2ml, 14.35 mmol). The resulting solution was left to stir for 18 hrs at room temperature. This solution was then poured into 500 ml of DI water under vigorous stirring to precipitate the desired product and remove unreacted PEG₁₀₀₀ diol. The precipitate was isolated by filtration, re-dissolved into THF (50 ml), and precipitated as before. This process was repeated three times. Finally, the isolated product was dried under vacuum at 25 °C for 72 hrs. The desired product was isolated as a solid white material (1.13 g, 53 %). ¹H NMR (500 MHz CDCl₃): δ 1.36 (m, -CH₂CH₂CH₂-), 1.63 (m, -CH₂CH₂CH₂-), 2.28 (t, -C(O)CH₂-), 3.62 (s, -OCH₂CH₂-), 4.04 (t, -OCH₂).

PCL_{14K}-PEG₁₀₀₀-NH₂ was prepared by the according to the following procedure. PCL_{14K}-PEG₁₀₀₀ (1 g) was added to a 50 ml oven dried 2-neck round-bottom flask equipped with a magnet stir bar and a rubber septum with nitrogen inlet. To this was added 20 ml of dry methylene chloride (DCM) followed by 1,1'-carbonyldiimidazole (100 mg, .62 mmol) and the resulting solution left to stir for 6 hrs at room temperature. To this was added 1,3-diaminopropane (1 ml, 12.19 mmol) and the resulting solution left to stir for 12 hrs at room temperature. The DCM was then removed under reduced pressure using a rotary evaporator. The resulting viscous yellow liquid was dissolved into THF (20 ml) and precipitated by pouring the solution into 250 ml of vigorously stirred DI water. The precipitate was isolated by filtration, re-dissolved into THF (20 ml), and precipitated as before. This process was repeated three times. Finally, the isolated product was dried under vacuum at 25 °C for 72 hrs. The desired product was isolated as a yellow solid (.5 g, 50%). Although the resonances for the end-group -C(O)NHCH₂CH₂CH₂NH₂- are not assigned due to obfuscation of these resonances by the polymer backbone, the polymer tested positive for the presence of primary amines using the Kaiser test [89]. H NMR (500 MHz CDCl₃): δ 1.37 (m, -CH₂CH₂CH₂-), 1.64 (m, -CH₂CH₂CH₂-), 2.29 (t, -C(O)CH₂-), 3.63 (s, -OCH₂CH₂-), 4.05 (t, -OCH₂).

Nanoparticles (NPs) were prepared by the nanoprecipitation method. Briefly; 100 mg of PLGA (50:50, M_w ~ 20 K), 5 mg of PCL-PEG₁₀₀₀, 1 mg PCL-PEG₁₀₀₀-NH₂, and 1 - 5 mg of cargo was dissolved into 10 ml of acetone. This solution was then added dropwise via syringe into a stirred solution of 1% PVA (20 ml) at a rate of 90 ml/hr controlled using a syringe pump. The resulting colloidal suspension was then transferred to a 100 ml round-

bottom flask, and the acetone removed under reduced pressure using a rotary evaporator. NPs were then purified by centrifugation (25 min, $30,000 \times g$) using three successive washes of sterile filtered 18 Ω water at 4 °C. The resulting NP pellet was then resuspended into sterile filtered 18 Ω water (10 ml), whereupon dextrose (10 mg) was added as a lyoprotectant. This colloidal suspension was then flash frozen in liquid nitrogen then lyophilized at 25 °C and 50 mTorr for 24 - 48 hrs resulting in a flocculent solid. Paclitaxel (PTX), Fluorescein Diacetate (FDA), and Nile Red (NR) were all prepared according to the general method described above. See table 1 for the amount of cargo used in the preparation of the respective nanomaterials.

ICG NP's were prepared similar to the general method with minor modification. Briefly; 100 mg of PLGA (50:50, $M_w \sim 20$ K), 5 mg of PCL-PEG₁₀₀₀, 1 mg PCL-PEG₁₀₀₀-NH₂ was dissolved into 9 ml of acetone. Meanwhile 1 mg of ICG was dissolved into 1 ml of sterile filtered 18 Ω water. The two solutions were then mixed, and vortexed rapidly for 2 min. The resulting solution was then added dropwise via syringe into a stirred solution of 1% PVA (20 ml) at a rate of 90 ml/hr controlled using a syringe pump. The resulting colloidal suspension was then transferred to a 100 ml round-bottom flask, and the acetone removed under reduced pressure using a rotary evaporator. NPs were then purified by centrifugation (25 min, $30,000 \times g$) using three successive washes of sterile filtered 18 Ω water at 4 °C. The resulting NP pellet was then ii into sterile filtered 18 Ω water (10 ml), whereupon dextrose (10 mg) was added as a ii. This colloidal suspension was then flash frozen in liquid nitrogen, and lyophilized at 25 °C and 50 mTorr for 24 - 48 hr resulting in a flocculent green solid.

Table 2. Cargo Loading of PTX, FDA, NR, and ICG into Nanomaterials

Nanomaterial	Cargo (mg)	Loading	Amount Encapsulated (mg /100 mg NPs)	EE (%)
PTX NPs [*]	5		2	40
FDA NPs ^{**}	2		.11	5.5
NR NPs ^{**}	2		.28	14
ICG NPs ^{**}	1.75		.38	22

EE = Encapsulation Efficiency. ^{*} Determined by 1H NMR. ^{**} Determined by UV-Vis.

Table 3. Structural Properties of PTX, FDA, NR, and ICG Nanomaterials

Nanomaterial	HD (nm)	PDI	ZP (ζ)
PTX NPs	141.8	.169	-7.6 \pm .2
FDA NPs	171.3	.129	-6.4 \pm .2
NR NPs	209.3	.175	-6.7 \pm .1
ICG NPs	180.7	.076	-6.8 \pm .1

HD = Hydrodynamic Diameter, PDI = Polydispersity Index, ZP = Zeta Potential.

1 ml Solutions of FDA NPs (1 mg/ml) were incubated with constant stirring at 37 °C over 72 hrs. 100 μ l samples were taken at the indicated time-points and centrifuged (16,000 x g) to pellet out the remaining NPs. 50 μ l of NP free buffer was removed carefully so as not to disturb the pellet, and 20 μ l of 5% NaOH added to hydrolyze the liberated FDA. Absorbance measurements were recorded at 490 nm. These values were compared to a control sample having been dissolved in a 50:50 ACN: H₂O solution to liberate the entire sample of FDA from the NPs, and hydrolyzed as above.

SEM Imaging

Lyophilized nanoparticles were re-suspended in H₂O at 0.01 mg/mL concentrations and sonicated for 10 s. Samples were placed on SPI 5x5 silicon chips and dried overnight at 40 °C. Scanning electron microscopy (SEM) images were obtained with a Raith 150 microscope operated at 10 kV.

MUC1 WT was cloned into the pLNCX.1 vector consisting of the neomycin resistance gene for retroviral infection. GP2-293 cells were transfected with MUC1 WT and pVSV-G vectors and the resulting viral supernatant used to infect BxPC3 cells. Cells designated as BxPC3 MUC1 represents cells expressing full length MUC1 that consists of the extracellular domain, the transmembrane domain and wild type cytoplasmic tail domain. Cells designated as BxPC3 Neo represent cells that only express an empty vector control and therefore represents the endogenous levels of MUC1 in these cells. KCM cell line was generated by the Mukherjee lab from spontaneous PDA tumors from KCM mice. This cell line expresses both mouse Muc1 and human MUC1. Retroviral transduction of KCM cells with MSCV Luciferase PGK-Hygro (MSCV Luciferase PGK-hygro was a gift from Scott Lowe, Addgene plasmid # 18782) was performed by transfecting GP2-293 cells with the MSCV Luciferase PGK-Hygro and pVSV-G vectors and using the subsequent viral supernatant to infect KCM cells.

TAB004 conjugation to PLGA nanoparticles was performed using NuLink conjugation kit (NuChemie). PLGA nanoparticles were weighed out into an appropriate Eppendorf tube. To a vial containing 1 mg of the NuLink© bis-electrophile thioester was added 1 drop of DMSO to assist with dissolution, then 500µl of 18Ω H₂O was added. The solution was vortexed until all of the labeling reagent was dissolved. The PLGA

nanoparticles were re-suspended in 200 μ l of 18 Ω H₂O. The labeling solution was added dropwise to the nanoparticles while under a gentle vortex and allowed to incubate at room temperature (how long time) after mixing. The labeled nanoparticles were centrifuged at 21,000g and 4 °C to pellet them. The supernatant was removed and the labeled nanoparticles re-suspended in 200 μ l of 18 Ω H₂O. 30 μ g of TAB004 at mg/ml conc (in azide free buffer) was then added to the labeled NP solution in one portion. The next day, the nanoparticles were centrifuged at 21,000 rcf and 4 °C to pellet them and the supernatant discarded. Nanoparticles were re-suspended into desired working volume of PBS. Successful TAB004 conjugation to the PLGA nanoparticle was confirmed using FACS (BD Fortessa) and an anti-mouse IgG₁-FITC secondary antibody.

Cell viability assays were performed using MTT (3-(4,5-Dimethylthiazol-2-yl)-2,5-Diphenyltetrazolium Bromide) (Fisher Scientific, USA). Optimal number of cells per cell line were plated into 96-well tissue culture plates to ensure cells would not be over confluent after 48 hours post treatment. 24 hours after cells were plated, they were treated with corresponding concentrations of dimethyl sulfoxide (DMSO), PTX, blank PLGA nanoparticles, PTX loaded PLGA nanoparticles, and TAB004 conjugated PTX loaded PLGA nanoparticles for 1.5 hours. After 1.5 hours the treatments were washed off with 1x PBS and 200 μ l of fresh media was added to the wells and cell lines were incubated for 48 hours at 37°C, >90% humidity, and 5% CO₂ conditions. Following the 48 hour incubation, the media was replaced with 100 μ l of phenol red free media and 10 μ l of MTT was added to each well. Plates were incubated at 37°C, >90% humidity, and 5% CO₂ conditions for 4 hours, after which the media and MTT were removed, 100 μ l of DMSO added, and

incubated at 37°C for 10 minutes. The plates were then read using a ThermoFisher Scientific MultiScan GO.

Cell lines were plated into 4-chamber well slides (154917, LAB-TEK) at optimal concentration to ensure cells would not be over confluent after 24 hours. 24 hours after cells were plated, they were treated with fluorescein (20µg/ml) , or fluorescein diacetate and Nile Red containing PLGA nanoparticles at 1mg/ml concentration for 1.5 hours at 37°C, >90% humidity, and 5% CO₂ conditions. After treatment, cells were washed with PBS for 5 minutes (3x) and fixed with 4% formaldehyde. Prolong Gold Antifade reagent with DAPI (P36935, Molecular Probes) was applied to mount coverslips. Images were acquired on an Olympus Fluoview FV 1000 confocal microscope.

TAB004 conjugation to pHrodo Red was performed using the pHrodo Red, succinimidyl ester (pHrodo Red, SE) kit (P36600, Molecular Probes). TAB004 conjugation to indocyanine green (ICG) was performed using the ICG Labeling Kit –NH₂ (LK31-10, Dojindo Molecular Technologies, Inc.). All conjugations were performed using manufacturer protocols. Cell lines were plated into 4-chamber well slides (154917, LAB-TEK) at optimal concentration to ensure cells would not be over confluent after 24 hours. 24 hours after cells were plated, they were treated with 5µl of TAB004-phRodo Red conjugation solution for various time points at 37°C, >90% humidity, and 5% CO₂ conditions. During the last 5 minutes of treatment, Wheat Germ Agglutinin-Alexa Fluor 488 conjugate (W11261, Molecular Probes), was added to each chamber at 5µg/ml. The cells were washed with PBS for 5 minutes (3x) and fixed with 4% formaldehyde. Prolong Gold Antifade reagent with DAPI (P36935, Molecular Probes) was applied to mount

coverslips. Images were acquired on a GE Healthcare Life Sciences DeltaVision Elite Imaging microscope.

C57Bl/6 mice were purchased from Jackson Laboratory and housed at UNC Charlotte's vivarium.

C57/Bl6 female mice were injected in the pancreas with 5×10^5 KCM-Luc cells and allowed to recuperate for 7 days before any experiments were performed.

Orthotopic KCM-Luc tumor bearing C57/Bl6 mice were injected with 125 μ l of Redijet D-Luciferin (760504, Perkin Elmer) intraperitoneally and imaged 25 minutes later with a Perkin Elmer IVIS Spectrum. Orthotopic KCM-Luc tumor bearing C57/Bl6 mice were injected with 25 μ g of TAB004-ICG, 50mg/kg of NP w/ICG, or 50mg/kg of TAB004-NP w/ICG intraperitoneally and imaged at various time points with a Perkin Elmer IVIS Spectrum. Mice were euthanized at the end of imaging studies. All procedures were conducted in accordance to the Institutional Animal Care and Use Committee of UNC Charlotte.

3.3 Results

The Ogle group evaluated the size and release profile of PLGA NPs to determine an optimal size for use (Fig. 19A). As shown, PCL_{14K}-PEG_{1K} and PCL_{14K}-PEG_{1K}-NH₂ partitions into the aqueous environment during self-assembly of the nanoparticles, thereby generating a nanoparticle having a pegylated surface with a small percentage of nucleophilic amines available for chemical modification. During self-assembly the cargo is encapsulated in the hydrophobic core. The functionalization of the NP surface was

performed using the NuLink bis-electrophile (Fig. 19B). Fluorescein Diacetate (FDA) PLGA NPs were used as a model system to investigate the size and release profile of the NP platform described (Fig. 20A-B). In vitro cargo release of the NPs was evaluated in PBS at pH 7.4. FDA was steadily released over the course of 120 hours. The percent of FDA released at 24, 48, 72, and 96 hours was 24%, 37%, 50%, 59%, and 70% respectively (Fig. 20B).

I determined whether the PLGA NPs internalizes into a human PDA cell line. BxPC3 cells have minimal expression of endogenous MUC1. The Mukherjee group generated BxPC3.MUC1 cells that stably express full-length MUC1. As control, the Mukherjee group generated BxPC3.Neo that expresses the empty vector. BxPC3.MUC1 cells express high levels of MUC1 while BxPC3.Neo cells express minimal levels of MUC1 [90]. In the later experiments, this will enable us to assess the specificity of the TAB004 antibody in an otherwise genetically identical PDA cell line. BxPC3.MUC1 and BxPC3.Neo cell lines were treated for 1.5 hours with FDA and Nile Red loaded NPs. This matched the total treatment time of PDA cell lines in the cell viability assay. After 1.5 hours, FDA loaded PLGA NPs internalize through endocytosis and punctate green fluorescence, from the hydrolysis of FDA in the NPs, can be seen inside the cells, indicating internalization of the NPs (Fig. 21). As expected, the internalization was similar in both the high and low expressing BxPC3 cells. Overall, cellular uptake of PLGA NPs without TAB004 conjugation in PDA cell lines is expected [91].

Next, I determined if PTX loaded NPs were more efficacious than PTX by itself in a panel of human PDA cells. The cell lines were selected based on their drug resistance

and MUC1 levels [92]. I compared the cytotoxicity of PTX loaded NPs to PTX alone *in vitro* by MTT assay. The amount of PTX in the NPs is ~ 2% wt/wt. An effective dose-dependent cell death was observed with PTX alone in BxPC3.MUC1, BxPC3.Neo, and MiaPaCa2 cells. HPAF-II and HPAC cells were highly resistant to killing by PTX alone (Fig 22). However, when treated with PTX loaded NPs, all cell lines including the resistant HPAF-II and HPAC responded in a dose dependent manner (Fig. 22). I was able to reach the IC₅₀ for BxPC3 Neo, BxPC3 MUC1, and MIA PaCa-2 with both PTX-loaded NPs and PTX alone (Fig. 22A-C), but I were only able to do so in HPAF-II and HPAC with the PTX loaded NPs but not with PTX alone (Fig. 22D, E). All the tested cell lines saw a significant decrease in cell viability when treated with PTX loaded NPs when compared to PTX alone at the higher concentrations. This is interesting since release studies indicate that only 39% of the NPs cargo is released at 48 hours (the total runtime of the experiment), even though the amount of PTX in the NPs was identical to the amount of free PTX. It is possible that the treatment is benefiting from the slow release profile of the NPs [93, 94].

I determined the specificity and quantified the internalization of TAB004 antibody by fluorescent microscopy (Fig. 23). The presence and uptake of TAB004 was visualized by conjugating the antibody to pHrodo Red, which is non-fluorescent outside the cell, but fluoresces red during endocytosis (Fig. 23A). The green fluorescence is wheat germ agglutinin that stains the cell membrane. The fluorescent signal from TAB004 is significantly increased in BxPC3.MUC1 when compared to BxPC3.Neo cells at all time points (Fig. 23B). There is some internalization observed in BxPC3 Neo, which can be caused by the very low level of endogenous MUC1 that is present, or by non-specific

endocytosis as PDA cells have been shown to actively swallow their surroundings through macropinocytosis [95, 96].

The successful conjugation of TAB004 to the surface of the NPs (T-NPs) was determined by flow cytometry (Fig. 24). The linking reagent, a thioester, was tested and was successful in linking TAB004 to the NPs (Fig 24B). Flow cytometry data shows a shift in fluorescence when NPs are conjugated to TAB 004 and labeled with anti-mouse IgG1 FITC. Unconjugated NPs did not display any shift in fluorescence (Fig 24A). NPs without the linking reagent but incubated with TAB004, or anti-mouse IgG1 FITC, or both also served as controls and as expected did not show any shift in fluorescence signal. This suggests that the thioester linker was successful in conjugating TAB004 to the NPs.

To determine whether NP internalization could be affected by the presence of TAB004, BxPC3.MUC1 and BxPC3.Neo cells were treated with FDA loaded T-NPs over time (Fig. 25A, B). No significant increase in fluorescence between FDA loaded NPs and FDA loaded T-NPs was observed in BxPC3.Neo (Fig. 25C). However, a significant increase in fluorescence between FDA loaded NPs and FDA loaded T-NPs was observed at 60 and 90 minutes in BxPC3.MUC1 cells (Fig. 25D). The data indicates that linking TAB004 to the NPs was highly effective in longer term retention of the NPs within the cells compared to NPs alone and that this retention was antigen specific [91].

Thus, I next determined the cytotoxicity of PTX loaded T-NPs compared to PTX loaded NPs in the same cells (BxPC3.Neo and BxPC3.MUC1) as well as in a panel of other PDA cell lines with varying levels of MUC1 expression and sensitivity to PTX (Fig.26).

The comparison I am interested in was between treatment groups (NP and T-NPs) and not necessarily between cell lines, so a different paclitaxel treatment range was chosen for each cell line due to variation in sensitivity to the drug. There was a significant decrease in cell viability when BxPC3.Neo cells were treated with T-NPs at the lowest concentration, but all other concentrations either did not have any significant differences or the NPs caused more cytotoxicity than the T-NPs (Fig. 26A). This was expected based on the low MUC1 expression and the similar retention of the NPs versus T-NPs in the BxPC3.Neo cells (Fig. 25C). On the other hand, BxPC3 MUC1, MIA PaCA-2, and HPAC all saw significant decreases in cell viability with PTX loaded T-NP treatment at high and low concentrations of PTX when compared to PTX-loaded NPs (Fig. 26B, C, and E). Significant decreases in cell viability were also observed in HPAF-II, but only in 3 of the higher concentrations (Fig. 26D). Overall, the addition of TAB004 to the surface of the PTX-loaded NPs decreased cell viability when compared to NPs alone. Although the effect of T-NPs versus NPs is modest, it is highly significant for the very resistant cell lines such as HPAFII and HPAC. I speculate that *in vivo* the effect would be more pronounced. The fact that these cells are only treated for 1.5hrs and then all drugs washed out from the cell culture suggests that the modest efficacy of T-NPs versus NPs may likely be due to the limitations of the *in vitro* cell viability assay.

I demonstrated the specificity of TAB004 *in vitro*, but the same needed to be determined *in vivo*. C57BL/6 immune competent mice bearing murine syngeneic orthotopic pancreatic tumors (KCM cells) [97] were injected intraperitoneal with TAB004 conjugated with indocyanine green (ICG) and imaged 24 hours post injection. The KCM

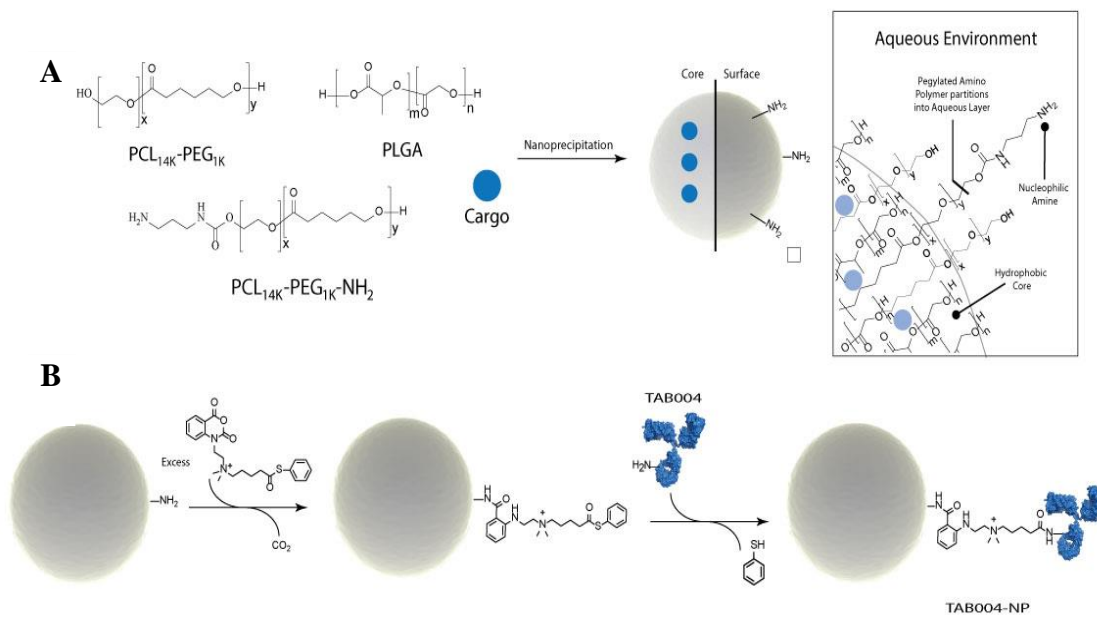
cells stably expressed the luciferase gene and thus bioluminescent tumors could be visualized by IVIS post luciferin injection. TAB004 localizes and persists specifically at the tumor site 24 hours later (Fig. 27). Images of 4 representative mice are shown. It is clear that the TAB004-ICG localizes only to the bioluminescent pancreatic tumors.

Next, I tested ICG loaded NPs and ICG loaded TAB004-conjugated NPs in mice bearing the same KCM bioluminescent orthotopic tumors to determine if TAB004 can increase the accumulation of NPs at the tumor site (Fig. 28). ICG loaded NPs appear to clear from the mouse between 24 and 48 hours post injection (Fig. 28A), similar to the biodistribution profile of ICG loaded NPs injected in non-tumor bearing mice (data not shown). However, ICG loaded TAB004-conjugated NPs (T-NPs) displayed significantly greater accumulation and persistence at the tumor site 24 and 48 hours post injection (Fig. 28B). *Ex vivo* images of the tumor and liver of the mice were taken 48 hours post injection. It is clear that the ICG loaded T-NPs accumulate and persist in the tumor while ICG load NPs cannot be detected in the tumor at 48hours. However, the fluorescence in the liver was identical for ICG-T-NPs and ICG-NPs (Fig. 28C) suggesting that the tumor localization is superior for TAB004-conjugated NPs. Thus, TAB004 conjugated NPs may be developed as a potential platform for targeted delivery of not only PTX, but other drugs and imaging agents directly to the pancreatic tumor while reducing toxicity to other major organs. Future studies will evaluate the in vivo anti-tumor efficacy in several models of PDA.

3.4 Conclusions

In this study, I aimed to investigate PEG-functionalized PLGA NPs conjugated to monoclonal antibody TAB004. TAB004 was shown to be specific for hypoglycosylated MUC1, whose overexpression is found in over 80% of PDA [98]. TAB004 conjugated PLGA NPs (T-NPs) showed stronger cellular accumulation over time than non-conjugated NPs in BxPC3.MUC1 cells. PTX-loaded T-NPs showed modest but significantly enhanced cytotoxicity at several doses (Fig. 26). I also observed prolonged and enhanced T-NP accumulation at the tumor site as compared to NPs alone (Fig. 28C) clearly demonstrating the potential utility of TAB004-functionalized nanoparticles for a therapeutic application in the treatment of PDA tumors. The results will be further discussed in the dissertation summary (Chapter 4).

3.5 Figures



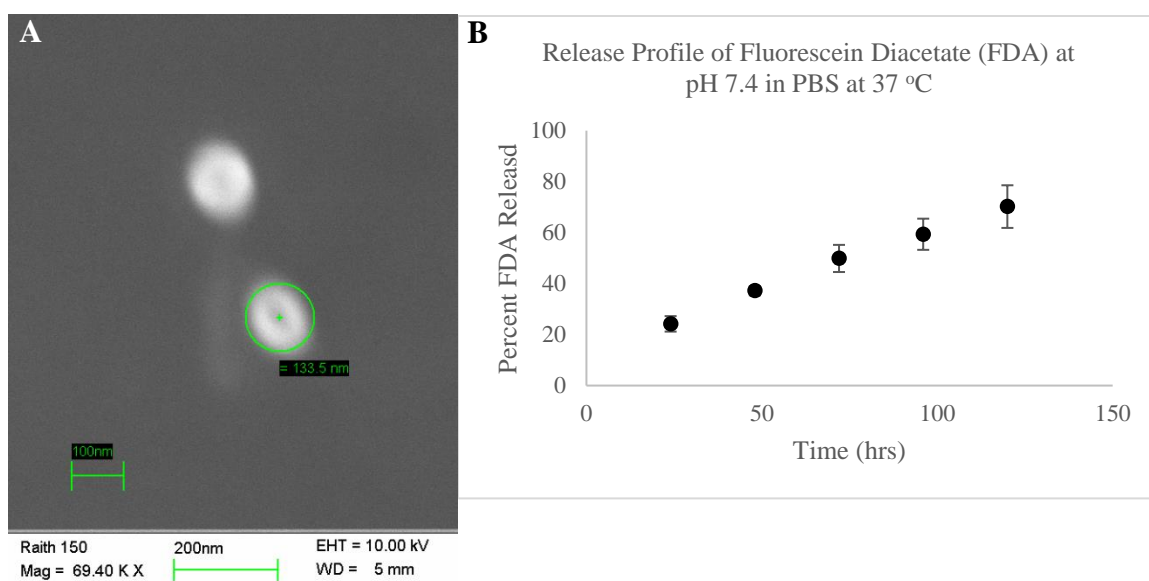


Figure 20. Characterization of PLGA NPs. Fluorescein Diacetate (FDA) PLGA NPs were used as a model system to investigate the size and release profile of the NP platform described (Fig. 2A-B). In vitro cargo release of the NPs was evaluated in PBS at pH 7.4. FDA was steadily released over the course of 120 hours. The percent of FDA released at 24, 48, 72, and 96 hours was 24%, 37%, 50%, 59%, and 70% respectively (Fig. 2B).

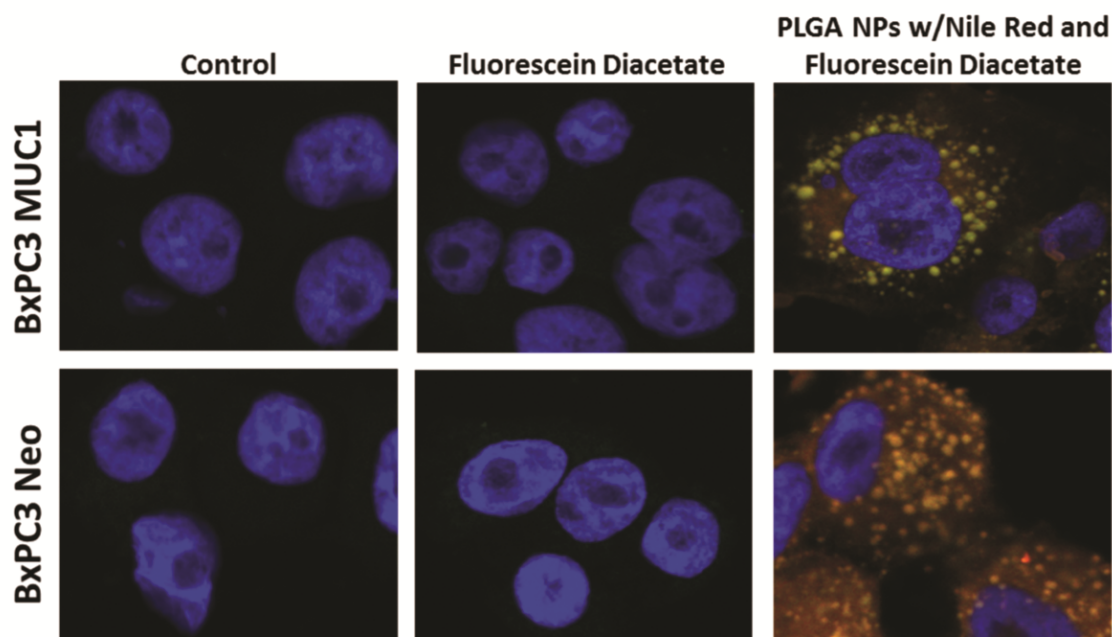


Figure 21. Internalization of PLGA NPs in: (A) BxPC3 MUC1; (B) BxPC3 Neo. Results shown are representative images (n=3)

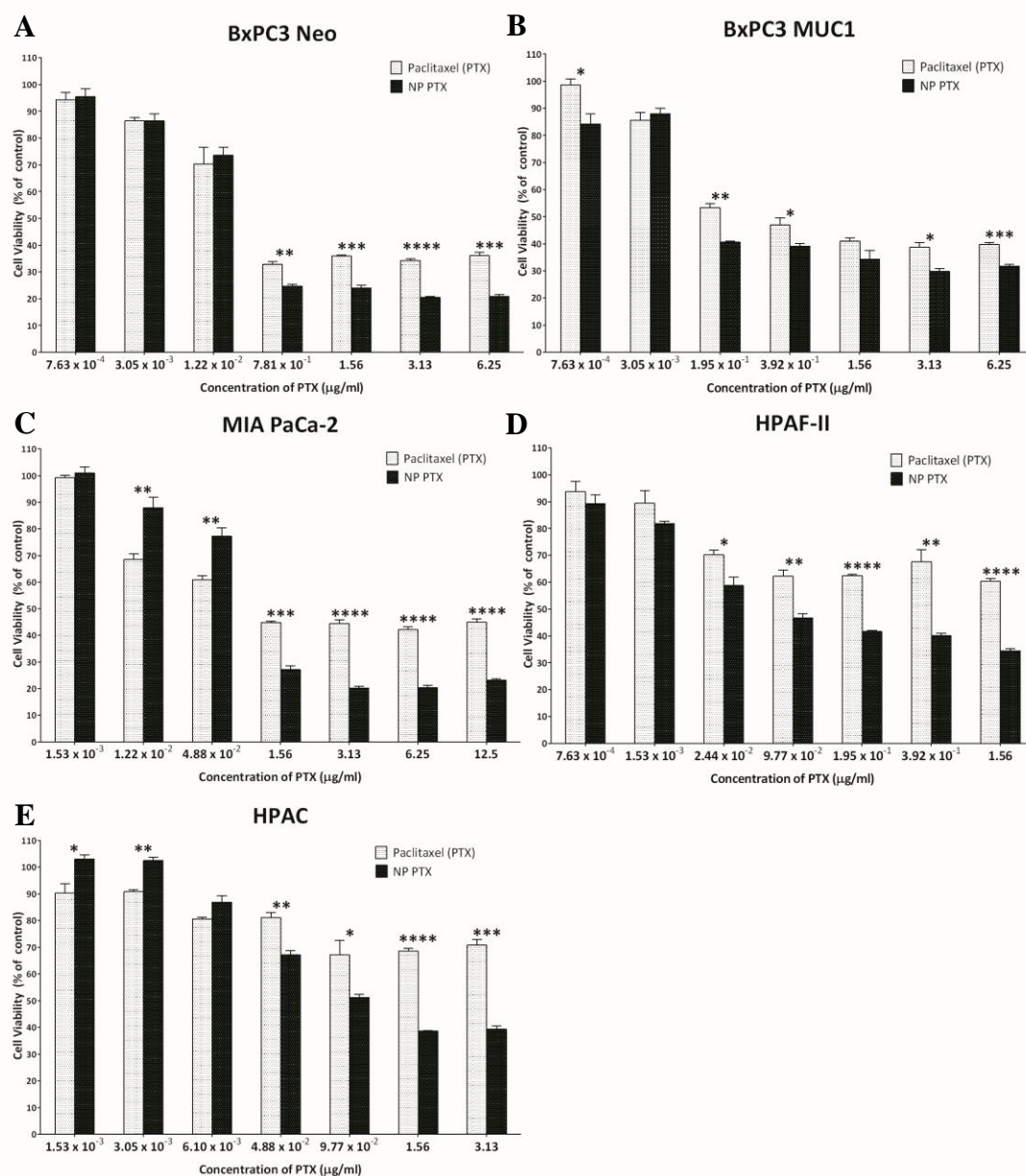


Figure 22. Cell viability of PDA cell lines treated with PTX and PTX loaded NPs: (A) BxPC3 Neo; (B) BxPC3 MUC1; (C) MIA PaCa-2; (D) HPAF-II; (E) HPAC. Data shown is mean \pm SEM (n=3) and determined by a one-sided t-test comparing treatment groups at each concentration, * $p < 0.05$, ** $p < 0.01$, *** $p < 0.001$, **** $p < 0.0001$.

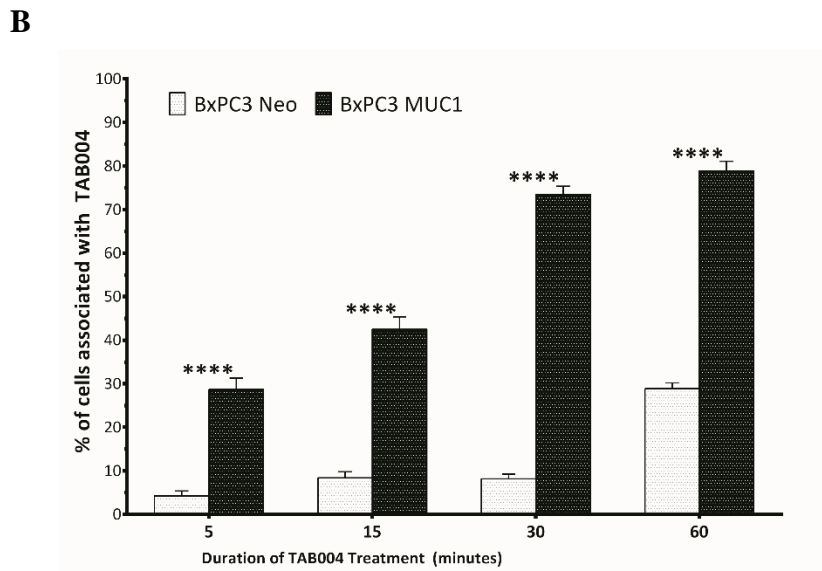
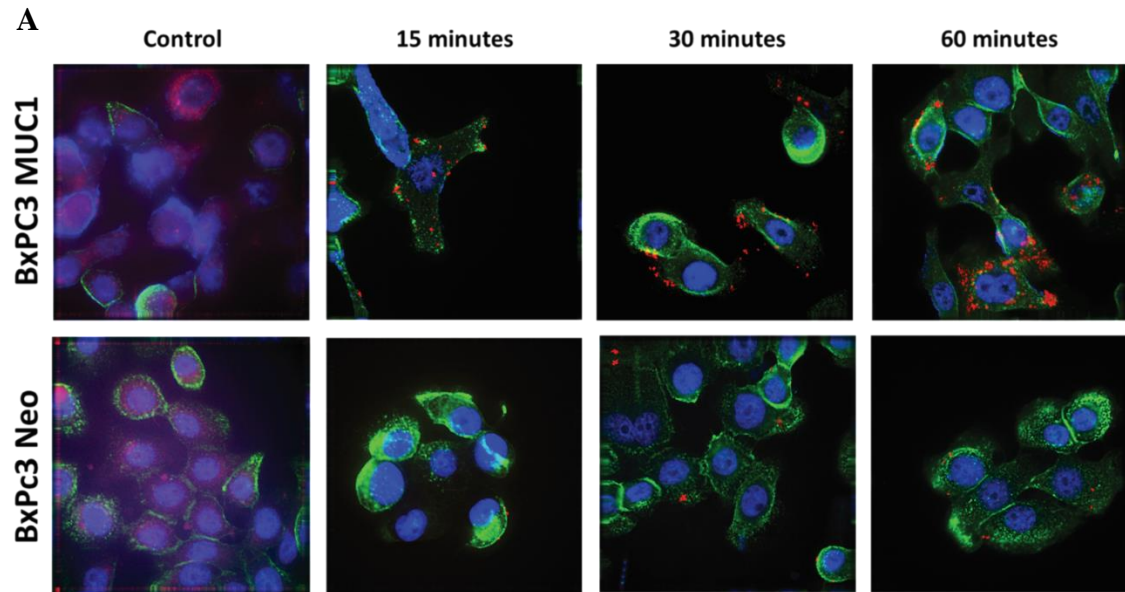


Figure 23. Specificity and internalization of TAB004 in BxPC3 MUC1 and Neo: (A) representative images cells treated with TAB004 conjugated to pHRedo red (n=3); (B) quantification of images determine by the number of cells associated with TAB004 divided by total number of cells. Data shown is mean \pm SEM (n=3) and determine by two-way ANOVA and Bonferroni's post-hoc test, *p<0.05, **p<0.01, ***p<0.001, ****p<0.0001.

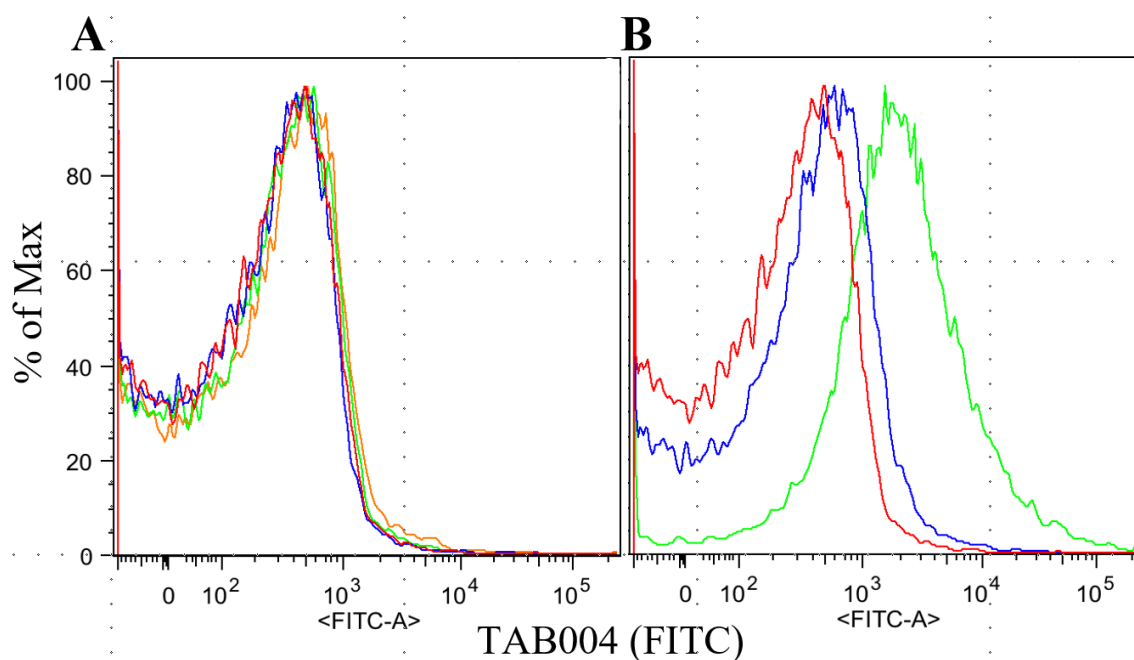


Figure 24. Confirmation of TAB004 conjugation to PLGA NPs with FACS. Blank NPs were treated with: (A) control (red), TAB004 (blue), anti-mouse IgG₁ FITC (green), and both TAB004 and anti-mouse IgG₁ FITC (orange/yellow); (B) control (red), NHS Ester linking reagent (blue), and NHS Ester linking reagent, TAB004, and anti-mouse IgG₁ FITC (green).

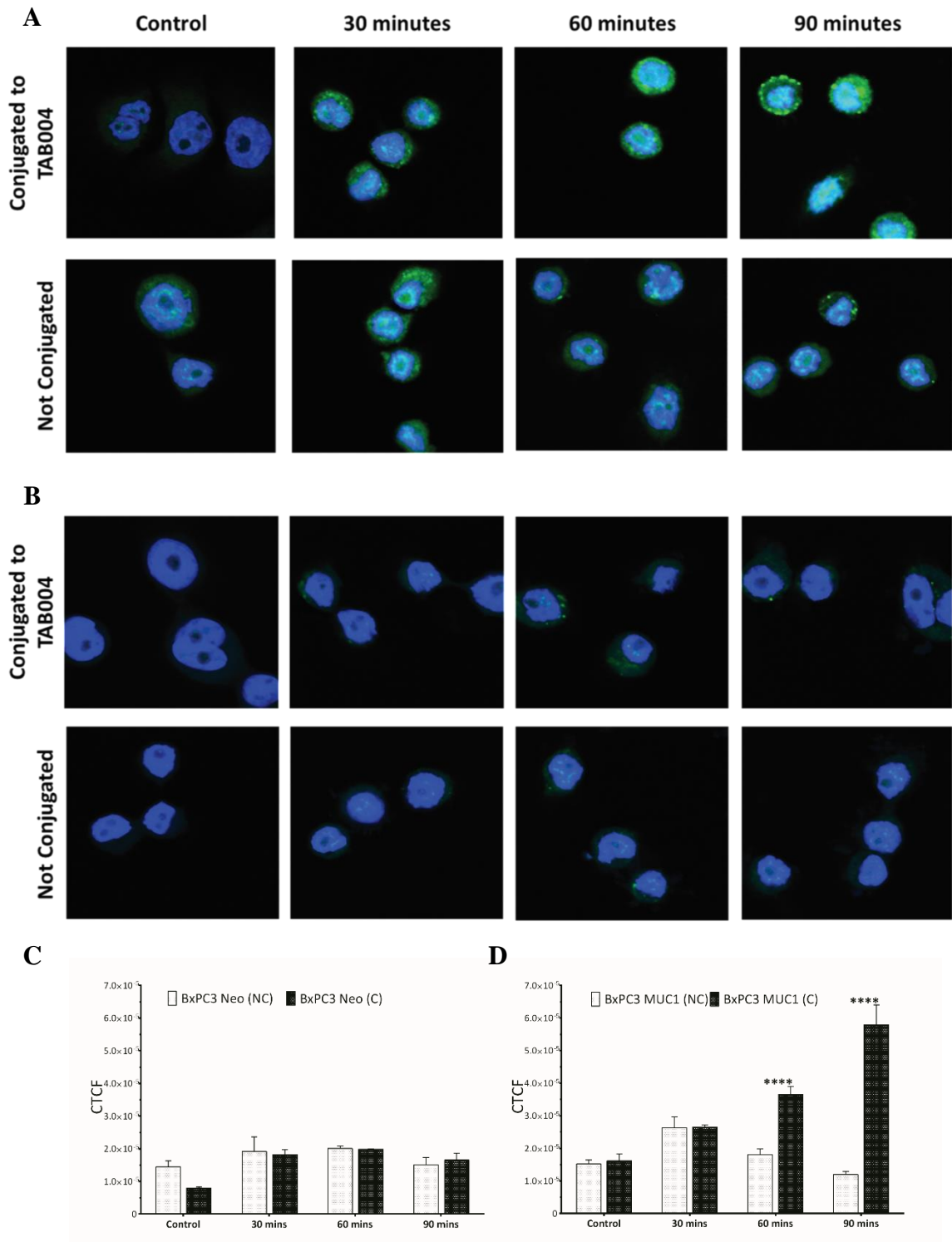


Figure 25. Internalization of TAB004 conjugated NPs loaded with fluorescein diacetate (FDA): (A) representative images of BxPC3 MUC 1 (n=3) treated with T-NPs; (B) representative images of BxPC3 Neo (n=3) treated with T-NPs; (C) and (D) quantification of fluorescence using Image J to determine corrected total cell fluorescence (CTCF). Data shown is mean \pm SEM (n=3) and determined by a one-sided t-test, * $p < 0.05$, ** $p < 0.01$, *** $p < 0.001$, **** $p < 0.0001$.

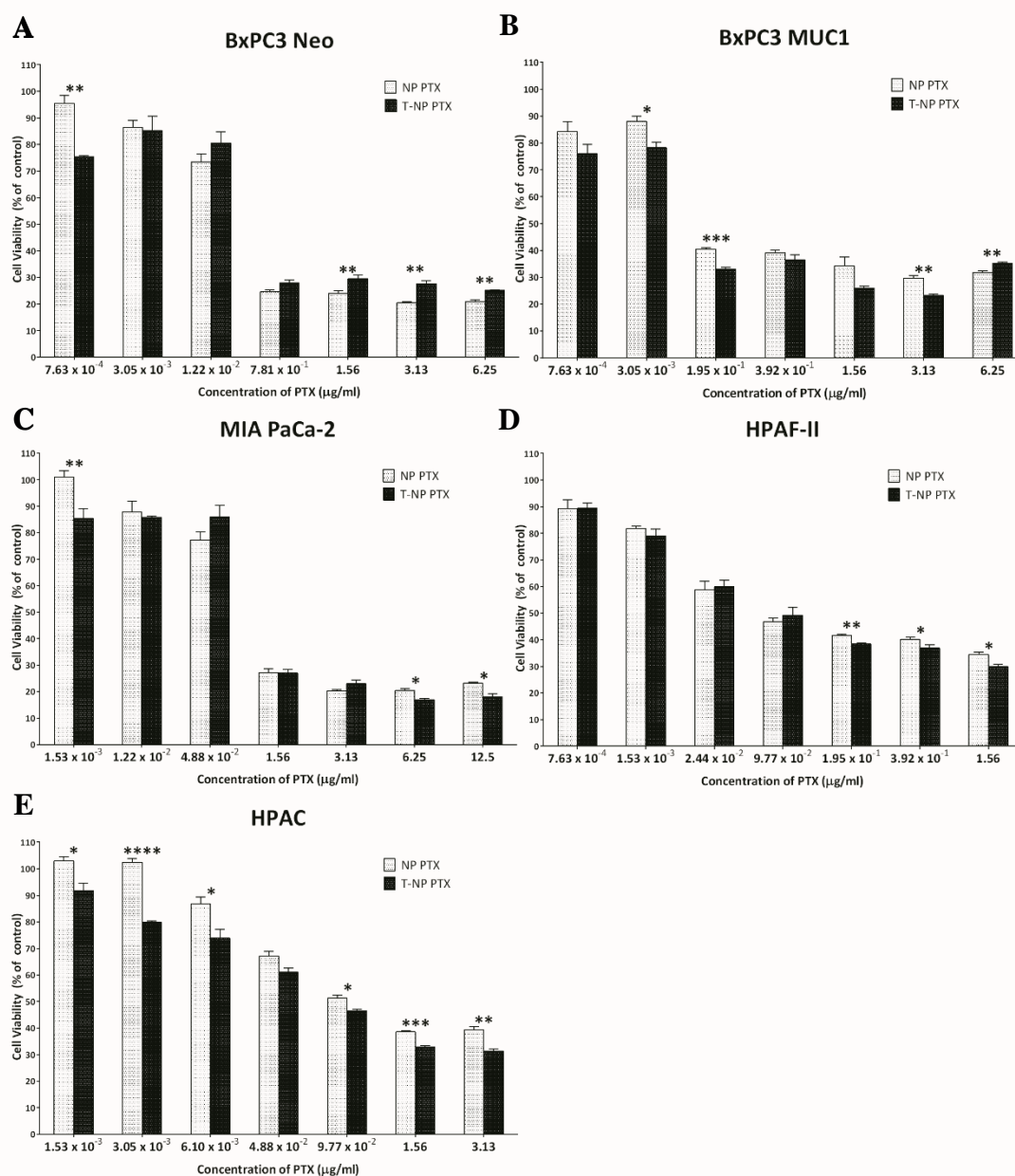


Figure 26. Cell viability of PDA cell lines treated with PTX loaded NPs and PTX loaded TAB004 conjugated NPs: (A) BxPC3 Neo; (B) BxPC3 MUC1; (C) MIA PaCa-2; (D) HPAF-II; (E) HPAC. Data shown is mean \pm SEM (n=3) and determine by a one-sided t-test comparing treatment groups at each concentration, * p <0.05, ** p <0.01, * p <0.001, **** p <0.0001.**

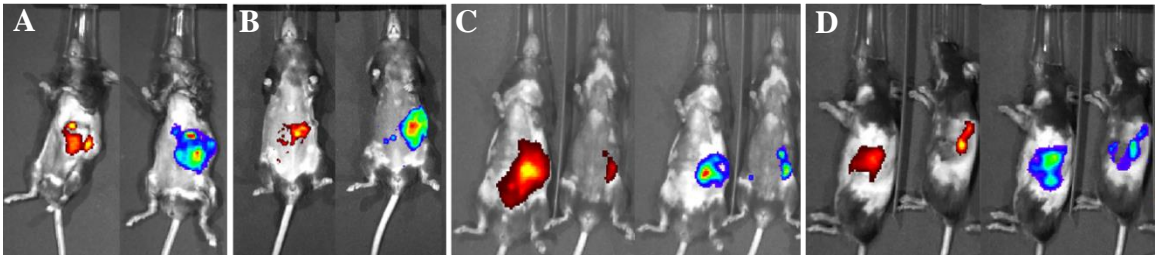


Figure 27. *In vivo* imaging of TAB004-ICG in orthotopically injected bioluminescent tumor bearing mice (ICG - red/yellow, tumor (luciferase-expressing) – rainbow, n=4): (A) mouse 1; (B) mouse 2; (C) mouse 3 and 4 ventral view; (D) mouse 3 and 4 side view.

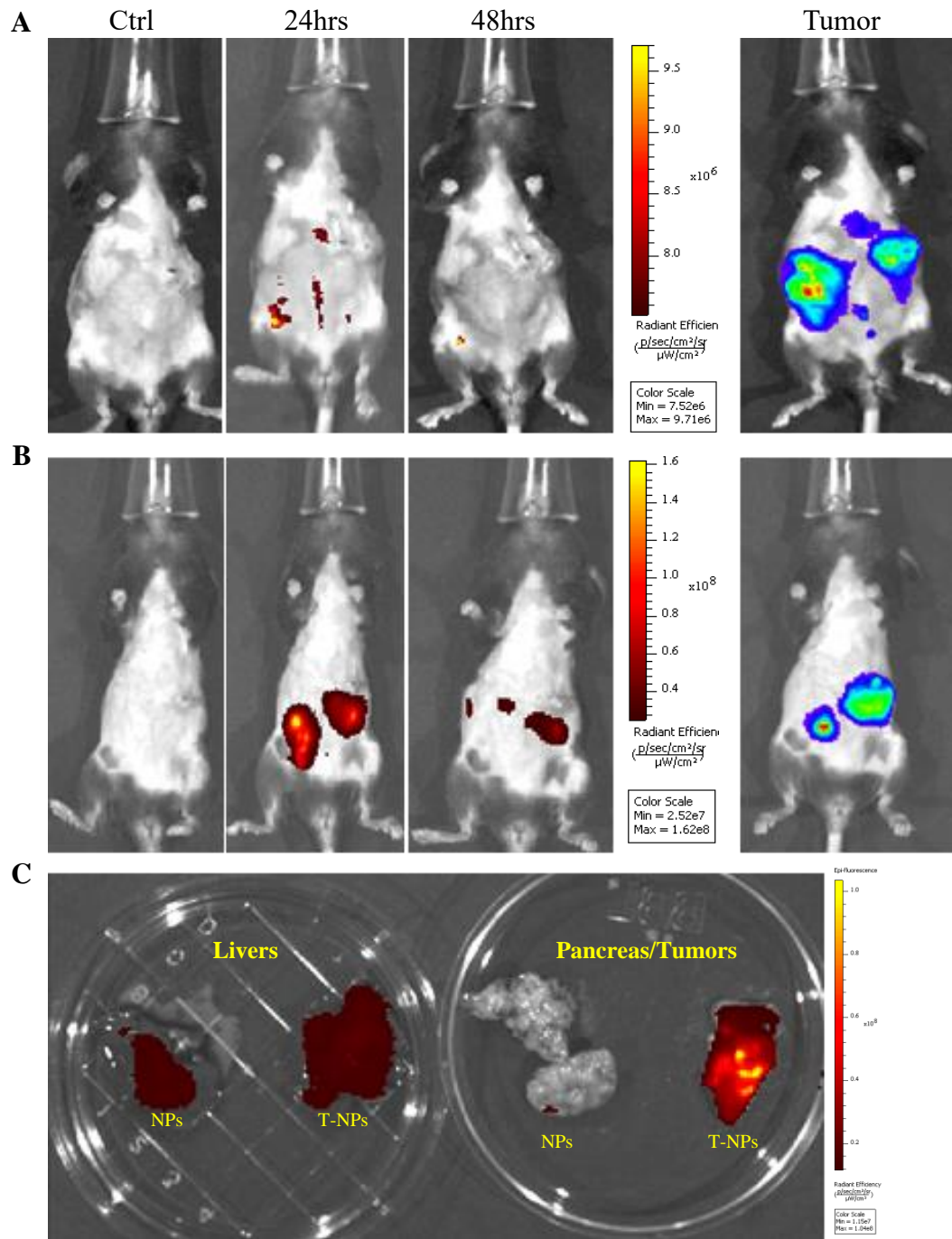


Figure 28. *In vivo* imaging of ICG loaded NPs and ICG loaded T-NPs orthotopically injected bioluminescent tumor bearing mice (ICG - red/yellow, tumor – rainbow, n=3): (A) ICG loaded NPs injected into tumor bearing mouse; (B) ICG loaded T-NPs injected into tumor bearing mouse; (C) *ex vivo* imaging of liver and tumor from (A) and (B).

CHAPTER 4: DISSERTATION SUMMARY

In chapter 2, I investigated the ability of TAB004 to specifically detect tMUC1 on PDA tumors and early PanIN lesions. This study demonstrated the ability of TAB004 to detect tMUC1 in orthotopic and spontaneous PDA tumor models for the first time. Previous studies showing TAB004 specificity to tMUC1 were performed *ex vivo* or in breast cancer models [74, 75, 99].

The concept of molecularly targeted diagnostic approaches would be very valuable toward the goal of precision medicine. The ability to monitor preneoplastic lesions and progression on a molecular level not defined by the presence of a palpable tumor mass and before any overt physiologic symptoms have developed would permit early and more adequate therapeutic intervention. tMUC1 is overexpressed in over 80% of pancreatic cancer patients [100, 101] and is also expressed in pancreatic intraepithelial neoplasia (PanIN) lesions, precursors of PDA [71].

Our results from the orthotopic tumor model demonstrate that TAB004 is highly specific in targeting the PDA tumor and does not accumulate in other organs. In control group 1 (normal C57/B16 mice) and 2 (KCM-Luc tumor bearing mice – no TAB004 injected), I established background fluorescence levels for the mice and used these values to determine antibody accumulation at the tumor site and other organs. Control groups 3 (non-tumor bearing mice injected with isotype IgG1-ICG) and 4 (KCM-Luc tumor bearing mice injected with isotype IgG1-ICG) displayed no significant increase in fluorescence levels in all regions when compared to control groups 1 and 2, suggesting that from an imaging standpoint, non-targeting antibody at the chosen concentration clears from the

mice in 24 hours. The significant increase in RE within the pancreas/tumor in mTAB004 and cTAB004 injected groups clearly demonstrates the retention of the targeting antibody. The livers from TAB004 injected groups displayed significant increase in RE over the control groups as well, with mTAB004 showing a greater increase over cTAB004. This appears to be a specific effect, possibly due to the presence of hepatic metastases from pancreatic cancer [102]. It also appears that TAB004 accumulates in the small intestine and spleen of mice, due to the increase in RE (Fig 7). Due to the orthotopic nature of the tumor, I have evidenced outgrowth of the primary pancreatic tumor into the surrounding organs including the spleen and small intestine due to their proximity to the pancreas. Whether this outgrowth is due to true metastasis or dissemination of tumor cells while injection is not clear at this time. Cells from the initial injection may leak out and cause many secondary tumors in the intraperitoneal space. Furthermore, I confirm that TAB004-ICG accumulates in the margins and within the pancreatic tumor bed. Other studies have attempted to target tMUC1 for diagnostic, imaging, and targeted therapy [75, 103-105]. However, due to the non-specificity of most of the MUC1 antibodies, I believe that TAB004 can improve the specific visualization of pancreatic tumor. Furthermore, fluorescent-tagged antibody may be useful in defining the tumor margins improving patient outcome that are eligible for resection [106].

Finally, I utilized a genetically engineered mouse model that spontaneously induced human tMUC1-positive pancreatic cancer (in KCM mouse) (Fig 9-11). The data from the KCM mice show that TAB004 can target tMUC1 being expressed in the pancreas before PDA develops. Examination of the pancreas from KCM mice show no evidence of a primary tumor, but IHC sections from these mice show the presence of PanIN 2 lesions. PanIN 2

lesions are the first stage in the development of PDA that is associated with significant genetic and molecular changes [107]. This early detection of the PanIN lesions can be translated into early detection of PDA and significantly improve disease outcome [12, 108]. As tMUC1 expression has global relevance in adenocarcinomas including pancreatic cancer, this study focused on applying our imaging approach to pancreatic cancer. Specifically, I illustrate the detection of the changes in the expression profile of the molecular biomarker tMUC1 with a noninvasive imaging approach. By focusing on early disease, i.e., the PanIN lesion, I explore a scenario in which the molecular changes in tMUC1 precede changes in anatomical and physiologic signs of tumor development. This study extends our prior work in breast cancer, which demonstrated that changes in MUC1 antigen that occur in breast cancer development could be detected in vivo using TAB004 as a carrier for imaging agent [75, 109]. By broadening the application of this methodology to pancreatic cancer, I move closer to establishing the value of tMUC1 as a wide-ranging cancer biomarker.

Progress has already been made in the direction of targeted cancer diagnostics. With regard to noninvasive imaging, the development of dynamic MRI techniques, magnetic resonance spectroscopy and positron emission tomography have contributed to progress. Still, none of these technologies probes for specific molecular biomarkers expressed by cells in proportion to their potential for malignancy. Consequently, this highly specific molecular imaging approach has the potential for capturing the earliest signs of neoplastic transformation and in the future permit predictive diagnosis and response to therapy. Fortunately, the incidence of PDA in the general population is too small to necessitate mandatory pancreatic cancer screening, but this in turn causes high costs, and the low

predictive sensitivities of current imaging discourage its use. Another application of this technology would be to monitor response to therapy and predicting recurrence.

Several risk factors are taken into consideration for recommending pancreatic cancer screening: certain environmental insults, hereditary pancreatitis, familial atypical mole and multiple melanoma syndrome (FAMMM), Peutz-Jeghers syndrome, polyposis syndrome, and BRCA mutations are some examples. This discussion will briefly highlight some environmental risk factors and genetic dispositions to PDA.

Currently, no strong environmental factors have been identified that substantially increase the risk of pancreatic cancer. Tobacco use appears to increase the risk by a factor of 2, and there is significant positive trend of increasing risk with increased duration and exposure [110]. Smokers who cease use for more than 10 years see about a 30% decrease in risk compared to active users [110]. Second-hand smoke, which contains or causes the release of several known carcinogens, has been associated with increased risk as well [111]. Aside from tobacco, other occupational exposures can increase risk of pancreatic cancer as well. An increase in risk by a factor of 1.4 to 4.4 has been seen in association with exposure to chlorinated hydrocarbon solvents, nickel compounds, chromium compounds, polycyclic aromatic hydrocarbons, organochlorine insecticides, silica dust, and aliphatic hydrocarbon solvents [112]. They all likely cause a combination of DNA damage and inflammation. An increase in risk of PDA has been seen with increased obesity. A mild elevated risk in individuals with a BMI of 30 kg/m^2 or higher was observed compared to those with a BMI $<23 \text{ kg/m}^2$ [113]. Diabetes has been examined as both a risk factor and early manifestation of pancreatic cancer. Diabetics are twice more likely to develop PDA than non-diabetics, and are often diagnosed with diabetes 2-3 years prior to PDA diagnosis [114, 115].

Additionally, data has shown that 57% of patients with diabetes less than 2 years and undergo a Whipple procedure see resolution of their diabetes [116]. In fact, 4% of people with new onset diabetes will develop pancreatic cancer. Pancreatic Cancer Action Network and NIH are soliciting research to develop screening modalities for this high-risk population [117].

Genetic predisposition to PDA elevates risk of PDA substantially. An individual with two first-degree relatives with pancreatic cancer would see a 6.4 fold increase in risk of PDA [118, 119]. This risk increases to >32 fold if three or more first-degree relatives have had PDA [120]. An example of a genetic mutation associated with PDA is the BRCA gene mutations. BRCA's play a role in double-stranded break repairs in DNA. When BRCA is mutated or altered, DNA repair is affected and the accumulation of DNA damage can occur, which can cause different effects that lead to the formation of cancer [121]. BRCA2 mutation carriers have an increased risk factor of 3.51 to 5.9 of developing PDA, while BRCA1 carriers show a smaller increased risk factor of 2.26 to 2.8 [122, 123]. PALB2 and ATM mutations also play a role in DNA repair. Mutations in the ATM gene increased the risk factor for PDA by 2.7 fold [124], and mutations in PALB have been associated with increased risk for pancreatic cancer, the exact risk value is still unknown [125]. Combining our imaging screening with individuals at higher risk of developing pancreatic cancer could possibly increase the survival rate.

In chapter 3 I investigated the use of TAB004 as a guide antibody for targeted therapy with PTX loaded PLGA nanoparticles. The novel platform of TAB004-PLGA NP loaded with PTX to target PDA had never been done before. Other studies have targeted tMUC1 with PTX loaded PLGA NPs, but in breast cancer cell lines [126]. The ability to target PTX-loaded nanoparticles to the tumor site would greatly enhance efficacy of PTX based treatments. Poly (lactic-co-glycolic acid) (PLGA) is one of the most effective biodegradable polymers used to construct polymeric nanoparticles (NPs). It is approved by the US FDA for use in drug delivery systems due to controlled and sustained- release properties, low toxicity, and biocompatibility with tissue and cells [127-129]. Poly(ethylene glycol) (PEG)-functionalized PLGA NPs are especially desirable as pegylated-NP platforms have demonstrated significantly reduced systemic clearance compared with similar particles without PEG. This design parameter is especially important for the passive targeting of nanocarrier to tumor by the enhanced permeability and retention (EPR) effects [130]. TAB004 conjugated PLGA NPs (T-NPs) showed stronger cellular accumulation over time than non-conjugated NPs in BxPC3.MUC1 cells. This enhancement of cellular internalization and accumulation may be due to the presence of TAB004 on the surface of the nanoparticle binding to hypoglycosylated MUC1, which has been shown to internalize through macropinocytosis [131]. Furthermore, PTX-loaded T-NPs showed modest but significantly enhanced cytotoxicity at several doses. The modest enhancement of cytotoxicity may be attributed to the limited time (1.5 hours) of exposure of cells to the drug. Longer incubation with the nanoparticles caused degradation of the PLGA NPs which then interfered with OD values in the MTT assay. It is well established that the antitumor effect of PTX results from its intracellular accumulation over time [132].

Nevertheless, *in vivo*, I observed prolonged and enhanced T-NP accumulation at the tumor site as compared to NPs alone clearly demonstrating the potential utility of TAB004-functionalized nanoparticles for a therapeutic application in the treatment of PDA tumors. Thus, I believe that the modest cytotoxic advantage observed *in vitro* would be significantly enhanced *in vivo*. A treatment study in mice was performed, but no relevant data could be obtained. 18 C57/Bl6 mice were orthotopically injected in the pancreas with 5×10^5 KCM-Luc cells and split into 3 groups: Control, PTX-loaded NPs, and PTX-loaded T-NPs. The mice are allowed to recover for at least 7 days after orthotopic surgery before treatment can begin. Near the start of treatment, mice from all 3 groups were dying at an alarming rate from the aggressive cancer, so it seems injecting 5×10^5 cells in these mice led to a highly aggressive tumor. By the 2nd week of treatment, over 75% of the mice had died. Additionally, the dosage of PTX in the PLGA NPs actually given to the mice was about 17 fold lower than the proposed dose. The minimum dose proposed was 250 mg/kg of PTX-loaded NPs (and T-NPs), which translates to 100 μ g of PTX per mouse (20g) per injection (PTX is 2% of NP weight). But limitations in the preparation of the PLGA NPs only allowed for a colloidal suspension of 3mg/ml, meaning only 0.3mg of PTX-loaded NPs could be used per injection (100 μ l limit). This translated to only 6 μ g of PTX given to each mouse per injection. I hypothesize that the combination of injecting too many KCM-Luc cells and lower than the minimum effective dose (from literature) condemned the experiment to fail. I was not discouraged however, and learning from these mistakes, a titration was performed to find an appropriate number of KCM-Luc cells to inject during orthotopic surgery and a range of 20,000 to 50,000 cells produced even growing tumor that could still be imaged with IVIS 1 week after surgery. Future studies will benefit from this

data. As for the limitations of the PLGA NPs, it is possible to alter the formulation and methods in generating them to encapsulate a higher percentage of PTX. The *in vivo* imaging data of ICG loaded T-NPs is very promising, and perhaps with a higher PTX payload, the TAB004-PLGA NP platform will be successful.

Nevertheless, I should not limit myself to only examining PLGA NPs and/or PTX for targeted therapy with TAB004. Several types of NPs have been used for therapeutics over the years [133].

Liposomes are composed of self-assembled phospholipids into bilayers with a spherical shape and range in size from 30nm to microns [134]. Liposomes can encapsulate both the hydrophilic and hydrophobic chemotherapies within the vesicles and lipid bilayer. These nanoparticles are highly biocompatible and can be modified for different applications, such as increasing circulation time and active targeting [135]. There are currently multiple liposome-based anti-cancer therapeutic compounds available in the market for clinical use, such as Caelyx, DaunoXome, DepoCyt, Doxil, Myocet, and VincaXome [136]. Use of these platforms with conjugated TAB004 will be highly desirable in the future.

Solid Lipid NPs (SLNs) are non-toxic nanoparticles produced from natural lipids or synthetic lipids [137]. An advantage of SLNs is that their production does not need to use toxic organic solvents, which helps keep the drug composition intact. SLNs can carry both the lipophilic or hydrophilic drugs. SLNs are versatile nanoparticles since they

demonstrate controlled release and protection of payload, which is beneficial in intravenous administration [138].

Nanostructured lipid carriers (NLC), are composed of a mixture of solid and liquid lipids [139]. These nanoparticles are internalized by tumor cells and have several advantages, including high drug loading potential, controlled drug release, increased drug stability, and the ease of large-scale generation [140].

Gold NP surfaces can be easily modified by amine and thiol groups for tumor specific targeting. Gold NPs also show surface plasmon resonance (SPR) [141]. SPR is a non-radiative electromagnetic surface wave that propagates in a direction parallel to the negative permittivity/dielectric material interface. Their small size allow them to accumulate and internalize into tumor cells through EPR effect. Gold NPs-based therapeutics are also being tested in early-phase clinical trials with some positive results. Gold NPs can also be used as imaging vectors and in tumor-selective photothermal therapy due to the high atomic number of gold [142].

Dendrimers consist of highly branched repeat polymeric star-like molecules with a 3D geometric shape. They have three different parts including a central core, the branches, and an exterior surface with various surface functional groups [143]. Tertiary amines present in the structure of dendrimers allow for the addition of different molecules for active targeting [144]. They are used for both the diagnostic and therapeutic purposes [145]. Vivagel is the first dendrimer-based drug to be on the Fast Track approval approach with the Food and Drug Administration [146].

Iron oxide NPs are inorganic NPs with size of 1–100 nm in diameter. Since these particles can be visualized by magnetic resonance imaging (MRI), they have been used for imaging purposes in various tumors [147]. They can be used to destroy cancer cells by hyperthermia through their conduction by external magnetic field at the tumor site [148]. These NPs can also be used for *in vivo* applications because they degrade into iron which can be absorbed by hemoglobin in the body [149].

Combining TAB004 with any of the nanoparticles described could prove beneficial for targeted therapy. Although this dissertation only examined the use of paclitaxel loaded nanoparticles, other therapies such as 5FU, FOLFIRINOX, Gemcitabine, colchicine [150], or any combination of therapies could be used with our targeting platform in the future to fight pancreatic cancer.

SUPPLEMENTAL

Characterizing TAB004

Monoclonal antibody based therapies (MAT) for cancer have improved significantly over the past twenty years, but certain considerations must be taken to ensure MATs to succeed, such as immunogenicity, specificity, and stability *in vivo*. While this dissertation has demonstrated TAB004's tumor antigen specificity in a PDA tumor models, the questions of plasma antigen specificity, stability, and immunogenicity remain. The preliminary work here sets out to answer them.

The MUC1-N and MUC1-C subunits are cleaved by a disintegrin and metalloprotease 17 (ADAM 17) [151]. The MUC1-C subunit may be activated and translocated to the cell's nucleus and promote transcription of tumor-promoting genes [152] while the MUC1-N (tMUC1) subunit is free to enter the circulation. One of the problems associated with CA19.9 antibodies are their inability to distinguish between tumor and free tMUC1 and based on this fact I decided to test TAB004 against this problem.

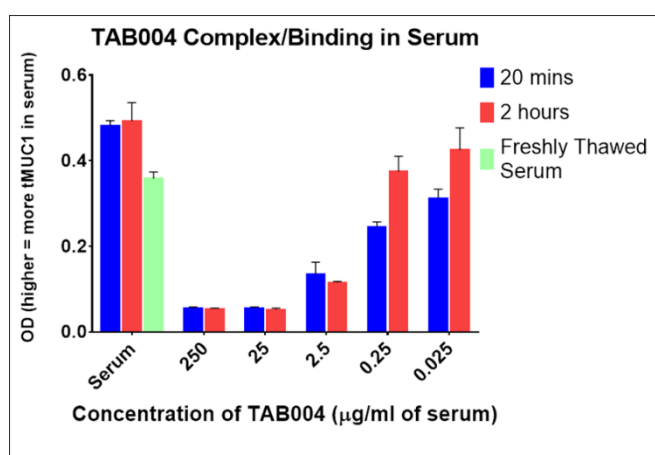


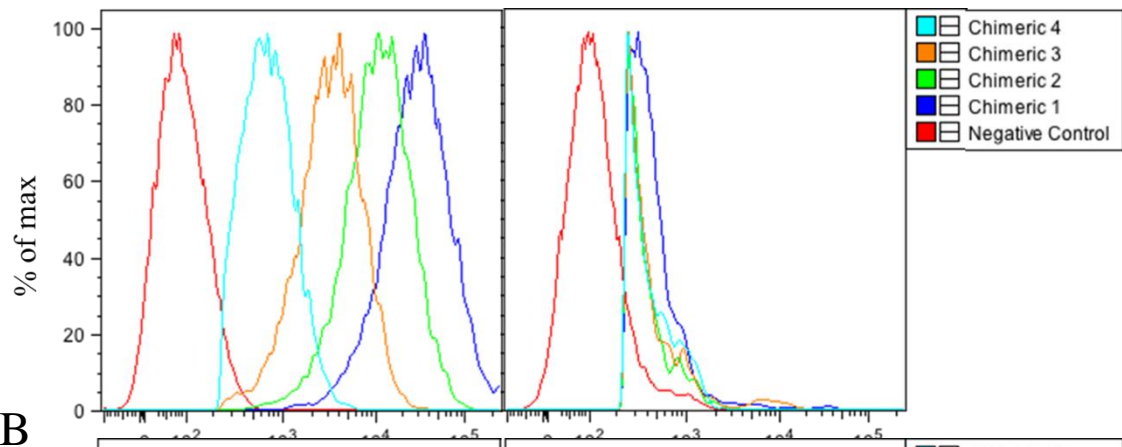
Figure 29. ELISA data of murine TAB004 incubated with tMUC1. Higher optical density (OD) values = higher level of tMUC1 detected.

Briefly, different concentrations of mTAB004 were incubated with tMUC1 positive murine serum for 20 minute or 2 hours on a shaker at 37°C. After incubation, an anti-tMUC1 ELISA was performed on the samples at 25°C. Our results indicate that TAB004 does bind with free tMUC1 in serum/plasma (Fig. 27). Freshly thawed serum and serum incubated for 20 minutes and 2 hours served as controls and registered high levels of tMUC1, as expected. It is interesting to note that freshly thawed serum appears to have lower level of tMUC1, even though the samples are identical. This effect is most likely due to the temperature differences during the beginning of the experiment. At high concentrations of mTAB004 (250 and 25 µg/ml of serum) added to the serum, the tMUC1 OD values from samples incubated at 20 minutes and 2 hours were the same as background controls. As concentrations of mTAB004 decrease, the OD values of tMUC1 increase for both time points. This data demonstrates that TAB004 binds to free tMUC1 in the serum, similar to CA19.9. MATs based on TAB004 may not function *in vivo* due to this result and can probably only be used for imaging purposes, where it's quick cleared from circulation. Nevertheless, the *in vivo* data from chapter 2 of this dissertation remain promising and further studies must to be done to make a definitive conclusion.

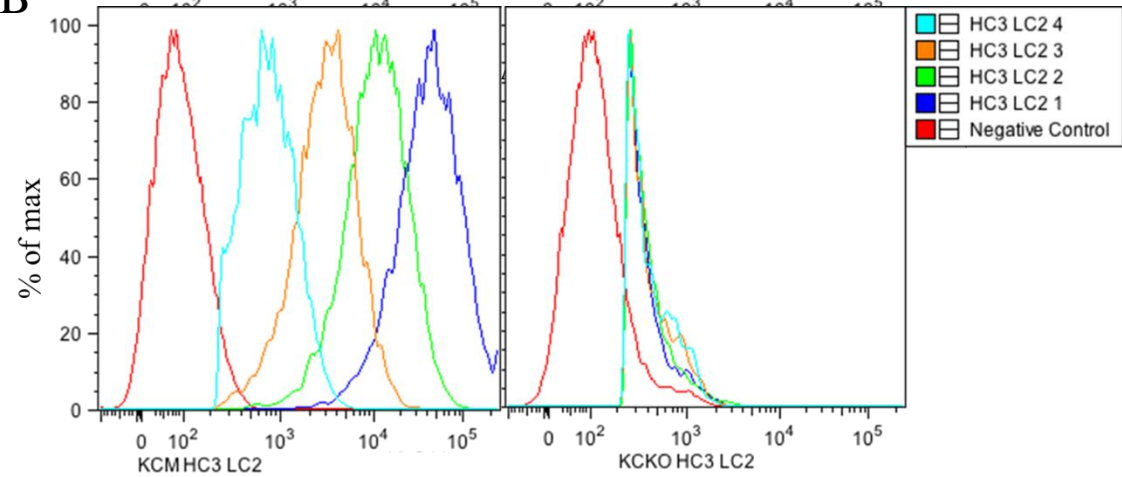
Humanized mAbs are essential to address the issue of immunogenicity of MATs in humans [153]. Humanized TAB004 (hTAB004, HC3 LC2) was acquired (LakePharma Inc., Belmont, CA) and its binding profile was compared to chimeric TAB004 (cTAB004) (Fig. 28). hTAB004 differs from cTAB004 in that it is built on a human IgG2 backbone structure and only the hypervariable regions of the light and heavy chain remain murine (cTAB004 is built on human IgG1 constant regions and murine variable regions). The human IgG2 subtype was chosen since studies have shown that human IgG1 is highly immunogenic in

mice and was more potent in activating mouse NK cells, polymorphonuclear leucocytes, and macrophages human compared to IgG2 [66].

A



B



hTAB004-APC Cy7

Figure 30. FACS analysis of cTAB004 and hTAB004 binding profiles. An identical range of concentrations of cTAB004 (A) and hTAB004 (B) incubated with KCM (left) and KCKO (right). 1 = highest, 4 = lowest concentration.

Briefly, cTAB004 and hTAB004 were conjugated to APC-Cy7 and incubated with KCM or KCKO at different concentration for 20 minutes. KCKO is a cell line derived from a crossing of KC mice with MUC1 and murine *Muc1* knockout mice to produce KCKO mice. These mice are absent of both human and murine mucin-1. The 4 concentrations were 2, 0.4, 0.08, and 0.016 μg of antibody per 5×10^5 cells (designated 1, 2, 3, and 4 respectively in Fig 28). A standard flow cytometry protocol was performed and the results determined by FloJo program. The results show that cTAB004 binds to KCM cells in a concentration dependent manner (Fig. 28A) and there is negligible binding to KCKO cells. The same is true for hTAB004, it binds to KCM cells in a concentration dependent manner (Fig. 28B) and does not bind KCKO cells. The binding profiles of cTAB004 and hTAB004 are almost identical. hTAB004 also internalizes into tMUC1 expressing cell lines, similar to mouse and cTAB004 (data not shown). I would expect to see similar results *in vivo* and this data is very encouraging for future studies involving humanized TAB004.

Antibody stability in serum can be a good indicator of its ability to remain in circulation over time *in vivo* [154]. In many instances, antibody therapeutics recovered from circulation in blood show altered physiochemical characteristics and lower potency [154]. To elucidate the stability of TAB004, I conjugated mTAB004, hTAB004, and a commercially available mouse IgG1 antibody (iIgG1) to ICG, and incubated them in mouse and human serum for various time points (Fig. 29). A time-dependent degradation is observed in all 3 antibodies (Fig. 29) in mouse (left) and human (right) serum as indicated by the shift from red to green fluorescence signal in the 150kDa (size of full-length IgG1 or IgG2) band as time progresses on an SDS-PAGE non reducing gel electrophoresis. As time progresses, a band at the 40-50kDa mark intensifies suggesting that the antibodies are

being degraded and the by-products are 40-50kDa in size. Unfortunately, due to the non-specific nature of the conjugation of ICG to the antibodies, it is impossible to determine where and which parts of the antibodies are being degraded. ICG becoming unbound from the antibody is not likely, as it is <1 kDa and would be much lower on the gel. The antibodies in human serum appear to degrade more quickly and into more by-products (Fig. 29). Encouragingly, TAB004 seems to be more stable than the commercially available mouse IgG1, which is almost completely degraded in human serum. Currently, research is being done to determine what is causing this degradation. The current hypothesis is that a proteinase, such as papain, is degrading or digesting the antibody.

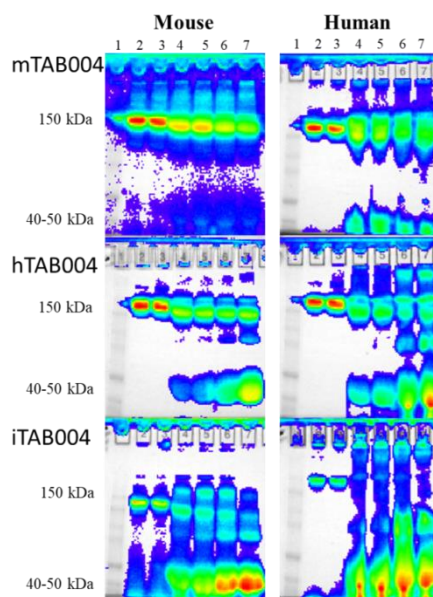


Figure 31. IVIS images of SDS-PAGE gels. Murine TAB004 (mTAB004), human TAB004 (hTAB004), and commercial mouse IgG1 (iTAB004) were conjugated to ICG, incubated with murine or human serum, and run on a SDS-PAGE gel under non-reducing conditions. Lane 1 = ladder, 2 = TAB004-ICG in PBS 24hrs, 3 = TAB004-ICG in PBS 48hrs, 4 = TAB004-ICG in serum 2hrs, 5 = TAB004-ICG in serum 4hrs, 6 = TAB004-ICG in serum 24hrs, 7 = TAB004-ICG in serum 48hrs. Rainbow indicates fluorescence intensity (dark blue = least intense, dark red = most intense).

tMUC1 regulation of Macropinocytosis

Lastly, preliminary work has been done to determine if tMUC1 regulates macropinocytosis in any way. Macropinocytosis is an endocytic process resulting in actin-mediated membrane ruffling (lamellipodia) at the plasma membrane and cytoskeleton remodeling [155]. The lamellipodia fold back upon themselves and fuse with the membrane, creating large vesicles called macropinosomes [156]. Cancers exploit this process to enhance tumorigenesis. Macropinocytosis is an efficient method for cancer cells to internalize surrounding proteins for food and internalize cell surface receptors to either down-regulate inhibitory or activate pro-tumorigenic ones [157]. Research has shown the MUC1 complexes with CIN85, an adaptor protein involved in cytoskeleton remodeling [158] and promote the formation of invadopodia-like structure on the cell surface. I hypothesized that MUC1, through complex with CIN85, plays a role in regulating micropinocytosis in PDA.

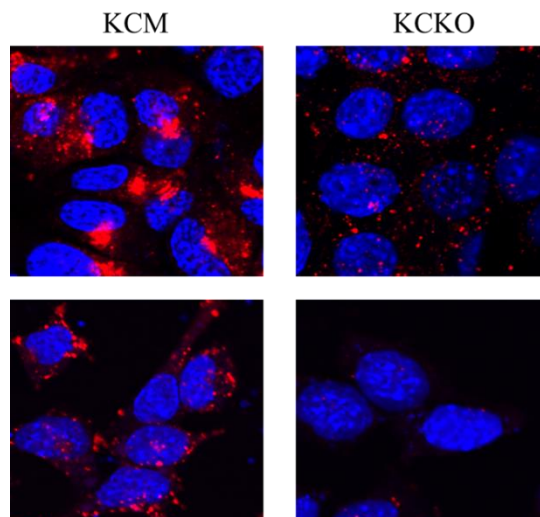


Figure 32. Confocal images of Mouse PDA cell lines treated with TMR-Dextran. Red indicates internalized dextran. Blue indicates DAPI nucleus staining.

Briefly, murine PDA cell lines, KCM, KCKO, Panc02.MUC1, and Panc02.Neo were plated in chamber slides and treated with TMR-dextran red for 1 hour; then imaged with a confocal microscope (Fig. 30). Dextran, used in the quantitation of macropinosomes, is a hydrophilic, non-digestible carbohydrate, and does not induce any active internalization process on cell surfaces. These early results suggest that high tMUC1 expressing cell lines, KCM and Panc02.MUC1 (a murine PDA cell line that expresses tMUC1 through transduction) internalize more dextran (red) than cells that do not express tMUC1, KCKO and Panc02.Neo (same cell line as Panc02 except transduction with an empty vector). Future studies involving adding in or knocking out functions will need to be conducted to draw any conclusions in this subject.

Works Cited

1. Siegel, R.L., K.D. Miller, and A. Jemal, *Cancer statistics, 2017*. CA: A Cancer Journal for Clinicians, 2017. **67**(1): p. 7-30.
2. Society, A.C., *Cancer facts & figures*. American Cancer Society, 2017.
3. Melisi, D. and A. Budillon, *Pancreatic cancer: between bench and bedside*. Curr Drug Targets, 2012. **13**(6): p. 729-30.
4. Stathis, A. and M.J. Moore, *Advanced pancreatic carcinoma: current treatment and future challenges*. Nat Rev Clin Oncol, 2010. **7**(3): p. 163-72.
5. Kleeff, J., et al., *Pancreatic cancer*. 2016. **2**: p. 16022.
6. Tamburrino, A., et al., *Mechanisms of resistance to chemotherapeutic and anti-angiogenic drugs as novel targets for pancreatic cancer therapy*. Front Pharmacol, 2013. **4**: p. 56.
7. Winter, J.M., et al., *Survival after resection of pancreatic adenocarcinoma: results from a single institution over three decades*. Ann Surg Oncol, 2012. **19**(1): p. 169-75.
8. Fokas, E., et al., *Pancreatic ductal adenocarcinoma: From genetics to biology to radiobiology to oncoimmunology and all the way back to the clinic*. Biochim Biophys Acta, 2015. **1855**(1): p. 61-82.
9. Erkan, M., et al., *The role of stroma in pancreatic cancer: diagnostic and therapeutic implications*. Nat Rev Gastroenterol Hepatol, 2012. **9**(8): p. 454-67.
10. Distler, M., et al., *Precursor lesions for sporadic pancreatic cancer: PanIN, IPMN, and MCN*. Biomed Res Int, 2014. **2014**: p. 474905.
11. Yeo, C.J. and J.L. Cameron, *Prognostic factors in ductal pancreatic cancer*. Langenbeck's Archives of Surgery, 1998. **383**(2): p. 129-133.
12. Shimizu, Y., et al., *Small carcinoma of the pancreas is curable: new computed tomography finding, pathological study and postoperative results from a single institute*. J Gastroenterol Hepatol, 2005. **20**(10): p. 1591-4.
13. Durymanov, M.O., A.A. Rosenkranz, and A.S. Sobolev, *Current Approaches for Improving Intratumoral Accumulation and Distribution of Nanomedicines*. Theranostics, 2015. **5**(9): p. 1007-20.
14. Wong, J.C. and D.S.K. Lu, *Staging of Pancreatic Adenocarcinoma by Imaging Studies*. Clinical Gastroenterology and Hepatology. **6**(12): p. 1301-1308.
15. Long, E.E., et al., *Computed tomography, endoscopic, laparoscopic, and intra-operative sonography for assessing resectability of pancreatic cancer*. Surgical Oncology, 2005. **14**(2): p. 105-113.
16. Brennan, D.D.D., et al., *Comprehensive Preoperative Assessment of Pancreatic Adenocarcinoma with 64-Section Volumetric CT*. RadioGraphics, 2007. **27**(6): p. 1653-1666.
17. Lee, J.H., et al., *Acinar Cell Carcinoma of the Pancreas: A Report of Two Cases with Long-term Follow-up and a Review of the Literature*. J Korean Surg Soc, 2010. **79**(4): p. 310-315.
18. Tummala, P., O. Junaidi, and B. Agarwal, *Imaging of pancreatic cancer: An overview*. J Gastrointest Oncol, 2011. **2**(3): p. 168-74.

19. Andersson, R., C.E. Vagianos, and R.C.N. Williamson, *Preoperative staging and evaluation of resectability in pancreatic ductal adenocarcinoma*. *HPB*. **6**(1): p. 5-12.
20. Peddu, P., et al., *Role of imaging in the management of pancreatic mass*. *Critical Reviews in Oncology / Hematology*. **70**(1): p. 12-23.
21. Callery, M.P., et al., *Pretreatment Assessment of Resectable and Borderline Resectable Pancreatic Cancer: Expert Consensus Statement*. *Annals of Surgical Oncology*, 2009. **16**(7): p. 1727-1733.
22. Matsuyama, M., et al., *Ultrasound-guided vs endoscopic ultrasound-guided fine-needle aspiration for pancreatic cancer diagnosis*. *World Journal of Gastroenterology : WJG*, 2013. **19**(15): p. 2368-2373.
23. Burris, H.A., 3rd, et al., *Improvements in survival and clinical benefit with gemcitabine as first-line therapy for patients with advanced pancreas cancer: a randomized trial*. *J Clin Oncol*, 1997. **15**(6): p. 2403-13.
24. Chiaravalli, M., M. Reni, and E.M. O'Reilly, *Pancreatic ductal adenocarcinoma: State-of-the-art 2017 and new therapeutic strategies*. *Cancer Treatment Reviews*, 2017. **60**(Supplement C): p. 32-43.
25. Cooper, A.B., et al., *Does the use of neoadjuvant therapy for pancreatic adenocarcinoma increase postoperative morbidity and mortality rates? J Gastrointest Surg*, 2015. **19**(1): p. 80-6; discussion 86-7.
26. Von Hoff, D.D., D. Goldstein, and M.F. Renschler, *Albumin-bound paclitaxel plus gemcitabine in pancreatic cancer*. *N Engl J Med*, 2014. **370**(5): p. 479-80.
27. Von Hoff, D.D., et al., *Gemcitabine plus nab-paclitaxel is an active regimen in patients with advanced pancreatic cancer: a phase I/II trial*. *J Clin Oncol*, 2011. **29**(34): p. 4548-54.
28. Frese, K.K., et al., *nab-Paclitaxel potentiates gemcitabine activity by reducing cytidine deaminase levels in a mouse model of pancreatic cancer*. *Cancer Discov*, 2012. **2**(3): p. 260-9.
29. Von Hoff, D.D., et al., *Increased Survival in Pancreatic Cancer with nab-Paclitaxel plus Gemcitabine*. *New England Journal of Medicine*, 2013. **369**(18): p. 1691-1703.
30. He, L., G.A. Orr, and S.B. Horwitz, *Novel molecules that interact with microtubules and have functional activity similar to Taxol*. *Drug Discov Today*, 2001. **6**(22): p. 1153-1164.
31. Herbst, R.S. and F.R. Khuri, *Mode of action of docetaxel - a basis for combination with novel anticancer agents*. *Cancer Treat Rev*, 2003. **29**(5): p. 407-15.
32. Galley, H.F., et al., *Melatonin limits paclitaxel-induced mitochondrial dysfunction in vitro and protects against paclitaxel-induced neuropathic pain in the rat*. *J Pineal Res*, 2017.
33. King, J., et al., *Improving theranostics in pancreatic cancer*. *J Surg Oncol*, 2017. **116**(1): p. 104-113.
34. Salaun, P.Y., et al., *Phase II trial of anticarcinoembryonic antigen pretargeted radioimmunotherapy in progressive metastatic medullary thyroid carcinoma*:

- biomarker response and survival improvement.* J Nucl Med, 2012. **53**(8): p. 1185-92.
35. Kraeber-Bodere, F., et al., *Radioimmunotherapy in medullary thyroid cancer using bispecific antibody and iodine 131-labeled bivalent hapten: preliminary results of a phase I/II clinical trial.* Clin Cancer Res, 1999. **5**(10 Suppl): p. 3190s-3198s.
 36. Hiroshima, Y., et al., *Effective fluorescence-guided surgery of liver metastasis using a fluorescent anti-CEA antibody.* J Surg Oncol, 2016. **114**(8): p. 951-958.
 37. Houghton, J.L., et al., *Site-specifically labeled CA19.9-targeted immunoconjugates for the PET, NIRF, and multimodal PET/NIRF imaging of pancreatic cancer.* Proc Natl Acad Sci U S A, 2015. **112**(52): p. 15850-5.
 38. Shaib, W., R. Mahajan, and B. El-Rayes, *Markers of resistance to anti-EGFR therapy in colorectal cancer.* J Gastrointest Oncol, 2013. **4**(3): p. 308-18.
 39. Shi, C. and K. Washington, *Molecular testing in colorectal cancer: diagnosis of Lynch syndrome and personalized cancer medicine.* Am J Clin Pathol, 2012. **137**(6): p. 847-59.
 40. Beauchemin, N. and A. Arabzadeh, *Carcinoembryonic antigen-related cell adhesion molecules (CEACAMs) in cancer progression and metastasis.* Cancer Metastasis Rev, 2013. **32**(3-4): p. 643-71.
 41. Hegele, A., et al., *CA19.9 and CEA in transitional cell carcinoma of the bladder: serological and immunohistochemical findings.* Anticancer Res, 2010. **30**(12): p. 5195-200.
 42. Kannagi, R., *Carbohydrate antigen sialyl Lewis a--its pathophysiological significance and induction mechanism in cancer progression.* Chang Gung Med J, 2007. **30**(3): p. 189-209.
 43. Sawada, R., et al., *Human monoclonal antibodies to sialyl-Lewis (CA19.9) with potent CDC, ADCC, and antitumor activity.* Clin Cancer Res, 2011. **17**(5): p. 1024-32.
 44. Au, M., et al., *Emerging Therapeutic Potential of Nanoparticles in Pancreatic Cancer: A Systematic Review of Clinical Trials.* Biomedicines, 2016. **4**(3).
 45. Jain, K.K., *Advances in the field of nanooncology.* BMC Med, 2010. **8**: p. 83.
 46. Bertrand, N., et al., *Cancer nanotechnology: the impact of passive and active targeting in the era of modern cancer biology.* Adv Drug Deliv Rev, 2014. **66**: p. 2-25.
 47. Dong, X. and R.J. Mumper, *Nanomedicinal strategies to treat multidrug-resistant tumors: current progress.* Nanomedicine, 2010. **5**(4): p. 597-615.
 48. Hollis, C.P., et al., *Biodistribution and bioimaging studies of hybrid paclitaxel nanocrystals: lessons learned of the EPR effect and image-guided drug delivery.* J Control Release, 2013. **172**(1): p. 12-21.
 49. Malekigorji M, C.A., Hoskins C *The Use of Iron Oxide Nanoparticles for Pancreatic Cancer Therapy.* . J Nanomed Res, 2014. **1**(1): **00004**.
 50. Kunjachan, S., et al., *Passive versus active tumor targeting using RGD- and NGR-modified polymeric nanomedicines.* Nano Lett, 2014. **14**(2): p. 972-81.

51. Du, J.Z., et al., *Tumor extracellular acidity-activated nanoparticles as drug delivery systems for enhanced cancer therapy*. *Biotechnol Adv*, 2014. **32**(4): p. 789-803.
52. Muthu, M.S., et al., *Nanotheranostics - application and further development of nanomedicine strategies for advanced theranostics*. *Theranostics*, 2014. **4**(6): p. 660-77.
53. Yang, T., et al., *Anti-tumor Efficiency of Lipid-coated Cisplatin Nanoparticles Co-loaded with MicroRNA-375*. *Theranostics*, 2016. **6**(1): p. 142-54.
54. Xing, L., et al., *Ultrasound-Mediated Microbubble Destruction (UMMD) Facilitates the Delivery of CA19-9 Targeted and Paclitaxel Loaded mPEG-PLGA-PLL Nanoparticles in Pancreatic Cancer*. *Theranostics*, 2016. **6**(10): p. 1573-87.
55. Nath, S. and P. Mukherjee, *MUC1: a multifaceted oncoprotein with a key role in cancer progression*. *Trends Mol Med*, 2014. **20**(6): p. 332-42.
56. Hattstrup, C.L. and S.J. Gendler, *Structure and function of the cell surface (tethered) mucins*. *Annu Rev Physiol*, 2008. **70**: p. 431-57.
57. Gendler, S.J., *MUC1, The Renaissance Molecule*. *Journal of Mammary Gland Biology and Neoplasia*, 2001. **6**(3): p. 339-353.
58. Yolken, R.H., et al., *Human milk mucin inhibits rotavirus replication and prevents experimental gastroenteritis*. *The Journal of Clinical Investigation*. **90**(5): p. 1984-1991.
59. Gendler, S.J., et al., *Molecular cloning and expression of human tumor-associated polymorphic epithelial mucin*. *J Biol Chem*, 1990. **265**(25): p. 15286-93.
60. Burdick, M.D., et al., *Oligosaccharides expressed on MUC1 produced by pancreatic and colon tumor cell lines*. *J Biol Chem*, 1997. **272**(39): p. 24198-202.
61. Patton, S., S.J. Gendler, and A.P. Spicer, *The epithelial mucin, MUC1, of milk, mammary gland and other tissues*. *Biochim Biophys Acta*, 1995. **1241**(3): p. 407-23.
62. Roy, L.D., et al., *MUC1 enhances invasiveness of pancreatic cancer cells by inducing epithelial to mesenchymal transition*. *Oncogene*, 2011. **30**(12): p. 1449-1459.
63. Cheever, M.A., et al., *The Prioritization of Cancer Antigens: A National Cancer Institute Pilot Project for the Acceleration of Translational Research*. *Clinical Cancer Research*, 2009. **15**(17): p. 5323-5337.
64. Verhoeyen, M.E., et al., *Construction of a reshaped HMFG1 antibody and comparison of its fine specificity with that of the parent mouse antibody*. *Immunology*, 1993. **78**(3): p. 364-70.
65. Fan, X.N., et al., *Reactivity of a humanized antibody (hPankoMab) towards a tumor-related MUC1 epitope (TA-MUC1) with various human carcinomas*. *Pathol Res Pract*, 2010. **206**(8): p. 585-9.
66. Overdijk, M.B., et al., *Crosstalk between human IgG isotypes and murine effector cells*. *J Immunol*, 2012. **189**(7): p. 3430-8.
67. Helft, P.R., et al., *A phase I study of cantuzumab mertansine administered as a single intravenous infusion once weekly in patients with advanced solid tumors*. *Clin Cancer Res*, 2004. **10**(13): p. 4363-8.

68. Liu, D., et al., *Identification of PAM4 (clivatuzumab)-reactive epitope on MUC5AC: a promising biomarker and therapeutic target for pancreatic cancer*. *Oncotarget*, 2015. **6**(6): p. 4274-85.
69. Maitra, A., et al., *Multicomponent analysis of the pancreatic adenocarcinoma progression model using a pancreatic intraepithelial neoplasia tissue microarray*. *Mod Pathol*, 2003. **16**(9): p. 902-12.
70. Hingorani, S.R. and D.A. Tuveson, *Targeting oncogene dependence and resistance*. *Cancer Cell*, 2003. **3**(5): p. 414-7.
71. Tinder, T.L., et al., *MUC1 enhances tumor progression and contributes toward immunosuppression in a mouse model of spontaneous pancreatic adenocarcinoma*. *J Immunol*, 2008. **181**(5): p. 3116-25.
72. Rowse, G.J., et al., *Tolerance and immunity to MUC1 in a human MUC1 transgenic murine model*. *Cancer Res*, 1998. **58**(2): p. 315-21.
73. Besmer, D.M., et al., *Pancreatic ductal adenocarcinoma mice lacking mucin 1 have a profound defect in tumor growth and metastasis*. *Cancer Res*, 2011. **71**(13): p. 4432-42.
74. Curry, J.M., et al., *The use of a novel MUC1 antibody to identify cancer stem cells and circulating MUC1 in mice and patients with pancreatic cancer*. *J Surg Oncol*, 2013. **107**(7): p. 713-22.
75. Moore, L.J., et al., *Antibody-Guided In Vivo Imaging for Early Detection of Mammary Gland Tumors*. *Transl Oncol*, 2016. **9**(4): p. 295-305.
76. Lau, S.K., L.M. Weiss, and P.G. Chu, *Differential expression of MUC1, MUC2, and MUC5AC in carcinomas of various sites: an immunohistochemical study*. *Am J Clin Pathol*, 2004. **122**(1): p. 61-9.
77. Sahraei, M., et al., *MUC1 regulates PDGFA expression during pancreatic cancer progression*. *Oncogene*, 2012. **31**(47): p. 4935-45.
78. Curry, J.M., et al., *The Use of a Novel MUC1 Antibody to Identify Cancer Stem Cells and Circulating MUC1 in Mice and Patients With Pancreatic Cancer*. *Journal of surgical oncology*, 2013. **107**(7): p. 10.1002/jso.23316.
79. Nath, S., et al., *MUC1 induces drug resistance in pancreatic cancer cells via upregulation of multidrug resistance genes*. *Oncogenesis*, 2013. **2**(6): p. e51.
80. Zhou, R., et al., *A novel association of neuropilin-1 and MUC1 in pancreatic ductal adenocarcinoma: role in induction of VEGF signaling and angiogenesis*. *Oncogene*, 2016.
81. Von Hoff, D.D., et al., *Increased Survival in Pancreatic Cancer with nab-Paclitaxel plus Gemcitabine*. *The New England journal of medicine*, 2013. **369**(18): p. 1691-1703.
82. Von Hoff, D.D., et al., *Increased survival in pancreatic cancer with nab-paclitaxel plus gemcitabine*. *N Engl J Med*, 2013. **369**(18): p. 1691-703.
83. Schneider, D.W., et al., *In Vivo Biodistribution, PET Imaging, and Tumor Accumulation of 86Y-and 111In-Antimindin/RG-1, Engineered Antibody Fragments in LNCaP Tumor-Bearing Nude Mice*. *Journal of Nuclear Medicine*, 2009. **50**(3): p. 435-443.
84. Siegel, R.L., K.D. Miller, and A. Jemal, *Cancer statistics, 2015*. CA: A Cancer Journal for Clinicians, 2015. **65**(1): p. 5-29.

85. Bose, R.J., S.H. Lee, and H. Park, *Lipid-based surface engineering of PLGA nanoparticles for drug and gene delivery applications*. *Biomater Res*, 2016. **20**: p. 34.
86. Okamura, Y., et al., *Prolonged hemostatic ability of polyethylene glycol-modified polymerized albumin particles carrying fibrinogen gamma-chain dodecapeptide*. *Transfusion*, 2007. **47**(7): p. 1254-62.
87. Moghimi, S.M., A.C. Hunter, and J.C. Murray, *Long-circulating and target-specific nanoparticles: theory to practice*. *Pharmacol Rev*, 2001. **53**(2): p. 283-318.
88. Danhier, F., et al., *PLGA-based nanoparticles: an overview of biomedical applications*. *J Control Release*, 2012. **161**(2): p. 505-22.
89. Sarin, V.K., et al., *Quantitative monitoring of solid-phase peptide synthesis by the ninhydrin reaction*. *Analytical Biochemistry*, 1981. **117**(1): p. 147-157.
90. Roy, L.D., et al., *MUC1 enhances invasiveness of pancreatic cancer cells by inducing epithelial to mesenchymal transition*. *Oncogene*, 2010.
91. Amin, M.L., D. Kim, and S. Kim, *Development of hematin conjugated PLGA nanoparticle for selective cancer targeting*. *Eur J Pharm Sci*, 2016. **91**: p. 138-43.
92. Nath, S., et al., *MUC1 induces drug resistance in pancreatic cancer cells via upregulation of multidrug resistance genes*. *Oncogenesis*, 2013. **2**: p. e51.
93. Graf, N., et al., *$\alpha V\beta 3$ Integrin-Targeted PLGA-PEG Nanoparticles for Enhanced Anti-tumor Efficacy of a Pt(IV) Prodrug*. *ACS Nano*, 2012. **6**(5): p. 4530-4539.
94. Sahu, A., et al., *Synthesis of novel biodegradable and self-assembling methoxy poly(ethylene glycol)-palmitate nanocarrier for curcumin delivery to cancer cells*. *Acta Biomater*, 2008. **4**(6): p. 1752-61.
95. Kamphorst, J.J., et al., *Human pancreatic cancer tumors are nutrient poor and tumor cells actively scavenge extracellular protein*. *Cancer Res*, 2015. **75**(3): p. 544-53.
96. Sousa, C.M. and A.C. Kimmelman, *The complex landscape of pancreatic cancer metabolism*. *Carcinogenesis*, 2014. **35**(7): p. 1441-50.
97. Besmer, D.M., et al., *Pancreatic ductal adenocarcinoma mice lacking mucin 1 have a profound defect in tumor growth and metastasis*. *Cancer Research*, 2011. **71**(13): p. 4432-42.
98. Zhou, R., et al., *A novel association of neuropilin-1 and MUC1 in pancreatic ductal adenocarcinoma: role in induction of VEGF signaling and angiogenesis*. *Oncogene*, 2016. **35**(43): p. 5608-5618.
99. Dreau, D., et al., *Mucin-1-Antibody-Conjugated Mesoporous Silica Nanoparticles for Selective Breast Cancer Detection in a Mucin-1 Transgenic Murine Mouse Model*. *J Biomed Nanotechnol*, 2016. **12**(12): p. 2172-2184.
100. Qu, C.F., et al., *MUC1 expression in primary and metastatic pancreatic cancer cells for in vitro treatment by (213)Bi-C595 radioimmunoconjugate*. *Br J Cancer*, 2004. **91**(12): p. 2086-93.
101. Winter, J.M., et al., *A novel survival-based tissue microarray of pancreatic cancer validates MUC1 and mesothelin as biomarkers*. *PLoS One*, 2012. **7**(7): p. e40157.

102. Katada, T., et al., *Initial Features of Hepatic Metastases From Pancreatic Cancer: Histological and Radiological Appraisal of Hepatic Micrometastases Detected by Real-Time Fluorescent Imaging*. *Pancreas*, 2017. **46**(9): p. 1196-1201.
103. Pascual, L., et al., *MUC1 aptamer-capped mesoporous silica nanoparticles for controlled drug delivery and radio-imaging applications*. *Nanomedicine*, 2017.
104. Santos do Carmo, F., et al., *Anti-MUC1 nano-aptamers for triple-negative breast cancer imaging by single-photon emission computed tomography in induced animals: initial considerations*. *Int J Nanomedicine*, 2017. **12**: p. 53-60.
105. Park, J.Y., et al., *MUC1 selectively targets human pancreatic cancer in orthotopic nude mouse models*. *PLoS One*, 2015. **10**(3): p. e0122100.
106. Yeh, R., et al., *Imaging of pancreatic cancer: what the surgeon wants to know*. *Clin Imaging*, 2017. **42**: p. 203-217.
107. Buchholz, M., et al., *Transcriptome analysis of microdissected pancreatic intraepithelial neoplastic lesions*. *Oncogene*, 2005. **24**(44): p. 6626-36.
108. Zhou, B., et al., *Early detection of pancreatic cancer: Where are we now and where are we going?* *Int J Cancer*, 2017. **141**(2): p. 231-241.
109. Dreau, D., et al., *Mucin-1-Antibody-Conjugated Mesoporous Silica Nanoparticles for Selective Breast Cancer Detection in a Mucin-1 Transgenic Murine Mouse Model*. *Journal of Biomedical Nanotechnology*, 2016. **12**(12): p. 2172-2184.
110. Iodice, S., et al., *Tobacco and the risk of pancreatic cancer: a review and meta-analysis*. *Langenbecks Arch Surg*, 2008. **393**(4): p. 535-45.
111. Villeneuve, P.J., et al., *Environmental tobacco smoke and the risk of pancreatic cancer: findings from a Canadian population-based case-control study*. *Can J Public Health*, 2004. **95**(1): p. 32-7.
112. Ojajarvi, I.A., et al., *Occupational exposures and pancreatic cancer: a meta-analysis*. *Occup Environ Med*, 2000. **57**(5): p. 316-24.
113. Michaud, D.S., et al., *Physical activity, obesity, height, and the risk of pancreatic cancer*. *Jama*, 2001. **286**(8): p. 921-9.
114. Gupta, S., et al., *New-onset diabetes and pancreatic cancer*. *Clin Gastroenterol Hepatol*, 2006. **4**(11): p. 1366-72; quiz 1301.
115. Chari, S.T., et al., *Pancreatic cancer-associated diabetes mellitus: prevalence and temporal association with diagnosis of cancer*. *Gastroenterology*, 2008. **134**(1): p. 95-101.
116. Pannala, R., et al., *Prevalence and clinical profile of pancreatic cancer-associated diabetes mellitus*. *Gastroenterology*, 2008. **134**(4): p. 981-7.
117. Chari, S.T., et al., *Early detection of sporadic pancreatic cancer: summative review*. *Pancreas*, 2015. **44**(5): p. 693-712.
118. Klein, A.P., et al., *Prospective risk of pancreatic cancer in familial pancreatic cancer kindreds*. *Cancer Res*, 2004. **64**(7): p. 2634-8.
119. Hruban, R.H., et al., *Update on familial pancreatic cancer*. *Adv Surg*, 2010. **44**: p. 293-311.
120. Klein, A.P., *Identifying people at a high risk of developing pancreatic cancer*. *Nat Rev Cancer*, 2013. **13**(1): p. 66-74.

121. Rustgi, A.K., *Familial pancreatic cancer: genetic advances*. Genes Dev, 2014. **28**(1): p. 1-7.
122. Mocci, E., et al., *Risk of pancreatic cancer in breast cancer families from the breast cancer family registry*. Cancer Epidemiol Biomarkers Prev, 2013. **22**(5): p. 803-11.
123. *Cancer risks in BRCA2 mutation carriers*. J Natl Cancer Inst, 1999. **91**(15): p. 1310-6.
124. Geoffroy-Perez, B., et al., *Cancer risk in heterozygotes for ataxia-telangiectasia*. Int J Cancer, 2001. **93**(2): p. 288-93.
125. Fernandes, P.H., et al., *Comprehensive sequencing of PALB2 in patients with breast cancer suggests PALB2 mutations explain a subset of hereditary breast cancer*. Cancer, 2014. **120**(7): p. 963-7.
126. Yu, C., et al., *Novel aptamer-nanoparticle bioconjugates enhances delivery of anticancer drug to MUC1-positive cancer cells in vitro*. PLoS One, 2011. **6**(9): p. e24077.
127. Mahapatro, A. and D.K. Singh, *Biodegradable nanoparticles are excellent vehicle for site directed in-vivo delivery of drugs and vaccines*. J Nanobiotechnology, 2011. **9**: p. 55.
128. Nobs, L., et al., *Poly(lactic acid) nanoparticles labeled with biologically active Neutravidin for active targeting*. Eur J Pharm Biopharm, 2004. **58**(3): p. 483-90.
129. Sadat Tabatabaei Mirakabad, F., et al., *PLGA-based nanoparticles as cancer drug delivery systems*. Asian Pac J Cancer Prev, 2014. **15**(2): p. 517-35.
130. Guo, J., et al., *Aptamer-functionalized PEG-PLGA nanoparticles for enhanced anti-glioma drug delivery*. Biomaterials, 2011. **32**(31): p. 8010-20.
131. Hisatsune, A., et al., *Internalization of MUC1 by anti-MUC1 antibody from cell membrane through the macropinocytotic pathway*. Biochem Biophys Res Commun, 2009. **388**(4): p. 677-82.
132. Fonseca, C., S. Simões, and R. Gaspar, *Paclitaxel-loaded PLGA nanoparticles: preparation, physicochemical characterization and in vitro anti-tumoral activity*. Journal of Controlled Release, 2002. **83**(2): p. 273-286.
133. Hawker, C.J. and K.L. Wooley, *The Convergence of Synthetic Organic and Polymer Chemistries*. Science, 2005. **309**(5738): p. 1200-1205.
134. Malam, Y., M. Loizidou, and A.M. Seifalian, *Liposomes and nanoparticles: nanosized vehicles for drug delivery in cancer*. Trends in Pharmacological Sciences. **30**(11): p. 592-599.
135. Hu, C.-M.J., et al., *Half-Antibody Functionalized Lipid-Polymer Hybrid Nanoparticles for Targeted Drug Delivery to Carcinoembryonic Antigen Presenting Pancreatic Cancer Cells*. Molecular Pharmaceutics, 2010. **7**(3): p. 914-920.
136. Misra, R., S. Acharya, and S.K. Sahoo, *Cancer nanotechnology: application of nanotechnology in cancer therapy*. Drug Discovery Today, 2010. **15**(19): p. 842-850.
137. Jain, A.K., et al., *Adapalene loaded solid lipid nanoparticles gel: an effective approach for acne treatment*. Colloids Surf B Biointerfaces, 2014. **121**: p. 222-9.

138. Wong, H.L., et al., *Chemotherapy with anticancer drugs encapsulated in solid lipid nanoparticles*. *Advanced Drug Delivery Reviews*, 2007. **59**(6): p. 491-504.
139. Doktorovova, S., E.B. Souto, and A.M. Silva, *Nanotoxicology applied to solid lipid nanoparticles and nanostructured lipid carriers – A systematic review of in vitro data*. *European Journal of Pharmaceutics and Biopharmaceutics*, 2014. **87**(1): p. 1-18.
140. Shao, Z., et al., *Targeted lung cancer therapy: preparation and optimization of transferrin-decorated nanostructured lipid carriers as novel nanomedicine for co-delivery of anticancer drugs and DNA*. *Int J Nanomedicine*, 2015. **10**: p. 1223-33.
141. Park, J.-H., et al., *Micellar Hybrid Nanoparticles for Simultaneous Magnetofluorescent Imaging and Drug Delivery*. *Angewandte Chemie*, 2008. **120**(38): p. 7394-7398.
142. Blasiak, B., F.C.J.M. van Veggel, and B. Tomanek, *Applications of Nanoparticles for MRI Cancer Diagnosis and Therapy*. *Journal of Nanomaterials*, 2013. **2013**: p. 12.
143. Astruc, D., E. Boisselier, and C. Ornelas, *Dendrimers Designed for Functions: From Physical, Photophysical, and Supramolecular Properties to Applications in Sensing, Catalysis, Molecular Electronics, Photonics, and Nanomedicine*. *Chemical Reviews*, 2010. **110**(4): p. 1857-1959.
144. Hawker, C.J. and J.M.J. Frechet, *Preparation of polymers with controlled molecular architecture. A new convergent approach to dendritic macromolecules*. *Journal of the American Chemical Society*, 1990. **112**(21): p. 7638-7647.
145. Turrin, C.-O. and A.-M. Caminade, *Dendrimers for Imaging*, in *Dendrimers*. 2011, John Wiley & Sons, Ltd. p. 393-412.
146. Menjoge, A.R., R.M. Kannan, and D.A. Tomalia, *Dendrimer-based drug and imaging conjugates: design considerations for nanomedical applications*. *Drug Discovery Today*, 2010. **15**(5): p. 171-185.
147. Peng, X.H., et al., *Targeted magnetic iron oxide nanoparticles for tumor imaging and therapy*. *Int J Nanomedicine*, 2008. **3**(3): p. 311-21.
148. Yu, M.K., et al., *Drug-Loaded Superparamagnetic Iron Oxide Nanoparticles for Combined Cancer Imaging and Therapy In Vivo*. *Angewandte Chemie International Edition*, 2008. **47**(29): p. 5362-5365.
149. Sun, C., et al., *PEG-Mediated Synthesis of Highly Dispersive Multifunctional Superparamagnetic Nanoparticles: Their Physicochemical Properties and Function In Vivo*. *ACS Nano*, 2010. **4**(4): p. 2402-2410.
150. Dasgeb, B., et al., *Colchicine: an ancient drug with novel applications*. *British Journal of Dermatology*: p. n/a-n/a.
151. Thathiah, A., C.P. Blobel, and D.D. Carson, *Tumor necrosis factor-alpha converting enzyme/ADAM 17 mediates MUC1 shedding*. *J Biol Chem*, 2003. **278**(5): p. 3386-94.
152. Nath, S., et al., *Mucin 1 Regulates Cox-2 Gene in Pancreatic Cancer*. *Pancreas*, 2015. **44**(6): p. 909-17.
153. Firer, M.A. and G. Gellerman, *Targeted drug delivery for cancer therapy: the other side of antibodies*. *Journal of Hematology & Oncology*, 2012. **5**: p. 70-70.
154. Correia, I.R., *Stability of IgG isotypes in serum*. *MAbs*, 2010. **2**(3): p. 221-32.

155. Peng, H., J.K. Park, and R.M. Lavker, *Autophagy and Macropinocytosis: Keeping an Eye on the Corneal/Limbal Epithelia*. Investigative Ophthalmology & Visual Science, 2017. **58**(1): p. 416-423.
156. Lim, J.P. and P.A. Gleeson, *Macropinocytosis: an endocytic pathway for internalising large gulps*. Immunol Cell Biol, 2011. **89**(8): p. 836-43.
157. Ha, K.D., S.M. Bidlingmaier, and B. Liu, *Macropinocytosis Exploitation by Cancers and Cancer Therapeutics*. Front Physiol, 2016. **7**: p. 381.
158. Cascio, S., et al., *Altered glycosylation of MUC1 influences its association with CIN85: the role of this novel complex in cancer cell invasion and migration*. Oncotarget, 2013. **4**(10): p. 1686-97.

APPENDIX

*Contributions and Awards**Papers*

Wu, S., Fowler, A., Garmon, C., Fessler, A., Ogle, J., Grover, K., Allen, B., Williams, C., Zhou, R., Yazdanifar, M., Ogle, C., Mukherjee, P. Treatment of pancreatic ductal adenocarcinoma with tumor antigen specific-targeted delivery of paclitaxel loaded PLGA nanoparticles. *Under review, BMC Cancer*

Wu, S., Williams, C., Moore, L., Grover, P., Mukherjee, P. Early detection of pancreatic cancer in mouse models using novel antibody, TAB004. *Under review, PLOS ONE*

Moore, L. J., Roy, L. D., Zhou, R., Grover, P., **Wu, S.**, Curry, J. M., Dillon, L., Puri, P., Yazdanifar, M., Puri, R., Mukherjee, P., Dréau, D. (2016). Antibody-Guided In Vivo Imaging for Early Detection of Mammary Gland Tumors. *Translational Oncology*, 9(4), 295–305. <http://doi.org/10.1016/j.tranon.2016.05.001>

Zhou, R., Curry, J. M., Roy, L. D., Grover, P., Haider, J., Moore, L. J., **Wu, S.**, Kamesh, A., Yazdanifar, M., Ahrens, W., Leung, TC., Mukherjee, P. (2016). A Novel Association of Neuropilin-1 and MUC1 in Pancreatic Ductal Adenocarcinoma: Role in Induction of VEGF Signaling and Angiogenesis. *Oncogene*, 35(43), 5608–5618.

<http://doi.org/10.1038/onc.2015.516>

Honors and Awards

- 2014 1st place, poster competition, Physical and Natural Science category,
Graduate Research Symposium, UNC Charlotte, Charlotte, NC
- 2014 1st place, poster competition, Department of Biological Sciences, UNC
Charlotte, Charlotte, NC
- 2014, 2016 UNC Charlotte Center for Biomedical Engineering and Science Travel
Award
- 2014, 2016 UNC Charlotte Graduate and Professional Student Government Travel
Award
- 2013-2015 UNC Charlotte Center for Biomedical Engineering and Science IVIS
Imaging Award
- 2012-2017 UNC Charlotte Graduate Assistant Support Plan Award
- 2017 Outstanding Teaching Assistant Award in Lower division courses, UNC
Charlotte